POLITECNICO
MILANO 1863

SCUOLA DI INGEGNERIA INDUSTRIALE
E DELL'INFORMAZIONE

Rain Attenuation Mitigation for EHF NGSO Systems Using Site and/or Orbital Diversity

TESI DI LAUREA MAGISTRALE IN
TELECOMMUNICATION ENGINEERING

Author: **Sofia Lecci**

Student ID: 10764812
Advisor: Prof. Lorenzo Luini
Co-advisor: Enrico Polo
Academic Year: 2024-25

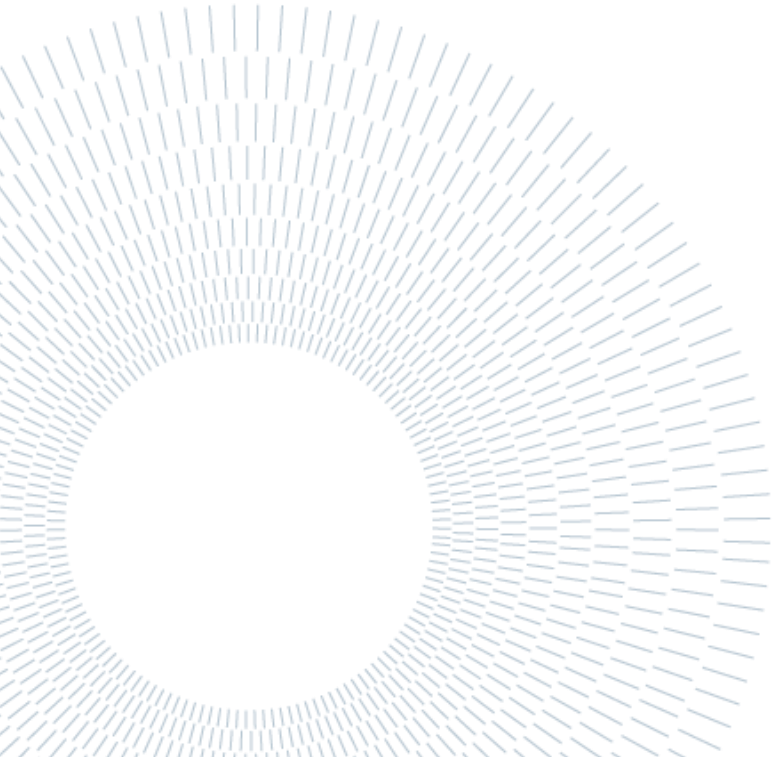

Abstract

In this thesis, a simulation-based framework to investigate rain attenuation on extremely high-frequency (EHF) NGSO satellite links is presented, aimed at quantifying the performance gains achievable through spatial-diversity Fade Mitigation Techniques, namely Site Diversity (SD), Orbital Diversity (OD), and their joint application. Rain attenuation—dominant at Ka, Q and V bands—is modelled by coupling NGSO link geometry with 200 km × 200 km space–time precipitation fields generated by ST-MultiEXCELL over one-year period. The simulator is extended to multi-gateway scenarios by supporting configurable ground-station layouts (line, triangle, square) and inter-site separations, enabling systematic diversity assessments. Simulated attenuation time series are stored and post-processed to derive long-term Complementary Cumulative Distribution Functions (CCDFs) and diversity gains. OD is evaluated via per-epoch selection of the least attenuated link among a controllable number of simultaneously visible satellites, showing monotonic improvement with diversity order. SD is assessed through selection combining across geographically separated gateways, highlighting the dependence of gain on both inter-site distance and the number of deployed sites. Joint SD+OD provides the largest benefit, yielding a further reduction of exceedance probability, especially in the high-attenuation tail relevant to high-availability design.

Finally, a statistical OD model is introduced. The model relates the absolute attenuation difference between simultaneously visible links to their three-dimensional angular separation. Conditional $|\Delta A|$ statistics are fitted with a lognormal distribution whose parameters are expressed as continuous functions of separation angle and characterized across multiple frequencies, enabling the generation of OD-related attenuation-difference statistics without time-domain simulation. Overall, the proposed simulation and modelling approach provides practical tools for dimensioning and designing diversity strategies in future EHF NGSO systems.

Key-words: NGSO constellation, rain attenuation, Site Diversity, Orbital Diversity, ST-MultiEXCELL

Abstract in lingua italiana

La crescente adozione di costellazioni satellitari in orbita non geostazionaria (NGSO) e la migrazione verso frequenze elevate (bande Ka, Q e V) rendono l'attenuazione da pioggia uno dei principali vincoli di progetto per i collegamenti Earth–space. Questa tesi studia in modo quantitativo l'impatto del fading da pioggia su collegamneti NGSO in banda EHF e valuta l'efficacia di tecniche di mitigazione basate sulla diversità spaziale: Site Diversity (SD), Orbital Diversity (OD) e la loro combinazione. A tal fine viene impiegato un ambiente di simulazione che integra campi di precipitazione spazio-temporali generati dal modello ST-MultiEXCELL (mappe 200 km × 200 km) con la geometria istantanea dei collegamenti verso una costellazione NGSO. Il simulatore è esteso a scenari multi-gateway, consentendo il posizionamento di più stazioni di terra secondo geometrie configurabili (linea, triangolo, quadrato) e con distanze inter-sito variabili, in modo da analizzare sistematicamente le prestazioni in diversità. Le serie temporali ottenute vengono elaborate per ricavare CCDF a lungo termine e guadagni di diversità. L'OD, implementata selezionando a ogni istante il link con attenuazione minima tra un numero controllabile di satelliti simultaneamente visibili, mostra un miglioramento crescente all'aumentare dell'ordine di diversità. La tecnica di SD, ottenuta selezionando la stazione meno attenuata tra siti geograficamente separati, evidenzia un guadagno che aumenta sia con la distanza inter-sito sia con il numero di stazioni impiegate. L'applicazione congiunta SD+OD risulta la soluzione più efficace, poiché riduce ulteriormente la probabilità di superamento nelle condizioni più severe. Infine, viene proposto un modello statistico per descrivere l'OD senza ricorrere a simulazioni nel dominio temporale: la distribuzione della differenza assoluta di attenuazione $|\Delta A|$ tra collegamenti simultaneamente visibili viene modellata in funzione della loro separazione angolare tridimensionale. Le statistiche, ottenute per diverse frequenze, sono approssimate con una distribuzione lognormale, i cui parametri sono descritti mediante funzioni continue dell'angolo di separazione. Nel complesso, i risultati forniscono strumenti utili per il dimensionamento e la progettazione di strategie di diversità in futuri sistemi NGSO operanti in banda EHF.

Parole chiave: costellazione NGSO, attenuazione da pioggia, Site Diversity, Orbital Diversity, ST-MultiEXCELL

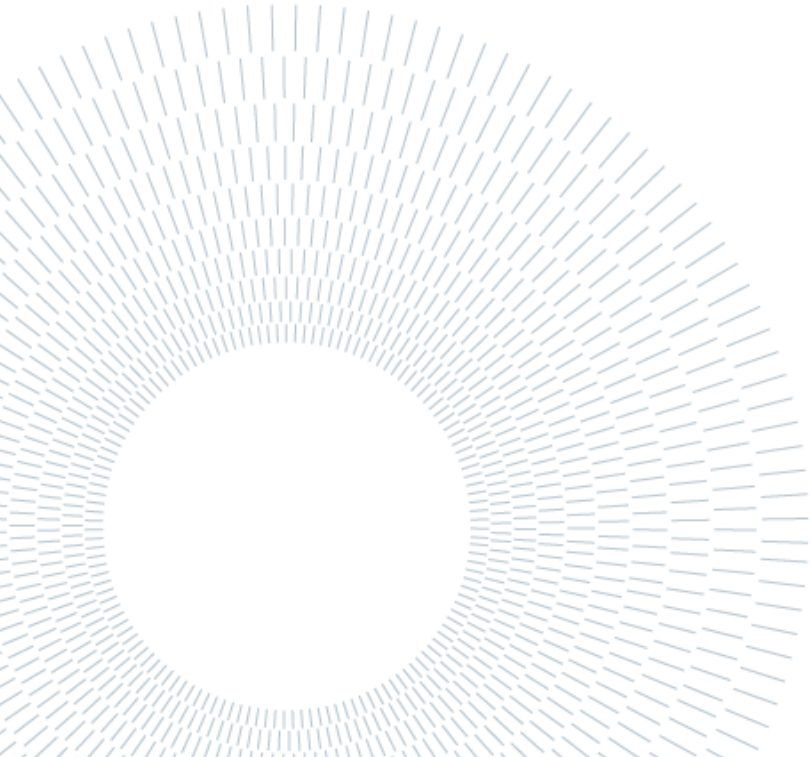

Contents

Introduction

Since 1964, when the first communication-oriented commercial satellite was launched (Syncom 3), Earth–space systems have been characterized by an incessant development becoming a key complement to terrestrial networks. Earth–space systems have evolved from simple broadcast services to complex broadband platforms capable of delivering high-speed Internet, supporting large volumes of data and providing enhanced coverage. As lower frequency bands become increasingly congested, satellite operators are progressively moving towards higher frequency ranges, such as Ka band (26-40 GHz) and, in perspective, Q/V (≈33-75 GHz) and W bands (75-110 GHz).

Traditionally, most commercial communication satellites have operated in Geostationary Orbit (GEO), at an altitude of about 35,786 km. In the last decade, however, the satellite communication landscape has been profoundly reshaped by the deployment of Non-Geostationary Orbit (NGSO) systems, including Medium Earth Orbit (MEO), Low Earth Orbit (LEO), Very Low Earth Orbit (VLEO) and Highly Elliptical Orbits (HEO). These orbits, collectively referred to as non-geosynchronous (non-GSO), do not share the GEO property of being stationary with respect to the Earth's surface. Therefore, individual NGSO satellites are visible from a given ground station only for limited time intervals and continuous service is guaranteed by deploying large constellations of satellites distributed over multiple orbital planes. The great interest in such satellite constellations is related to substantial advantages in terms of latency and global coverage, as well as to the more flexible and dynamic allocation of capacity enabled by NGSO architectures.

These benefits have motivated major commercial initiatives. A prominent example is Starlink: developed by SpaceX, the system is planned to consist of two sub-constellations, one at LEO with 4,425 satellites operating in the Ka and Ku bands, and another at VLEO with 7,518 satellites operating in the V band. However, this trend towards higher carrier frequencies and lower orbital altitudes comes with significant challenges from the propagation point of view.

Electromagnetic waves traveling along an Earth–space path interact with the troposphere, whose constituents impair the signal in several ways. The main propagation effects at high frequencies include phase delay and group delay,

depolarization, attenuation due to absorption and scattering, ray bending and phase fluctuations (scintillation). As the operating frequency exceeds approximately 10 GHz, attenuation due to hydrometeors – in particular rain, but also clouds – becomes progressively more severe. Gaseous absorption also contributes to the total attenuation and to the sky noise temperature, further degrading the signal-to-noise ratio (SNR) at the receiver.

These atmospheric effects are exacerbated in NGSO links. Because NGSO satellites spend a considerable fraction of the contact time at low elevation angles, the corresponding slant path through the troposphere is significantly longer than for high-elevation GEO links. As a result, rain attenuation can increase rapidly and vary strongly over time; scintillation and depolarization levels are also typically higher than in GEO scenarios. This leads to large dynamic variations of the received signal and poses stringent requirements on the dynamic range of the communication system. At high frequency bands, conventional link design approaches are often insufficient to guarantee the desired Quality of Service (QoS). In such conditions, the implementation of effective countermeasures becomes essential, motivating the improvement and development of accurate statistical prediction methods and channel models specifically tailored to NGSO constellations.

Given the critical impact of rain attenuation on high-frequency NGSO satellite links, Fade Mitigation Techniques (FMTs) play a key role in ensuring link availability and reliability: Site Diversity (SD) and Orbital Diversity (OD) are two well-established strategies that exploit spatial diversity to mitigate deep fades induced by intense precipitation. The former relies on the deployment of multiple, geographically separated Earth stations that are interconnected and concurrently communicate with the same satellite. Since heavy rain cells typically have limited spatial extent, it is unlikely that all sites within a diversity cluster experience severe attenuation at the same time. When the signal on one Earth–space path is strongly faded due to local rainfall, the system can switch to another station that is subject to less adverse meteorological conditions.

The latter exploits the fact that, in large NGSO constellations, a given Earth station can often see several satellites simultaneously at different elevation and azimuth angles. OD schemes select, at each instant, the satellite that provides the least attenuated path. As in SD, the goal is to ensure that the probability of experiencing simultaneous deep fades on all alternative paths remains much lower than the fade probability on any single link.

Both SD and OD are therefore promising FMTs for high-frequency NGSO satellite communication. Their proper design, however, requires detailed knowledge of the

statistical behaviour of atmospheric impairments along NGSO links, as well as of the correlation of rain attenuation across different sites and satellite pointing directions. At present, there is still no established statistical framework describing how NGSO satellite links are affected by tropospheric impairments, which motivates the analysis and modelling efforts presented in this thesis.

The first aim is to extend an existing simulator to address spatial diversity techniques and multi-link performance. The simulator operates with multiple Earth stations and a constellation of non-GSO satellites, in order to calculate the rain attenuation along the paths connecting the ground sites to each satellite.

Chapter 1 introduces the fundamentals of atmospheric impairments in satellite communications, from the effects of rain on the signal to the main prediction formulas and ITU-R recommendations used to model them. It also provides an overview of the development and main characteristics of NGSO satellite constellations, with particular emphasis on Fade Mitigation Techniques.

Chapter 2 describes the procedures adopted to implement the simulator and presents the different scenarios in which Site Diversity and Orbital Diversity are applied.

Chapter 3 focuses on the study of a statistical model that describes the behaviour of NGSO satellites in the troposphere, built upon the results obtained with the implemented simulator.

Finally, in *Chapter 4* are highlighted the main conclusions and proposed possible future works based on the present analysis.

1 Atmospheric Propagation and NGSO Satellite Systems

This chapter provides a brief introduction to atmospheric impairments affecting satellite communications, with particular focus on the impact of rain attenuation on satellite links. It then highlights the main characteristics of Non-Geostationary Orbit (NGSO) systems and describes their orbital representation.

1.1. Atmospheric impact on Earth-space links

Radio signals exchanged between satellites and ground stations must cross the Earth's atmosphere, whose layered structure introduces several propagation impairments. The two regions that mostly affect satellite links are the ionosphere and the troposphere.

The ionosphere, as shown in the schematic in *Figure 1.1*, extends roughly from 60 km to 1000 km altitude [1], and it is characterized by a high density of free electrons produced by solar UV and X-ray radiation. At low frequencies (below about 30 MHz), this region can act as a reflecting and strongly attenuating medium, enabling long-range high-frequency communication, but also introducing significant distortions. As frequency increases, ionospheric effects progressively weaken, and above a few GHz the ionosphere becomes almost transparent in terms of attenuation for most satellite applications. Residual effects such as Faraday rotation, delay, dispersion and scintillation are mainly relevant below 10 GHz and in specific geographical and geomagnetic conditions [2].

For satellite systems operating in the typical communication bands (Ku, Ka and above), the primary impairments arise in the troposphere, which extends from the ground up to about 10–15 km [3]. Hydrometeors (rain, snow, hail, cloud droplets and fog) and atmospheric gases (oxygen and water vapor) affect the signal through absorption, scattering, depolarization and emission noise. Among these phenomena, rain attenuation is generally the dominant impairment above 10 GHz, especially for high-availability links, while gaseous absorption and cloud attenuation provide a non-

negligible background contribution. The impact of these effects strongly depends on the elevation angle of the satellite with respect to the ground station. At low elevations, the radio wave travels along a longer slant path within the troposphere, so all tropospheric contributions become more severe. This behavior has been investigated in several experimental propagation campaigns. In the ITALSAT propagation experiment, carried out at the Spino d'Adda station (Milan, Italy), long-term measurements at 18.7, 39.6 and 49.5 GHz were collected from 1988 to 1992 on a fixed Earth-space link with an elevation angle of 37.7° [4]. The main objective of the experiment was the creation of an extensive database of propagation data representing the basis to devise and test prediction models. The dependance of attenuation statistics on the elevation angle has been highlighted by more recent experiments based on NGSO systems. In particular, results obtained within the MEKaP experiment [5] have shown that both the total attenuation and its short-term variability increase as the elevation angle decreases, and that the attenuation statistics become progressively more severe with increasing frequency. Low-elevation links were found to experience not only higher average attenuation, but also faster temporal fluctuations, reflecting the longer interaction path with spatially inhomogeneous rain structures.

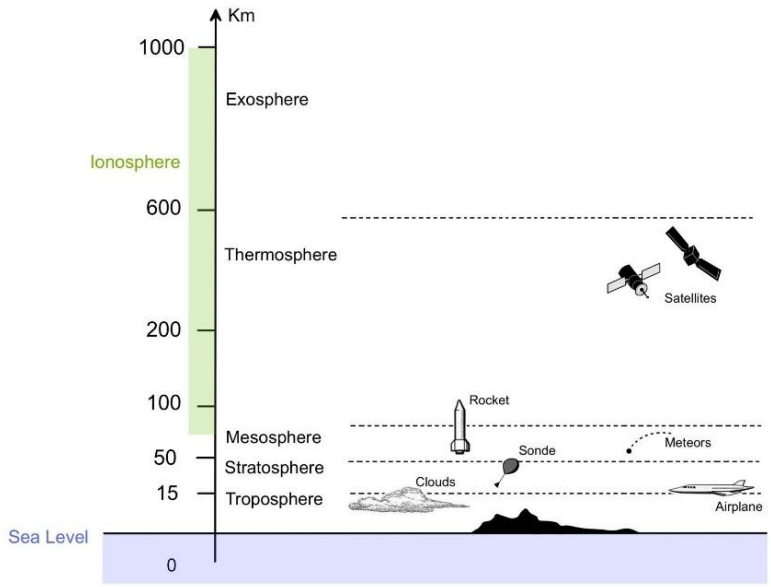

Figure 1.1: Schematic representation of the Earth's atmospheric layers, with altitude ranges and typical airborne and space systems.

In real propagation conditions, rain-induced attenuation exhibits a highly intermittent behaviour: long clear-sky periods alternate with rain events of variable intensity and duration. For high-frequency Earth–space links, even short and localized convective storms can produce deep fades (of the order of tens of dB) that severely degrade the signal-to-noise ratio, potentially leading to temporary outages if no countermeasures are implemented. Another key feature of rain is its marked spatial inhomogeneity. Rain cells have limited horizontal extent and exhibit strong rain-rate gradients over distances of only a few kilometers [6]. As a consequence, the attenuation affecting two nearby Earth–space links is only partially correlated. This limited spatial correlation is fundamental for diversity-based Fade Mitigation Techniques (FMTs), which exploit the uneven spatial distribution of rain to ensure that at least one low-attenuation path remains available at any time, if several properly spaced ground stations are considered.

To understand the physical origin of these effects, it is useful to recall how rain interacts with electromagnetic waves. Above 10 GHz, the wavelength of the radio wave becomes comparable with the typical raindrop diameter (roughly 0.1–8 mm), so the interaction between the electromagnetic wave and the drops becomes particularly significant. When a plane wave impinges on a raindrop, the incident power is partly absorbed and converted into heat and partly scattered away from the original propagation direction [7]. The combined effect of absorption and scattering removes power from the coherent wave: from a communication-system viewpoint, this is described as rain attenuation.

At a microscopic level, if a homogeneous rain volume of length L is considered, the average power of the wave decays exponentially along the path according to a Beer–Lambert law:

$$P_{\text{att}} = P_{\text{i}}\, e^{-kL}, \tag{1.1}$$

where P_{i} is the incident power and k is the attenuation coefficient of the rain medium. This coefficient can be expressed as

$$k = \rho\, Q_{\text{t}} = \rho\, (Q_{\text{abs}} + Q_{\text{sc}})\,, \tag{1.2}$$

where ρ is the number of drops per unit volume and Q_{t} is the total extinction cross-section of a single drop, which includes both absorption and scattering contributions.

In natural rainfall, however, the attenuation coefficient cannot be associated with a single drop size. Instead, it results from the superposition of contributions from a

population of drops with different radii, statistically described by the drop size distribution (DSD) $\eta(r)$:

$$k = \int Q_{\mathrm{t}}(r, \lambda, m)\, \eta(r)\, \mathrm{d}r, \tag{1.3}$$

where r is the drop radius, λ is the wavelength, m is the complex refractive index of water, and $\eta(r)$ represents the number of drops per unit volume with radius between r and $r + \mathrm{d}r$.

Early analytical models, such as the exponential distribution proposed by Marshall and Palmer [8], express the DSD as:

$$\eta(r) = N_0 e^{-\Lambda r} \tag{1.4}$$

where N_0 and Λ are parameters related to the rainfall intensity. Although more refined distributions have been proposed to account for different precipitation regimes (e.g. convective versus stratiform rain), it has been shown that the detailed shape of the DSD mainly affects second-order corrections, while the dominant dependence of attenuation on rain rate is preserved.

The rain attenuation over a path of length L is usually expressed in decibels as

$$A\,[\mathrm{dB}] = 10 \log_{10}\left(\frac{P_{\mathrm{i}}}{P_{\mathrm{att}}}\right), \tag{1.5}$$

Considering (1.1) and changing the base of the logarithm to the natural one, the rain attenuation can be expressed as

$$A\,[dB] = 4.343\; kL \tag{1.6}$$

It is convenient to introduce the specific attenuation γ_R in dB/km, defined such that the total attenuation caused by the rain volume is

$$A\,[dB] = \int_0^L \gamma_R\,(l)\,\mathrm{d}l \tag{1.7}$$

The integration is thus taken over the whole linear path crossed by the radio wave through the rain volume.

From (1.3) and (1.6) it is possible to state an expression for the specific attenuation that associates it to the size of the drop, the wavelength of the impinging wave, the extinction cross-section and the drop distribution in the considered volume:

$$\gamma_R \left[\frac{dB}{km}\right] = 4.343 \int Q_t(r, \lambda, m)\, \eta(r)\, dr \tag{1.8}$$

By combining the electromagnetic description of scattering and absorption with a statistical model of the drop size distribution, it can be shown that γ_R depends primarily on frequency and polarization of the wave, temperature, rain rate R (in mm/h) and on the elevation angle of the link. A fully analytical formulation is in general complex, because the drop size distribution and the corresponding scattering problem depend on the considered site, on the height and on the specific rain event. However, the widely adopted result is a power-law relationship between specific attenuation and local rain rate:

$$\gamma_R = k\, R^{\alpha} \tag{1.9}$$

where k and α are frequency- and polarization-dependent coefficients. This compact expression approximates very well the behavior of γ_R over a wide range of frequencies and rain rates and has become the standard basis for most rain-attenuation prediction models. ITU-R Recommendation P.838 [9] provides tables and interpolation formulas to obtain k and α for practical system configurations. The coefficients k and α implicitly embed all the relevant physical dependencies: the electromagnetic properties of water, the statistics of the drop size distribution, the operating frequency and polarization of the wave. In particular, α reflects how rapidly the contribution of larger drops increases with rain rate, while k acts as a scaling factor that grows rapidly with frequency. Both parameters also depend on polarization, since oblate raindrops introduce anisotropic scattering effects, leading to systematically higher attenuation for horizontally polarized waves. As stated before, at frequencies above approximately 10 GHz, the wavelength λ of the radio wave becomes comparable to typical drop diameters, and the scattering process transitions from the Rayleigh regime to the Mie regime. In this frequency range, the attenuation cross-section $Q_t(r, \lambda, m)$ cited in (1.3) exhibits quite a marked dependence on both drop size and complex refractive index of water, which in turn depends on temperature and frequency.

To apply the above concepts to the design of real satellite systems, the specific attenuation–rain rate relationship must be embedded in a procedure that accounts for link geometry and long-term rain statistics. The reference approach is provided by ITU-R Recommendations P.618, P.838 and P.839 [2],[9],[10].

Figure 1.2 provides a schematic representation of the ITU-R rain attenuation model, in which the rain region is assumed to extend from the ground up to the so-called rain height h_R. This parameter is defined in Recommendation ITU-R P.839 [10] as the sum

of the local 0 °C isotherm height and an additional offset accounting for the melting layer, where mixed-phase hydrometeors (melting snowflakes and ice particles coated with liquid water) exhibit scattering and absorption properties comparable to, and in some cases stronger than, those of liquid raindrops. Neglecting this layer would therefore lead to a systematic underestimation of attenuation, especially for slant paths at low elevation angles. Only the part of the Earth–space link lying below this height is affected by rain. For a given Earth station at height above mean sea level h_s and elevation angle θ, the corresponding slant path through the rain, L_s, is then determined from simple geometry, and can be expressed as

$$L_s = \frac{h_R - h_s}{\sin\theta} \tag{1.10}$$

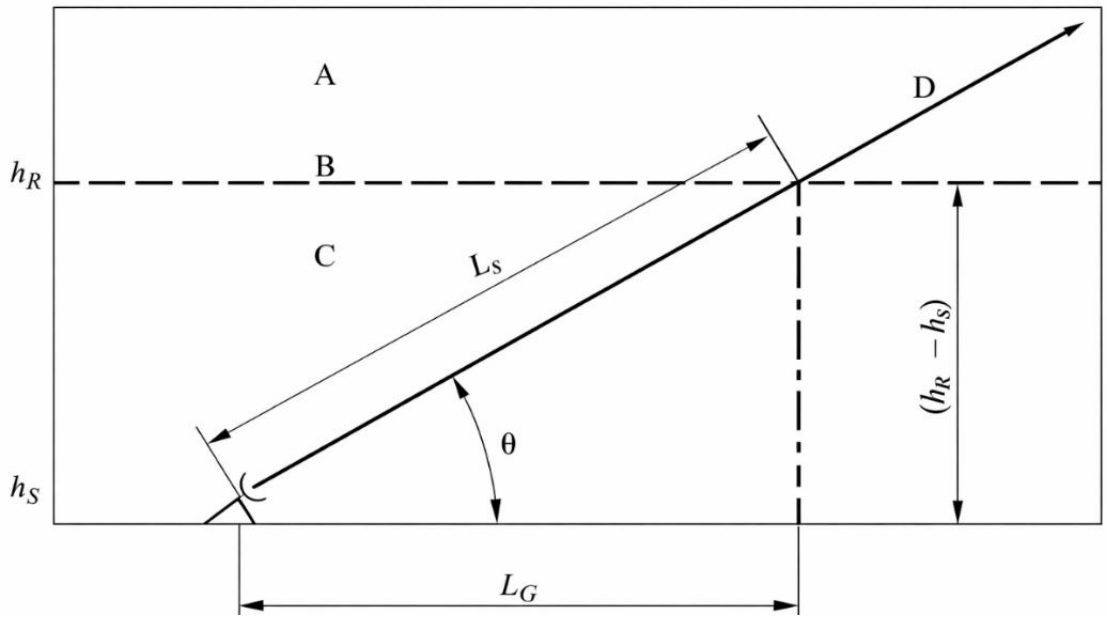

Figure 1.2: Schematic representation of an Earth-space link showing the parameters required as input to the attenuation prediction process (Source: ITU-R Recommendation P.618-14 [2]).

The assumption that the rain rate can be treated as approximately uniform along the vertical direction is a common and well-justified simplification in satellite propagation models. Over the vertical extent of the rain region, the dominant contribution to attenuation arises from the integrated effect of the precipitation column, while vertical gradients of rain rate introduce second-order corrections when compared to the much larger variability observed in the horizontal plane. By contrast, horizontal inhomogeneity represents the dominant source of variability in rain attenuation. Precipitation is organized in localized structures whose spatial scales typically range from a few kilometres for intense convective cells to several tens of kilometres for stratiform systems. This strong horizontal variability motivates the adoption of rain-cell-based models, in which the spatial distribution of rain rate is explicitly described through analytical profiles such as the exponential law:

$$R(\rho) = R_M e^{-\frac{\rho}{\rho_0}} \tag{1.11}$$

where R_M is the peak rain rate at the cell center, ρ is the radial distance from that center, and ρ_0 is an equivalent radius controlling the rate of decay. This formulation depicts how the rain rate reaches its maximum at the center of the cell and then decays rapidly with distance.

The fact that the main variability of rain occurs horizontally is particularly convenient for propagation calculations. The slant-path length L_s of the Earth–space link can be projected onto the ground as $L_G = L_s \cos\theta$, and the specific attenuation along this ground-projected path can be obtained from (1.9). The total attenuation on the slant path is then evaluated by integrating the specific attenuation along L_G and scaling the result by $1/\cos\ \theta$

$$A_G = \int_0^{L_G} \gamma_R(x)\, dx \tag{1.12a}$$

$$A_S = \int_0^{L_S} \gamma_R(l)\, dl = \frac{A_G}{\cos\theta} \tag{1.12b}$$

where x corresponds to the horizontal direction while l to the direction of propagation.

The procedure adopted for the development of the simulator described in this thesis, as will be explained in *Section 2.2.1*, also makes use of a model based on equation (1.9), relying on the above-mentioned Recommendations.

1.2. NGSO satellite constellations

1.2.1 Characteristics and historical development of NGSO satellite systems

Non-Geosynchronous Earth Orbits (NGSO) comprise all orbits for which the angular velocity of the satellite is not equal to the rotational velocity of the Earth, such as Low Earth Orbit (LEO), Very Low Earth Orbit (VLEO), Medium Earth Orbit (MEO) and Highly Elliptical Orbits (HEO) [11]. Unlike geostationary satellites, whose orbital period matches the Earth's rotation and which therefore remain fixed in the sky for a ground observer, NGSO satellites move rapidly across the celestial sphere and are visible from a given Earth station only for limited time intervals.

From a communication perspective, NGSO constellations are organized as networks of satellites distributed over multiple orbital planes, designed to guarantee that at least one satellite is in view of any user at any time. Satellites operating at LEO and VLEO are typically deployed at altitudes between 160 km and 2,500 km [12], yielding very short orbital periods (of the order of 90–120 minutes) and visibility windows of only a few minutes per pass (about 8–10 minutes before the satellite crosses the horizon).

MEO satellites fly at altitudes of roughly 10,000–20,000 km. At these heights, the one-way propagation delay is on the order of 100 ms and a single spacecraft can be tracked from the ground for up to about 2 hours. This orbital regime is widely used for navigation and positioning systems, as well as for some remote sensing and meteorological missions, with Global Positioning System (GPS) as the most well-known example (satellites at about 20,184 km). The orbital regimes introduced above are summarized in *Figure 1.3*, which schematically illustrates the altitude ranges of LEO and MEO orbits compared to GEO systems.

HEO are adopted to provide coverage over high-latitude regions that GEO satellites cannot serve adequately and for which longer visibility times are required than those offered by LEO. These orbits are markedly elliptical, with an apogee comparable to GEO altitude and a perigee closer to LEO, so that the satellite spends a large fraction of its orbital period near apogee over the target area. Consequently, the propagation delay experienced on HEO links varies significantly along the orbit, taking values from roughly 10 ms up to about 260 ms [13].

NGSO constellations offer several advantages over traditional GEO systems. The most evident benefit is the shorter distance between satellite and ground station, which translates into lower free-space path loss and significantly reduced propagation delay, enabling low-latency services and more energy-efficient transmissions, particularly at LEO and MEO altitudes. Moreover, since NGSO satellites overfly a wide range of

latitudes, they can ensure good coverage at high latitudes and even in polar regions, where GEO satellites are seen at very low elevation or may not be visible at all [14]. By appropriately designing orbital planes, the number of satellites per plane and the antenna footprints, system capacity can also be flexibly steered in space and time, concentrating resources where and when traffic demand is highest.

These advantages, however, come at the cost of increased complexity and specific design challenges. Continuous global or near-global coverage requires a large number of satellites and carefully optimized constellation geometries, which complicates deployment, operations and end-of-life management. In addition, NGSO systems often operate in the same Ku, Ka and Q/V bands used by existing GEO fixed-satellite services, so spectrum sharing and interference at GEO gateways become critical issues. Coordination mechanisms and equivalent power flux-density limits are therefore imposed to ensure that NGSO emissions do not degrade GSO link availability beyond prescribed thresholds [15]. Finally, NGSO satellites spend a significant fraction of their visibility time at low elevation angles, where the slant path through the troposphere is long; as stated in *Section 1.1*, at frequencies exceeding 10 GHz, NGSO links become particularly vulnerable to atmospheric impairments, with rain attenuation playing a dominant role on high-frequency feeder and user links.

All these challenging features have led to a notable evolution of NGSO systems. The historical development of NGSO constellations is often described in two "waves" [16]. The first wave, in the 1990s, was driven by the ambition to provide truly global telephony and low-rate data services. Systems such as Iridium and Globalstar, and projects like Teledesic, explored large LEO constellations to complement or bypass terrestrial networks. These systems introduced many of the architectural concepts that are now standard for NGSO constellations, including polar and inclined orbit shells, inter-satellite links and global gateway networks. However, they emerged in a context of high launch costs, relatively immature satellite manufacturing capabilities and rapidly expanding terrestrial cellular networks, which limited their long-term economic viability.

A second wave of NGSO constellations began around the mid-2010s and continues today. This wave is characterized by the so-called "mega-constellations" comprising hundreds or thousands of satellites, designed primarily for broadband Internet access rather than narrowband telephony. SpaceX's Starlink, OneWeb, Telesat's Lightspeed and Amazon's Kuiper, together with emerging governmental projects such as the European IRIS² constellation, are emblematic of this phase. Their emergence has been enabled by several technological and economic factors: reusable launch vehicles that dramatically reduce launch cost per kilogram; industrialized, mass-production

approaches to satellite manufacturing; advanced phased-array antennas capable of generating and steering multiple beams and powerful on-board processing suitable for routing and regenerative payloads. This second wave is therefore reshaping the role of NGSO constellations within the overall satellite communication ecosystem and motivates a renewed focus on propagation modelling and system-level performance.

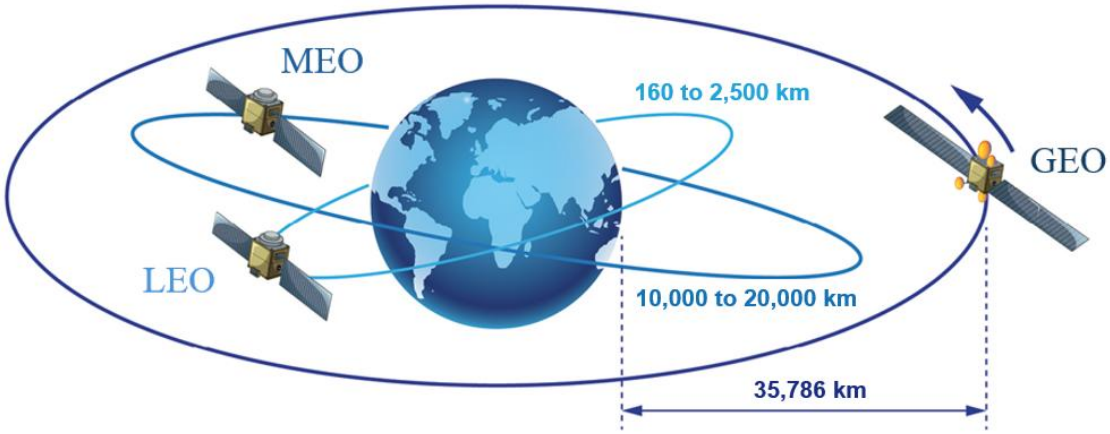

Figure 1.3: Comparison of coverage and distance of GEO, MEO and LEO satellites (Source: J. Keenan, SpaceVPX — Enabling the Next Generation of Satellite Constellations, VITA Technologies, Apr. 17, 2019.)

1.2.2 Reference frames for NGSO orbit description

To describe the motion of NGSO satellites and to compute link geometry it is necessary to introduce a set of reference systems. A natural starting point is a Cartesian coordinate system with three axes, but in practice different realizations are used depending on the task. The adopted reference frames are illustrated in *Figure1.4.*

The Earth-Centered Inertial (ECI) frame is an inertial-like, non-rotating reference system whose origin coincides with the Earth's center of mass, while the axes are fixed with respect to the distant stars. In this frame, the satellite trajectory is governed directly by orbital dynamics and can be conveniently expressed using the classical Keplerian elements (semi-major axis, eccentricity, inclination, right ascension of the ascending node, argument of perigee and anomaly). This description is well suited for orbit propagation and for implementing standard models such as SGP4 [17], which propagate satellite state vectors using Two-Line Element (TLE) sets.

For link budget calculations, however, an Earth-fixed description is more practical. This is provided by the Earth-Centered, Earth-Fixed (ECEF) frame, which shares the same origin (Earth's center of mass) as the ECI frame, but rotates with the Earth. In ECEF, the z-axis passes through the North Pole, the x-axis lies in the equatorial plane intersecting the prime meridian, and the y-axis completes a right-handed system. Because ECEF follows the Earth's rotation, positions of ground stations are time-invariant in this frame, and line-of-sight vectors from a station to a satellite can be easily computed by subtracting their Cartesian coordinates.

While ECEF is convenient for vector algebra, it does not directly account for the ellipsoidal shape of the Earth. For this reason, positions on the surface are usually given in a geodetic (ellipsoidal) reference system, specified by latitude, longitude and altitude above a reference ellipsoid. The widely adopted WGS-84 ellipsoid provides a consistent global standard and it is used by GNSS systems and most orbit and propagation tools. Geodetic coordinates offer an intuitive description of the ground station location and are easily converted to ECEF through well-known transformations.

In satellite communications, these three representations are typically combined in a processing chain. The satellite orbit is propagated in an inertial frame (ECI) using Keplerian elements or TLE-based models. At each time step, the satellite state is rotated into the ECEF frame through a suitable Earth-rotation transformation. Then, both satellite and ground station positions are expressed in Cartesian ECEF coordinates, allowing direct computation of the line-of-sight vector and thus of the slant range. Finally, this vector is projected into a local topocentric (horizon) frame

centered on the station to derive azimuth and elevation angles, which are essential for antenna pointing, for determining visibility windows and for evaluating the path length through the troposphere.

In the context of NGSO constellations, this consistent handling of reference frames is particularly important: the rapid motion of LEO and MEO satellites leads to quickly varying elevation angles and slant ranges, which in turn cause large temporal variations of atmospheric attenuation and of the link budget. A rigorous orbital description, coupled with appropriate coordinate transformations, is therefore a prerequisite for any realistic simulation of NGSO systems and for the subsequent analysis of fading statistics and mitigation strategies.

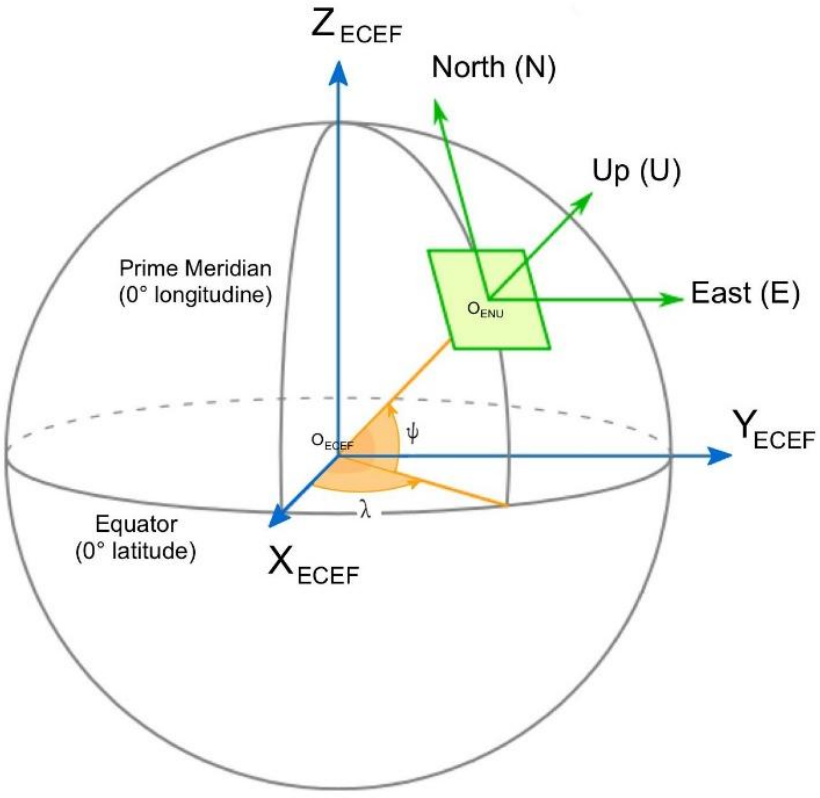

Figure 1.4: Relationships between Geodetic, ECEF and ENU coordinate systems.

1.2.3 Fade Mitigation Techniques for NGSO constellation

For NGSO constellations operating at Ku, Ka, Q and V bands, the combination of high frequencies, large slant paths at low elevation and stringent availability targets makes FMTs essentially mandatory. The general idea of FMTs is to mitigate propagation-induced fades either by adapting the physical-layer parameters of the link or by exploiting diversity in time, frequency or space.

A first class of FMTs operates at the physical layer and includes techniques such as uplink power control (UPC), adaptive modulation and coding (AMC) and data-rate adaptation. Uplink power control compensates for attenuation by increasing the transmitted power during fades, within the limits imposed by satellite amplifier saturation and interference constraints. AMC and data-rate adaptation dynamically adjust the modulation order and coding rate according to the instantaneous channel conditions, trading spectral efficiency for robustness in the presence of rain-induced signal degradation. These techniques are widely adopted in modern satellite systems and are extensively covered in ITU-R recommendations and DVB-S2/S2X standards [18]. However, their effectiveness is ultimately constrained by the available power margin and by the temporal dynamics of rain fades, which can be particularly severe at high frequencies.

Another mitigation approach is time diversity, which relies on the temporal decorrelation of rain attenuation, allowing transmissions to be scheduled or repeated when propagation conditions improve. By retransmitting data or using interleaving over sufficiently long-time intervals, the probability that all replicas experience deep attenuation is reduced. While time diversity can be effective for delay-tolerant services, it is generally less suitable for low-latency applications and real-time traffic, which are key targets of NGSO systems.

In contrast, geometric diversity techniques operate at the network level by exploiting the availability of multiple alternative Earth–space propagation paths affected by partially uncorrelated rain attenuation. Among these techniques, Site Diversity (SD) and Orbital Diversity (OD) are particularly well suited to NGSO constellations, where multiple gateways and multiple satellites are inherently available. Unlike power- or waveform-based mitigation strategies, geometric diversity does not rely on increased transmit power or additional physical-layer margins, but rather on the spatial structure of the propagation environment. For this reason, and because their effectiveness is tightly coupled to rain spatial variability and link geometry, SD, OD and their joint application constitute the focus of this thesis.

Site Diversity

SD exploits the limited horizontal extent (from a few kilometers to a few tens of kilometers) and the spatial inhomogeneity of intense rain cells [19]. Convective rain cells typically span a few kilometres, while even larger stratiform systems exhibit significant spatial variability in rain intensity. Since heavy precipitation typically affects only a portion of a region at any given time, if two or more Earth stations are separated by a distance D large enough, it becomes unlikely that all of them are simultaneously affected by the same severe rain event.

In a generic dual-site diversity scheme, two ground stations are deployed within the same service area, all connected to the same satellite(s), so that the satellite signal is received simultaneously at the diversity sites. Let $A_1(t)$ and $A_2(t)$ denote the rain attenuation on the two links at a given time t and let $P_S(A)$ be the single-site complementary cumulative distribution function (CCDF) of attenuation for either site. The joint CCDF of rain attenuation for SD is

$$P_j(A_1 \geq a_1,\ A_2 \geq a_2) \tag{1.13}$$

and directly quantifies the probability that both links exceed given attenuation thresholds a_1 and a_2. This joint behaviour directly reflects the spatial correlation of the rain field at the scale of the site separation. In practical systems, SD is commonly implemented through selection combining: at each time instant, traffic is routed through the site experiencing the lowest attenuation. For a system with N diversity sites, the effective attenuation is therefore

$$A_{\mathrm{SD}}(t) = \min\{A_1(t), A_2(t), \ldots, A_N(t)\} \tag{1.14}$$

The effectiveness of SD is usually expressed through the diversity gain, in dB and defined at a given exceedance probability p as

$$G(D, A_S) = A_S(p) - A_j(D, p) \tag{1.15}$$

where $A_s(p)$ is the attenuation exceeded with probability p on a single link, and $A_j(D, p)$ is the attenuation exceeded with the same probability for the diversity system (i.e. after selecting the best site). In general, diversity gain increases with site separation distance, operating frequency and required fade margin, since higher frequencies and rarer events are associated with more localised and less correlated rain structures.

From a modelling viewpoint, SD analysis requires two main ingredients. The first is an accurate description of single-site attenuation statistics, often modelled as lognormal in time and derived from long-term rain-rate measurements, with CCDF:

$$P_s(A) = P_{\text{rain}}\, Q\left(\frac{\ln A - \mu_A}{\sigma_A}\right) \tag{1.16}$$

where $Q(\cdot)$ is the complementary Gaussian CDF, and μ_A, σ_A are fitted to the 1-minute rain-rate statistics at the site.

The second is a model for the spatial correlation of rain attenuation, usually expressed in terms of the correlation of the logarithmic attenuation as a function of inter-site distance. Experimental studies have shown that this correlation function is expressed as a sum of decaying exponentials in D, reflecting a rapidly decorrelation at short distances and a slower tail at larger scales, mirroring the coexistence of different precipitation regimes.

For NGSO links, SD presents additional complexity: the elevation angles of the different links may differ significantly and vary in time, altering both the slant path lengths and the correlation structure of rain attenuation. To account for this, dedicated models must be used that explicitly incorporate the dependence of the attenuation correlation on both site separation and elevation angle, allowing the prediction of joint attenuation statistics and diversity gain for NGSO systems.

Orbital Diversity

OD exploits the simultaneous visibility of multiple satellites from a single ground station. In a large NGSO constellation, at any given time, a gateway or user terminal generally has access to several satellites located at different positions along the orbit, and therefore observed under different azimuth and elevation angles [20]. The rain attenuation affecting the links between a ground station and the N_{sat} satellites visible at time t is:

$$\{A_i(t)\}_{i=1}^{N_{sat}} \tag{1.17}$$

OD operates by continuously monitoring the link quality (e.g. attenuation or SNR) for each visible satellite and by dynamically selecting, at each time instant, the satellite providing the most favourable propagation conditions, which in the simplest case corresponds to minimising the instantaneous attenuation:

$$A_{OD}(t) = \min_{1 \le i \le N_{sat}} A_i(t) \tag{1.18}$$

The CCDF of A_{OD} then defines the OD performance, and the corresponding diversity gain (in dB) is obtained by comparison with the single-link statistics:

$$G_{OD}(A_S) = A_S(p) - A_{OD}(p) \tag{1.19}$$

As with SD, the performance of OD is governed by the geometry of satellite links. Here, the key parameter is the angular separation between the alternative links. Satellites observed at sufficiently different azimuth and elevation angles traverse distinct portions of the rain field, leading to partial decorrelation of the attenuation processes. Larger angular separations and higher elevation differences generally enhance OD performance, as they increase the likelihood that at least one link avoids the most intense precipitation regions. However, because all links originate from the same ground station, the differential effect is generally smaller than for widely spaced sites, which partly justifies the superiority of SD, especially when the fading margins required are high. Even though SD is technically preferable, cost effectiveness might be a crucial factor when having to decide between the two diversity alternatives. Indeed, SD systems require two Earth station installations along with a terrestrial connection, whereas OD operates on a common resource basis requiring additional bandwidth and an appropriate switching algorithm to process the data streams collected at the Earth station. Therefore, since OD systems operate at considerably lower Earth segment costs, a clear criterion must be established for system engineers to select between SD, which is technically superior, and OD, which is more cost effective from a system point of view [21]. A simplified configuration of SD and OD scenarios is reported in *Figure 1.5*.

Joint Site-and-Orbital Diversity

In realistic NGSO architectures, SD and OD are not mutually exclusive and can be jointly exploited to maximise resilience against rain-induced fading. In a joint diversity scheme, multiple ground stations are deployed, each with simultaneous access to multiple satellites. Let $\mathcal{K}$ be the set of ground stations and $\mathcal{S}_k$ the set of satellites visible from station k. The most general diversity strategy is to select, at each instant, the path (k, i) that minimizes attenuation:

$$A_{\mathrm{joint}}(t) = \min_{k \in \mathcal{K}} \min_{i \in \mathcal{S}_k} A_{k,i}(t) \tag{1.20}$$

The CCDF of A_{joint} quantifies the performance of a system that can route traffic through multiple gateways and multiple satellites, subject to network and resource-allocation constraints.

Joint diversity combines the large-scale spatial decorrelation provided by SD with the finer angular diversity offered by OD and therefore represents the most powerful mitigation strategy from a purely propagation-oriented viewpoint. Its performance depends on a wide range of parameters, including site separation distances, satellite angular distribution, elevation angle statistics, climate and frequency band.

For future high-frequency NGSO systems, FMTs design cannot rely on single-link statistics only. Instead, it requires an integrated framework combining realistic space–time rain-field models (such as ST-MultiEXCELL described in *Section 2.1.2*), detailed orbit and coverage simulations for large constellations and appropriate analytical or semi-empirical models for joint attenuation statistics. In the remainder of this thesis, these concepts and models provide the theoretical basis for the simulation methodology and for the interpretation of the results obtained for SD, OD and their combination in NGSO constellations.

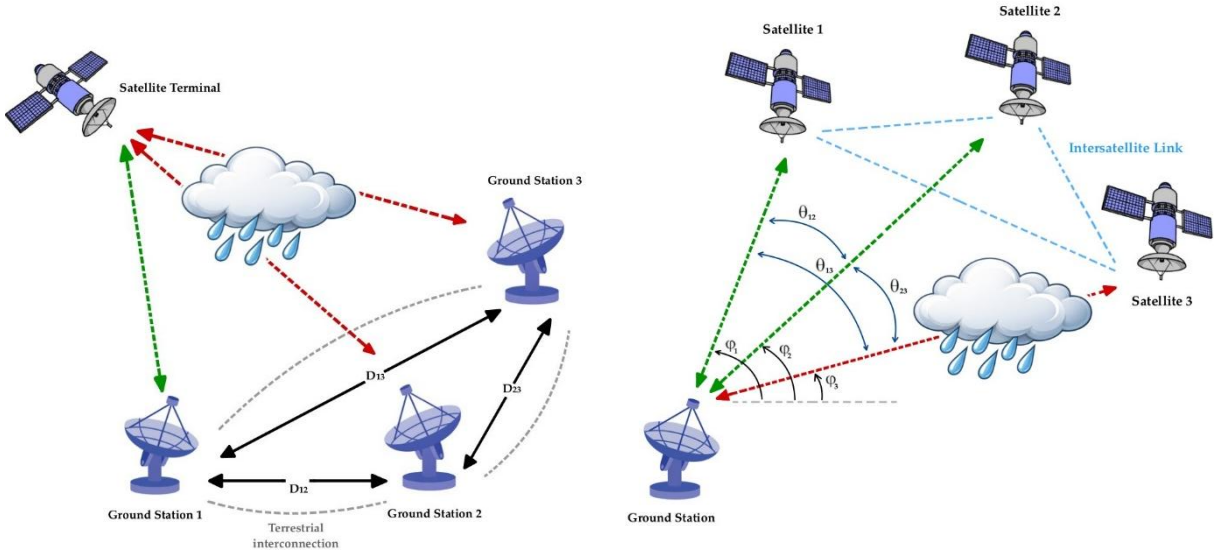

(a) (b)

Figure 1.5: Indicative paradigm of the examined diversity scenarios.
(a) Site Diversity. (b) Orbital Diversity

2 Framework and Methodology

The simulation framework adopted in this work is derived from the rain attenuation and interference simulator developed by Enrico Polo, PhD Student at Politecnico di Milano [22]. The original simulator was explicitly conceived to analyze co-frequency interference between a GSO satellite link and a large NGSO constellation operating at 40 GHz, under realistic atmospheric propagation conditions.

The simulator operated with a single Earth station, placed at the center of a 200 km × 200 km rain map, and combined space–time rain fields with NGSO orbital data. For each time instant, the tool identified the set of NGSO satellites simultaneously visible from the ground station and potentially interfering with the GSO link. This selection was based on geometric criteria, including the avoidance angle between the GSO line-of-sight and the NGSO satellite directions and the number of co-frequency interfering satellites (N_{co}). For each interfering NGSO satellite, the simulator computed the rain attenuation along the corresponding Earth–space path and evaluated the received interfering power at the ground station. In parallel, the rain-attenuated received power of the GSO link was calculated. A complete power-budget formulation was therefore implemented for both the GSO signal and the aggregate NGSO interference. By combining these contributions in linear units, the simulator produced time series of the carrier-to-interference ratio (CIR) at the ground station, enabling a statistical assessment of GSO link degradation due to NGSO interference in the presence of rain.

Building upon this framework, the present work shifts the focus from GSO–NGSO coexistence to NGSO-only scenarios, extending the simulator capabilities to address spatial diversity techniques and multi-link performance.

It is worth stressing that the input data and the initialization procedures of the simulator remain consistent with those that will be described in *Sections 2.1* and *2.2.* These elements constitute the fixed baseline of the simulation framework. All subsequent developments are therefore built upon the same rain-field realizations, satellite ephemerides and propagation assumptions, ensuring full consistency and comparability with the original simulator architecture. The main contributions of this thesis concern the extension to multi-site configurations, the introduction of flexible ground-station geometries and the enforcement of satellite visibility constraints for the systematic analysis of SD, OD and their joint application in NGSO-only scenarios.

2.1. Rain Field Models

Over the years, several types of rain field models have been proposed for propagation studies. Numerical weather models can reproduce the full meteorological environment with high physical accuracy, but they are usually too computationally demanding for routine simulations at 1-minute resolution. Stochastic and statistical models are more efficient and can be tuned to match local rainfall statistics, although they often rely on simplified assumptions about distributions or correlation structures and may require long rain-gauge time series for calibration. Fractal models, in turn, exploit self-similarity properties of precipitation fields, but depend on input parameters that are not always straightforward to infer from available data.

In this context, the developed simulator requires as input realistic rain fields to compute rain attenuation on multiple Earth–space links. Simple point-based models are inadequate for multi-link NGSO scenarios with diversity techniques, where spatial correlation and temporal evolution of rain are crucial. For these reasons, a family of cell-based rain field models is adopted here, culminating in the ST-MultiEXCELL model used in the simulations. They are briefly described in the following sections hereinafter below.

2.1.1. EXCELL and MultiEXCELL

In cell-based models, the rain field is described as a collection of rain cells. A rain cell is defined as a connected region where the rain rate exceeds a predefined threshold. Each cell is associated with an analytical horizontal profile, which captures how the rain rate decays away from the cell center. The theoretical representation of rain rate for a single cell has an exponential form:

$$R(\rho) = R_M \exp[-(\rho/\rho_0)^{2/k}], \tag{2.1}$$

where R [mm/h] is the rain rate, ρ [km] is the distance from the cell center, R_M [mm/h] is the maximum rain rate occurring at the center of the cell, and ρ_0 [km] is the equivalent radius for which R = R_M/e [23]. *Figure 2.1* shows a schematic of a rain cell, identifying the mentioned parameter. Equation (2.1) distinguishes multiple profiles, depending on k chosen. The shape factor, k = 1, k = 2 or k = 3, respectively defines Gaussian, exponential or hyper-exponential cell profiles. Capsoni et al. [24] stated that the exponential profile (k = 2) fits the best with the experimental results.

The EXCELL model (EXponential CELL) is the first implementation of this approach. Its main feature is that it links the statistical properties of the generated cells to the local 1-minute rain rate statistics $P(R)$ of the site under study. Starting from the

measured complementary cumulative distribution function of the rain rate, EXCELL derives the occurrence probability and the parameters of the cells so that the ensemble of synthetic events reproduces the observed $P(R)$. This allows the model to be tuned to different climatic conditions using only standard rain-gauge statistics. However, EXCELL is essentially limited to isolated cells and small areas: it does not describe how multiple cells group together to form larger precipitation systems, nor does it naturally extend to domains of hundreds of kilometres.

To overcome these limitations and to obtain a large-scale model, the Multi EXponential CELL model was introduced [25]. MultiEXCELL preserves the exponential description of individual cells, but adds a statistical characterization of cell aggregation into clusters. An example of the synthetic rain fields generated by the MultiEXCELL model is reported in *Figure 2.2*. These statistics were extracted from long-term radar measurements collected at the Spino d'Adda experimental station (Milan, Italy), where rain events were observed over several years with high spatial and temporal resolution. On this basis, MultiEXCELL can generate synthetic rain fields that reproduce both the local rain-rate CCDF, and the spatial correlation structure of the precipitation. The main limitation of MultiEXCELL, though, is that it treats each map as an independent realization: it does not impose any temporal correlation between successive fields. For propagation studies that require time series (e.g. for dynamic link simulations), this is a significant drawback. This motivated the development of an extended model, ST-MultiEXCELL, capable of reproducing both the spatial and temporal behaviour of rain.

2.1.2. ST-MultiEXCELL

The ST-MultiEXCELL (Space–Time MultiEXponential CELL) model extends MultiEXCELL by introducing a physically motivated description of the temporal evolution of rain fields, while preserving their realistic spatial structure [27]. Like its predecessor, it generates rain fields that match the local rain-rate CCDF $P(R)$, but it also reproduces the time correlation of the rainfall process.

Two related quantities are central to the time-domain characterization: the fractional rainy area η_P, defined as the fraction of the map where the rain rate exceeds a specified threshold, and the rainy area η, defined more strictly as the area where the rain rate exceeds a fixed threshold (0.5 mm/h for this model). The evolution of η and η_P depends on the type and on the duration of the precipitation event. ST-MultiEXCELL distinguishes between two main classes: stratiform rain, typically associated with a large covered area, relatively low rain rates (usually below about 10 mm/h [28]) and

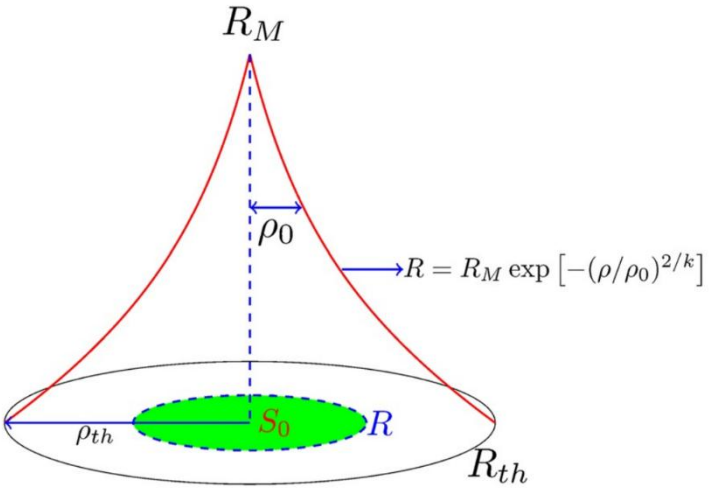

Figure 2.1: Typical rain cell in MultiEXCELL model [23].

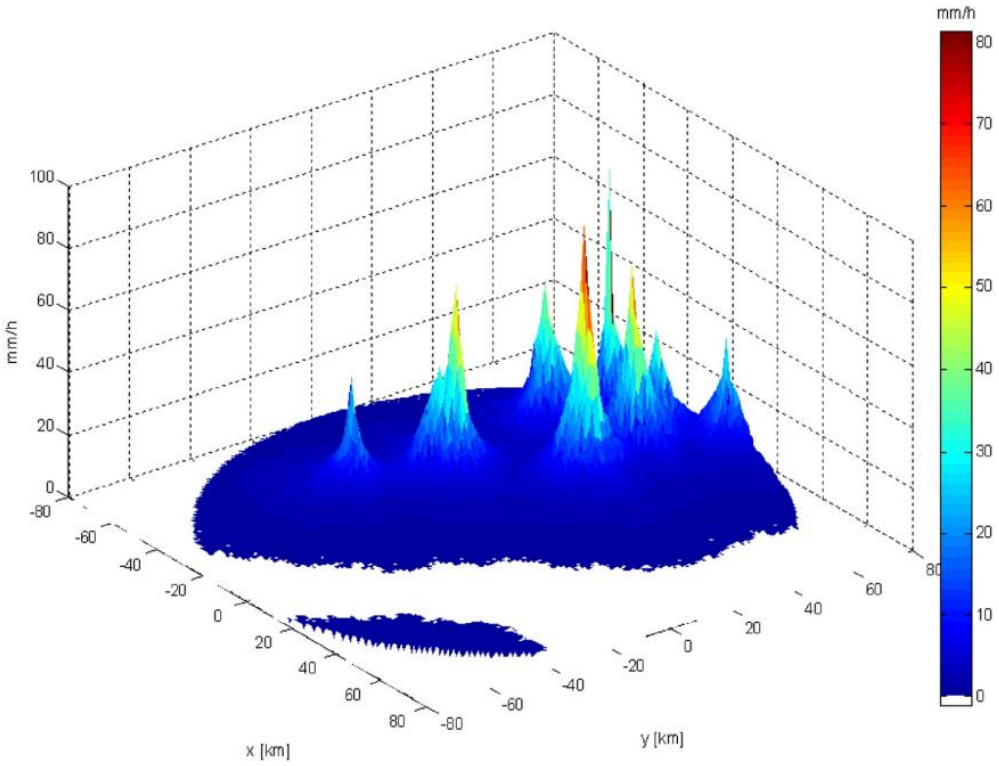

Figure 2.2: Example of the synthetic rain fields generated by the Multi EXponential CELL model [26].

long-lasting events, whereas convective rain is characterized by high rain rates, more localized cells and shorter lifetimes.
These regimes exhibit different temporal behaviour: convective cells tend to be smaller and more intense, with rapid changes in size and intensity, whereas stratiform precipitation evolves more smoothly and slowly. ST-MultiEXCELL accounts for these differences by prescribing distinct temporal laws for the variation of cell parameters (e.g. equivalent radius and peak rain rate) depending on the event type.

To parameterize the temporal evolution, the model exploits Numerical Weather Prediction data (ERA-40), which are organized in 6-hour slots. This organization is particularly convenient for studying how η and η_P evolve during rainy periods and for distinguishing different types of events. The same dataset is used to derive realistic statistics of wind speed v and wind direction θ at the site under consideration, which determine the advection of the precipitation system across the domain. In other words, in addition to structural changes in the cells (intensification, weakening, appearance and disappearance), ST-MultiEXCELL also models the horizontal displacement of the rain field driven by the local wind.

In its standard configuration, ST-MultiEXCELL produces rain events over a square domain of 200 km × 200 km, with 1 km × 1 km spatial resolution and 1-minute temporal resolution. Each event has a duration of 6 hours and consists of 359 consecutive rain maps, where each pixel contains the instantaneous rain rate in mm/h for the corresponding 1 km × 1 km area. For each synthetic event, the model ensures that the local rain-rate statistics $P(R)$ over the year are preserved, the spatial correlation length scales of the rain field are consistent with radar observations and the temporal evolution of η and η_P follows realistic trajectories derived from ERA-40. Comparisons with measurements at Spino d'Adda station (Milan, Italy) have shown that ST-MultiEXCELL is able to reproduce both the local rainfall statistics and the space–time correlation of the rain process, while overcoming the main limitation of MultiEXCELL, namely the absence of time correlation in the generated fields. In *Figure 2.3* it is possible to see an example of the evolution of a rain field generated by ST-MultiEXCELL for Milan, Italy.

In the context of this thesis, ST-MultiEXCELL provides the synthetic rain input to the attenuation simulator. At each time step, the simulator reads the rain maps generated by ST-MultiEXCELL and uses the rain rate values associated with the pixels intersected by each Earth–space link to compute the corresponding specific attenuation γ_R and, by integration along the slant path, the total rain attenuation. This framework makes it possible to simulate, in a consistent way, the impact of realistic, space–time correlated precipitation on multiple NGSO links and to assess the performance of diversity-based FMTs.

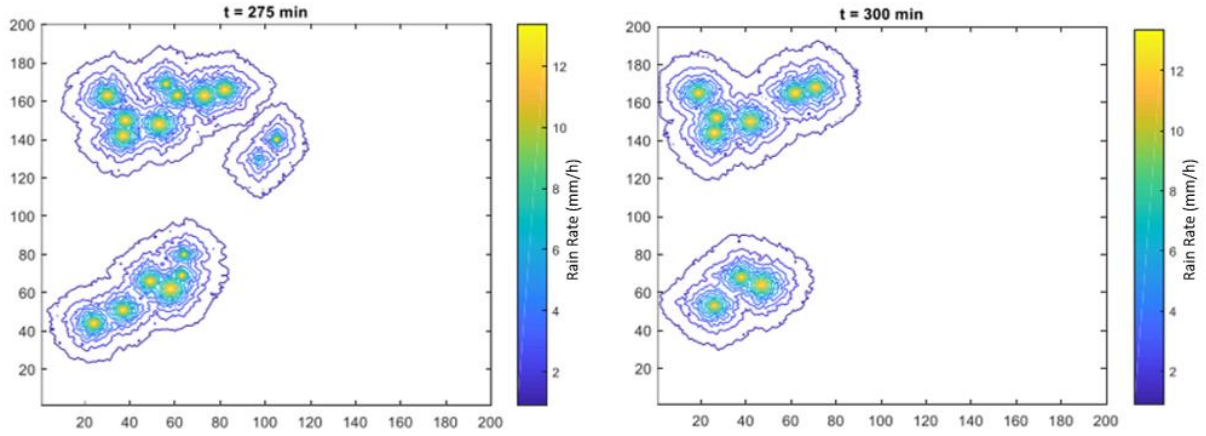

Figure 2.3: Evolution of a rain field generated by ST-MultiEXCELL for Milan, Italy [27].

2.2. Input and Geometric Initialization

The starting point of the simulator is a three-dimensional rain field, obtained by stacking the two-dimensional rain maps produced by ST-MultiEXCELL along the vertical direction. Each rain event covers a geographical area of 200 km × 200 km with a spatial resolution of 1 km × 1 km and a temporal resolution of 1 minute. The maps correspond, in practice, to 200×200 matrices, where each cell contains the instantaneous rain rate in mm/h for the associated pixel. To obtain a smoother evolution in time, the simulator increases the effective temporal resolution from 60 s to 30 s by interpolating between consecutive maps: each pair of successive ST-MultiEXCELL maps is averaged elementwise, inserting an additional "intermediate" map. As a result, each 6-hour event (originally 359 maps) is represented by 717 maps with a time step of 30 seconds.

The simulator requires as input the geodetic coordinates (latitude, longitude, altitude) of the ground station(s) and the geodetic coordinates of each NGSO satellite as a function of time. These data were made available through a collaboration with SES S.A., which provided the orbital information of the SpaceX VLEO sub-constellation in geodetic form.

The available orbital data describes the 7,518 satellites of the VLEO constellation listed in *Table 2.1* and *Table 2.2*, over a time span of 5 days with a sampling interval of 10 seconds. By contrast, the rain events produced by ST-MultiEXCELL extend over an entire year, yielding 1,460 six-hour slots. A key objective of the simulator is to associate, for each rain map, the corresponding positions of all satellites in the constellation at the same instant of time. Since rain fields are analyzed with a temporal

Table 2.1: Table describing SpaceX LEO constellation's parameters. Source: Table A.2-1 [29].

Parameter	Initial Deployment (1,600 satellites)	Final Deployment (2,825 satellites)			
Orbital Planes	32	32	8	5	6
Satellites per Plane	50	50	50	75	75
Altitude	1,150 km	1,110 km	1,120 km	1,275 km	1,325 km
Inclination	53°	53.8°	74°	81°	70°

Table 2.2: Table describing SpaceX VLEO constellation's parameters. Source: Table A.2-2 [29].

Parameter	Deployment		
	2,547	2,478	2,493
Satellites per Altitude	345.6 km	340.8 km	335.9 km
Altitude	1,150 km	1,120 km	1,275 km
Inclination	53°	48°	42°

resolution of 30 seconds, the orbital dataset is accordingly resampled so that only epochs that are multiples of 30 seconds are retained. For simplicity, once the 5-day orbital sequence has been fully used, it is repeated cyclically, resulting in 73 repetitions over one year. This choice does not affect the validity of the model, as the simulator is intended to analyze long-term simulated data and a 5-day period is sufficient to sample all relative configurations of LEO satellites within their orbital planes.

The first step in the procedure of the simulator is to load the orbital data of the constellation, as well as the geodetic coordinates of both the ground station(s) and the considered satellites. Both satellite and ground-station coordinates are first expressed with respect to a reference ellipsoid; in this work, the WGS-84 ellipsoid is adopted. The orbital data, in the practical case, correspond to a matrix of dimensions 7,518×3×14,401, in which each row is associated to one of the 7,518 satellites orbiting in LEO, the columns describe the latitude, longitude and altitude respectively of the selected satellite, while the third dimension refers to the evolution in time of the constellation for every 30 seconds. The geodetic coordinates are then converted to ECEF. As stated in *Section 1.2.2*, this reference system is indeed the most practical for calculations involving line of sight objects in space. After the conversion, what is obtained is a set of Cartesian coordinates (x, y, z). This transformation allows standard Euclidean geometry to be used: any position in space is represented by a vector from the Earth's centre of mass, and relative position vectors (for example, from the ground station to each satellite) are obtained by simple subtraction:

$$\mathbf{r}_{\text{sat/gs}} = \mathbf{r}_{\text{sat}} - \mathbf{r}_{\text{gs}} \tag{2.2}$$

These relative vectors describe the slant paths between the ground station and the NGSO satellites and are also convenient for angle calculations. The elevation angle of the link is obtained by projecting $\mathbf{r}_{\text{sat/gs}}$ onto the local topocentric (East–North–Up) frame at the ground station and computing the angle with respect to the local horizontal plane. Specifically, the angle Θ between two vectors **a** and **b** satisfies

$$\boldsymbol{a} \cdot \boldsymbol{b} = \|\boldsymbol{a}\| \, \|\boldsymbol{b}\| \cos(\Theta) \tag{2.3}$$

So that

$$\Theta = \arccos \frac{\boldsymbol{a} \cdot \boldsymbol{b}}{\|\boldsymbol{a}\| \, \|\boldsymbol{b}\|} \tag{2.4}$$

Only satellites with elevation angle above a prescribed threshold (e.g. 5°) are considered visible and included in the attenuation calculation.

Once visibility is established, the slant path below the rain height is determined. Using the local rain height h_R, evaluated according to ITU-R P.839 [10] and the ground-station altitude h_s, the length of the path segment crossing the rain region is

$$L_s = \frac{h_R - h_s}{\sin \theta} \tag{2.5}$$

where θ is the elevation angle of the link. The corresponding ground projection is

$$L_G = L_s \cos\, \theta \tag{2.6}$$

The direction of the ground-projected path is determined by the azimuth of the link: the simulator first considers a segment of length L_G aligned with the North direction and then rotates it clockwise by the azimuth angle ψ, obtaining the final ground-projection endpoint (x_f, y_f). If the ground station has coordinates (x_0, y_0), the segment $(x_0, y_0) \rightarrow (x_f, y_f)$ uniquely defines the intersection of the link with the rain field on the ground plane.

Given the ground projection of the slant path, the next step is to identify the pixels of the rain map that are crossed by the link. The simulator adopts a local Cartesian reference frame tangent to the Earth at the site, with one axis East-oriented and the other North-oriented. In this frame, the rain map can be interpreted as a regular grid with 1 km spacing. The segment connecting (x_0, y_0) and (x_f, y_f) is intersected with the grid lines of the map by first defining the Cartesian equation of the straight line joining the two points. The intersections of this line with the vertical and horizontal grid lines,

spaced at 1 km intervals, are then identified, and the midpoints between consecutive intersection points are subsequently evaluated. These midpoints uniquely lie within the pixels crossed by the ground-projected path and lie inside the pixels that are actually crossed by the slant path. Their coordinates are used to identify the corresponding cells of the rain-rate matrix. In this way, the set of crossed pixels is defined unambiguously.

An auxiliary matrix of the same dimensions as the rain map is created with all the elements initially set to zero. For each crossed pixel i, the simulator stores in the corresponding element the length Δx_i of the segment of the ground-projected path that lies inside that pixel. The described procedure in sketched in *Figure 2.4* and in *Figure 2.5.* This "distance matrix" will later be used to weigh the specific attenuation contribution of each pixel.
The sum of all segment lengths satisfies:

$$\sum_{i=1}^{N} \Delta x_i = L_G \tag{2.7}$$

where N is the number of crossed pixels.

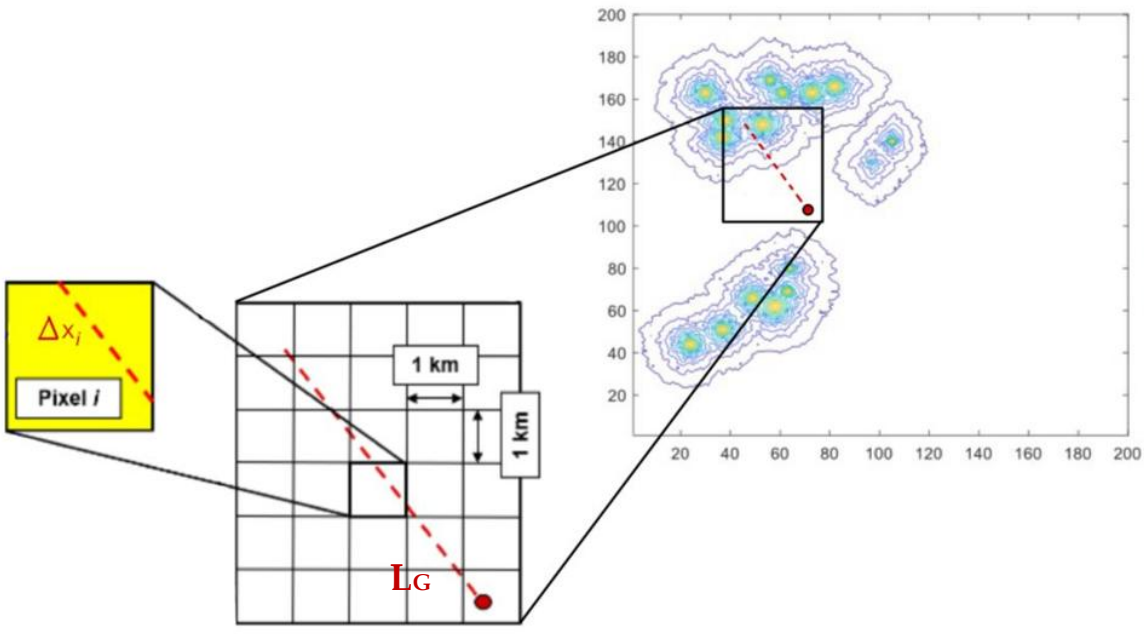

Figure 2.4: Calculation of rain attenuation using ST MultiEXCELL rain maps [30].

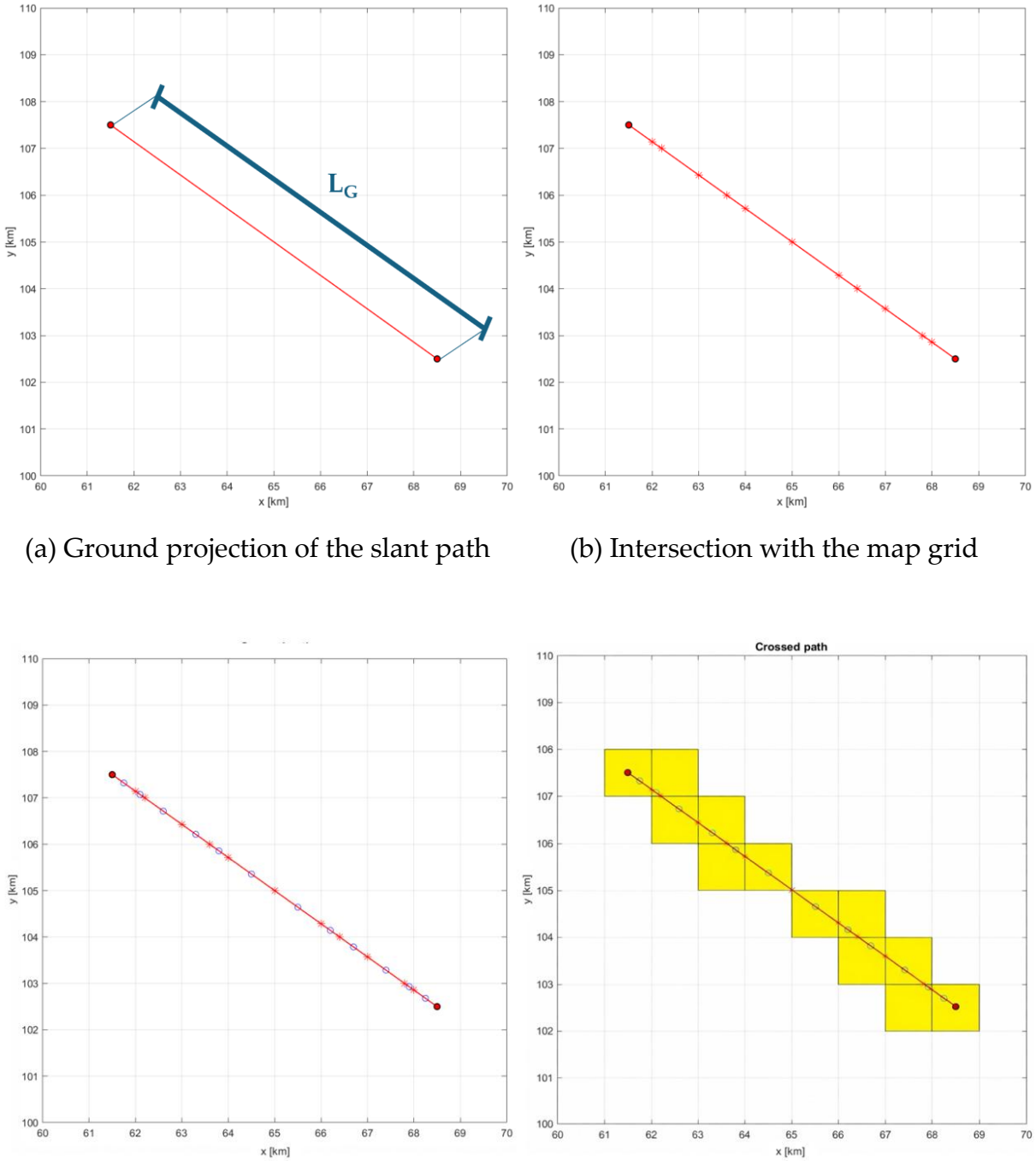

(a) Ground projection of the slant path

(b) Intersection with the map grid

(c) Medium points between intersections

(d) Pixels crossed by the link

Figure 2.5: Procedure to identify the pixels crossed by the link [22].

2.2.1. Specific attenuation and total path attenuation

The specific attenuation γ_R in each pixel is obtained from the local rain rate using the ITU-R power-law relationship defined in (1.9).

In practice, the rain map is represented by a two-dimensional grid of 200 × 200 pixels, each associated with a rain rate expressed in mm/h. For a considered link, the simulator first evaluates the matrices of coefficients k and α using a dedicated implementation of ITU-R P.838 [9]. These coefficients are assumed to be constant over the rain map for the given link and time instant. The rain rate matrix is then transformed into a specific-attenuation matrix by applying the power-law relationship elementwise, so that each pixel (i, j) is associated with a specific attenuation value $\gamma_{R,ij}$ expressed in dB/km. Once the spatial distribution of specific attenuation has been obtained, the total rain attenuation along the Earth–space link is evaluated by integrating γ_R along the portion of the slant path that lies within the rain region. As discussed in *Section 1.2*, this integration can be conveniently performed by projecting the slant path onto the ground plane. Denoting by L_s the slant-path length below the rain height, by L_G its ground projection and by θ the elevation angle, the continuous formulation given by equations (1.12a–b) remains valid.

In the numerical implementation, however, γ_R is not available as a continuous function of position, but only as discrete values associated with the pixels crossed by the ground-projected path. The path integral is therefore approximated by a discrete summation over the N pixels intersected by the link projection:

$$A_s \approx \frac{1}{\cos\theta} \sum_{i=1}^{N} \gamma_{R,i} \; \Delta x_i, \tag{2.8}$$

where $\gamma_{R,i}$ is the specific attenuation in pixel i (in dB/km) and Δx_i is the length, expressed in kilometers, of the portion of the ground-projected path lying inside that pixel.

Operationally, this summation is implemented by combining two matrices with the same spatial resolution as the rain map: a specific-attenuation matrix containing the values $\gamma_{R,i}$ and a distance matrix containing the corresponding path-length contributions Δx_i. Their element-wise product yields a matrix in which only the pixels intersected by the link contain non-zero values equal to $\gamma_{R,i}\Delta x_i$. The total attenuation for the considered link and time instant is finally obtained by summing all matrix elements and scaling the result by $1/\cos\theta$, thus accounting for the slant-path geometry.

2.2.2. Power-Budget computation

In its original formulation, the simulator was equipped with a power budget module designed to analyse the interference between a GSO satellite and a co-frequency NGSO constellation. For each time instant, once the set of NGSO satellites in view and classified as "interfering" with the GSO link had been identified, the corresponding 200 km × 200 km rain map was used to evaluate the rain attenuation on all relevant links. The procedure for attenuation computation previously described was applied first to the GSO–Earth link and then to each interfering NGSO–Earth link, considering the fixed Earth station at the center of the rain map yielding the rain attenuation A_{rain} for every path.

Within this framework, guaranteeing continuity, the power budget was evaluated consistently for each ground station s. For the GSO link, the received power at site s is computed as:

$$P_{RX,GSO,s}\,[dBW] = EIRP_{GSO} + G_{RX} - FSL_{GSO,s} - A_{rain,GSO,s} \tag{2.9}$$

where EIRP_{GSO} $[dBW]$ is the transmit EIRP of the GSO satellite, G_{RX} $[dB]$ is the receive gain of the ground-station antenna, $\text{FSL}_{\text{GSO},s}$ $[dB]$ is the free-space loss for the GSO–site $s$link, and $A_{\text{rain,GSO},s}$ $[dB]$ is the corresponding rain attenuation obtained from the procedure described in the previous section.

NGSO satellites are typically characterised in terms of power flux density (PFD) at the Earth's surface. For a given ground station s, the received power from an NGSO satellite is evaluated as:

$$P_{RX,NGSO,s}\,[dBW] = PFD + A_{eff,s} - A_{rain,NGSO,s} \tag{2.10}$$

where PFD $\left[dB\,\frac{W}{m^2}\right]$ is the power flux density radiated by the NGSO satellite, $A_{\text{eff},s}$ $[dB\,m^2]$ is the effective area of the receive antenna at site s and $A_{\text{rain,NGSO},s}$ $[dB]$ is the rain attenuation on the NGSO–Earth link, computed according to the procedure described in the previous sections.

The effective area is related to the receive antenna gain G_{RX} through

$$A_{eff,s} = \frac{G_{RX}\lambda^2}{4\pi}, \tag{2.11}$$

with λ the wavelength of the carrier.

In the present work, the power-budget expressions are retained mainly to preserve consistency with the original simulator framework; however, the analysis focuses on relative attenuation statistics and diversity gains rather than absolute received power levels.

2.3. Extension of the simulator

A key novelty of the simulator and a central aspect of the thesis, is the deployment of multiple ground stations within the rain map, arranged according to predefined geometries and inter-site separations. For each ground station, the procedure described in the previous sections is applied: at every time instant, and for every visible satellite, the corresponding slant path is projected onto the rain field, the crossed pixels are identified and the rain attenuation is computed. In this way, the simulator simultaneously generates consistent attenuation time series for all ground stations and all satellites, enabling a detailed analysis of SD, OD and their joint use in NGSO constellations.

To ensure numerical consistency and physical coherence when multiple ground stations are considered, additional care is required in handling cases where the ground-projected slant path extends beyond the finite spatial domain of the rain map. Since ground stations can be placed at different distances from the centre of the rain map, some links may partially exit the simulated rain field. For this reason, it is necessary to guarantee that each ground–satellite link either remains entirely within the map or, if it extends outside the domain, that only the portion of the slant-path projection contained inside the rain map is considered in the attenuation calculation. Operationally, once the ground station position C and the endpoint P of the ground-projected slant path have been determined, the simulator first checks whether P lies inside the domain defined by the map limits $[x_{\min}, x_{\max}] \times [y_{\min}, y_{\max}]$. If this condition is not satisfied, the semi-infinite segment starting from C and oriented toward P is intersected with the four edges of the map. Among all intersection points that lying on the perimeter, the one closest to C is selected and used as a "clipped" endpoint P_{clip}. The integration of specific attenuation is then performed exclusively along the portion of the path contained within the 200 km × 200 km map domain and no attempt is made to access pixels outside the rain field.

This assumption is fully coherent with the conceptual basis of the ST-MultiEXCELL model, in which rain is generated as a collection of localized cells whose spatial extent is limited and whose probability of occurrence smoothly decreases toward the edges of the map. As a result, rain cells are unlikely to intersect the map boundaries, and the

regions outside the simulated domain can be reasonably regarded as rain-free. This modelling choice avoids artificial edge effects and ensures that attenuation estimates are not biased by extrapolating rain statistics beyond the region where the rain field is explicitly defined. By adopting this clipping strategy, the simulator guarantees that attenuation is always computed using physically meaningful rain-rate informations, while maintaining numerical robustness and consistency across all ground stations, satellite geometries and diversity configurations. This is particularly important for SD analyses, where differences in attenuation between spatially separated sites must be attributed solely to the spatial variability of the rain field, and not to artefacts introduced by the finite extent of the simulation domain.

2.3.1. Multi-site ground-station configuration and satellite visibility constraint

To control the spatial configuration of the ground segment within the rain map, the simulator includes a dedicated geometry module that generates the positions of the Earth stations around a reference site. The user specifies the geodetic coordinates (latitude, longitude, altitude) of the reference centre around which the geometry is built, the number of stations to be deployed, a characteristic distance S (in km) and the desired pattern, chosen among a set of simple but representative geometries: a linear arrangement, an equilateral triangle and a square. In the line configuration, one station is placed at the reference position and the others are distributed along a straight line at distance S; in the triangular and square configurations, the stations are located at the vertices of an equilateral triangle or of a square with side length S. In all cases, a global rotation angle can be applied to the pattern, allowing the same geometry to be oriented arbitrarily with respect to the rain field. In *Figure 2.6* it is possible to see the main configurations used in the simulations.

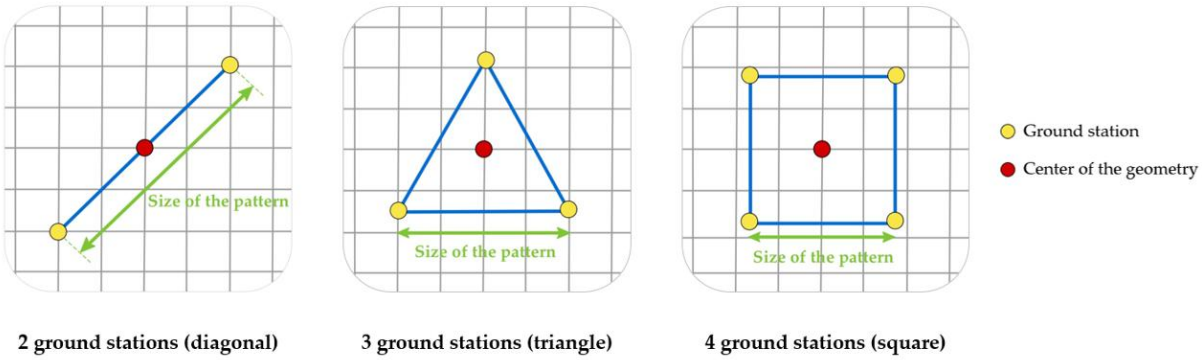

Figure 2.6: Ground station configurations.

Operationally, the reference ground station is associated with given geodetic coordinates, which define the origin of a local ENU frame. The geometry module first computes the ENU offsets (in km) of each site with respect to this reference, according to the selected pattern and spacing, and then converts the resulting positions back to geodetic and ECEF coordinates using the WGS-84 ellipsoid. At the same time, each site is mapped onto the rain field by assigning pixel coordinates under the assumption of 1 km spatial resolution (1 pixel = 1 km x 1 km). As a result, for every configuration, the simulator has direct access to both the physical coordinates of the sites (useful for link geometry and elevation-angle calculations) and their corresponding pixel indices on the 200×200 grid, essential for identifying which rain cells are crossed by each link. In *Figure 2.7* is shown a representative positioning of the ground stations within the rain map.

This flexible parametrisation of the ground-station geometry makes it possible to systematically study the impact of inter-site distance, relative orientation and number of stations on the performance of SD, OD and their combination, while the pixel-level representation of each site within the rain map is a key ingredient for the subsequent statistical analysis.

In addition, once a given geometry for the ground stations has been defined, the simulator enforces that, at each time instant, every site has access to the same number of visible satellites. This constraint is not merely a modelling convenience, but a requirement for obtaining fair and interpretable diversity results. In fact, the performance of SD, OD and joint diversity schemes depends both on the spatial correlation of rain attenuation and on the diversity order, i.e. the number of alternative links available at any given time. If one ground station could select among a larger set of satellites than another, the resulting diversity gain would be artificially enhanced, mixing the effect of a richer orbital visibility with that of the spatial separation between sites. By forcing an equal number of candidate satellites per station (for example, by restricting the analysis to the subset of satellites simultaneously visible from all sites), the simulator isolates the impact of rain-field correlation and geometry, in line with the classical diversity literature, where performance comparisons between SD and OD are carried out assuming comparable diversity orders and identical propagation conditions for the alternative branches. This modelling choice is therefore essential to ensure that the subsequent comparison between single-site, pure SD, pure OD and joint schemes truly reflects the underlying propagation characteristics, rather than trivial differences in satellite availability.

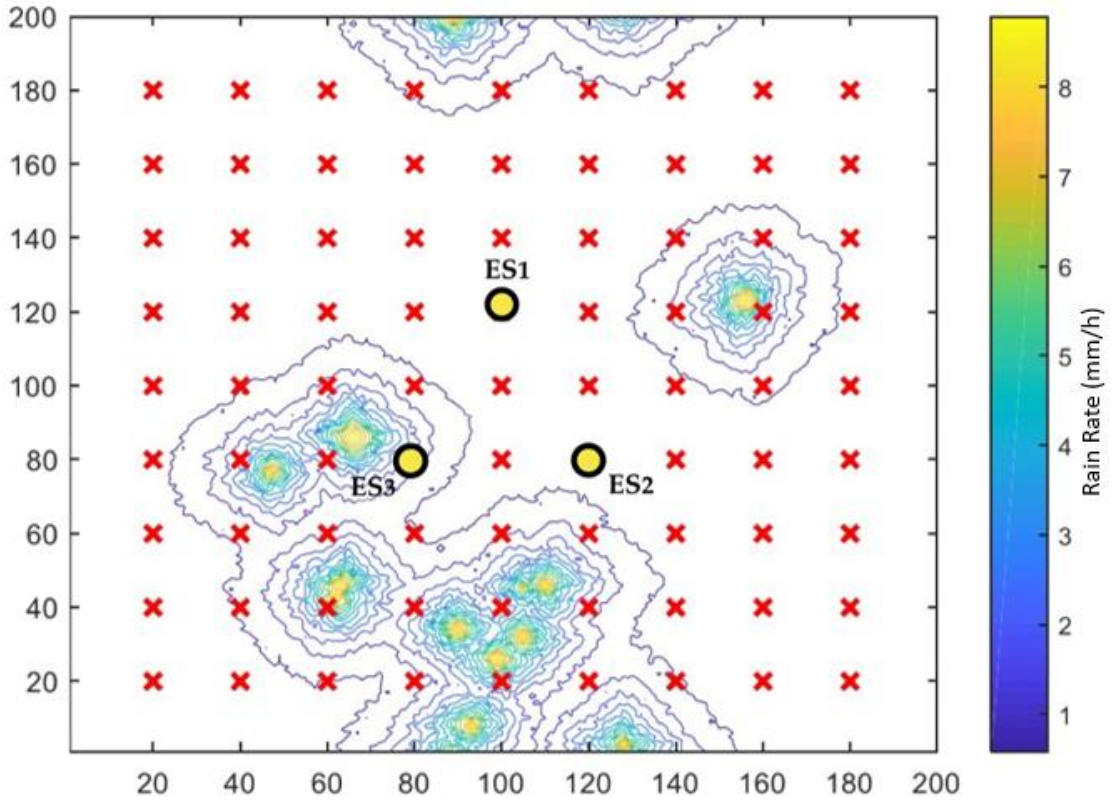

Figure 2.7: Sample ST-MultiEXCELL rain map and chosen positions: example of triangular geometry.

2.3.2. Orbital propagation module

In addition to the rain-attenuation simulator, an independent orbital-propagation module has been developed with the aim of enabling future extensions of the simulation framework. This module is conceived as a standalone tool and it is not directly involved in the numerical simulations presented in this thesis, which are based on the NGSO constellation data provided by SES and described in *Section 2.2*. Instead, its purpose is to provide a flexible and fully controllable environment for generating, propagating and analyzing satellite orbits, with particular emphasis on the resulting link-geometry parameters, and to support possible future extensions of the simulator toward fully synthetic or hybrid constellations.

The objective of this module is twofold. First, it allows the generation of synthetic satellite orbits through custom Two-Line Element (TLE) files with prescribed orbital characteristics. Second, it enables a detailed analysis of the temporal evolution of azimuth and elevation angles as observed from a fixed ground station, providing insight into the geometric behaviour of LEO satellite passes and into the statistical properties of the resulting visibility conditions.

The orbital information handled by the module is expressed in the standard TLE format. TLEs are widely used in satellite tracking and space situational awareness and represent a compact, standardized way of encoding the mean orbital elements of an Earth-orbiting object at a given reference epoch. Despite their simplicity, TLEs contain all the information required to reconstruct and propagate a satellite orbit using simplified dynamical models. TLE sets are produced by the North American Aerospace Defense Command (NORAD). NORAD keeps track of nearly all objects in orbit, both spacecraft and debris alike. The data is shared with the public through the efforts of Dr. T. S. Kelso who operates CelesTrak.com where all recent NORAD TLE data is available. To date, more than 40,000 artificial objects have been tracked in orbit at one time or another, where each is given a unique Space Catalogue Number (SCN). Some notable objects are the International Space Station (25544), the Apollo 11 Lunar Module (04041), the first human space flight of Yuri Gagarin (00103), and Sputnik 1 (00002). SCN 00001 was Sputnik 1's R7 rocket booster, the first piece of space debris.

A TLE consists of two fixed-format ASCII lines, each 69 characters long, where each column position has a predefined meaning. The first character of each line identifies the line number, ensuring correct parsing and interpretation [31].

Line 1 primarily contains identification data, epoch information and parameters related to the time evolution of the orbit. The epoch plays a central role, as it establishes the temporal reference for orbit propagation: it is expressed as a two-digit year and a fractional day of year, which defines the reference time at which all orbital elements are valid.

Line 2 contains the Keplerian mean elements that define the geometry of the orbit:

- the inclination i (in degrees), defining the tilt of the orbital plane with respect to the Earth's equatorial plane;
- the right ascension of the ascending node (RAAN) (in degrees), specifying the orientation of the orbital plane in inertial space;
- the eccentricity e, defining the orbit shape;
- the argument of perigee (in degrees), specifying the orientation of the ellipse within the orbital plane;
- the mean anomaly at epoch (in degrees), indicating the satellite position along the orbit at the epoch;
- the mean motion (in revolutions per day), which is directly related to the orbital period and semi-major axis.

In this work, custom TLE files are generated programmatically, allowing full control over these parameters. This approach makes it possible to define representative LEO orbits with prescribed altitude, inclination and phasing. When multiple satellites are generated, the mean anomaly can be evenly spaced, enabling the emulation of satellites distributed along the same orbital plane. In particular, the TLE file under study was created such that the satellite orbit is characterised by an inclination of 50° and the right ascension of the ascending node is set to 100°; the orbit is assumed to be nearly circular, with an eccentricity of 0.0005, which is typical of operational LEO communication satellites and ensures that the satellite altitude remains approximately constant along the orbit. The mean motion is fixed to 15 revolutions per day, corresponding to an orbital period of approximately 96 minutes. This value implies a semi-major axis consistent with a satellite altitude in the range of 550–600 km, which is representative of modern LEO constellations designed for broadband communication services.

Starting from the orbital elements extracted from the TLE, the satellite state vector is computed at the epoch by solving Kepler's equation and converting the Keplerian elements into Cartesian position and velocity vectors. Orbit propagation is then performed under a two-body gravitational assumption, in which the Earth is treated as a point mass, while perturbative effects such as atmospheric drag, Earth oblateness and third-body influences are neglected. Although simplified, this approach is sufficient for analyzing orbital geometry and link-angle evolution over the considered time scales.

The satellite position and velocity are propagated with a fixed temporal resolution of 60 seconds over a one-year interval, providing a dense time series of orbital states. The propagated trajectory is initially expressed in the ECI reference frame; the resulting trajectory exhibits the periodic motion characteristic of LEO satellites and can be visualized through projections onto the principal coordinate planes.

To analyze the satellite visibility from a given Earth station, the ECI coordinates are converted to the ECEF frame by accounting for the Earth's rotation. Subsequently, the satellite position is expressed in a local ENU reference frame centered at the ground station. This transformation enables a direct geometric interpretation of the satellite–ground link and allows the computation of the key angular parameters of interest.

From the ENU coordinates, the azimuth and elevation angles are computed as function of time. The elevation angle is defined as the angle between the local horizontal plane at the ground station and the line of sight to the satellite, while the azimuth angle represents the clockwise rotation from the North direction to the ground projection of the link. A minimum elevation threshold of 5° is applied to identify visible satellite positions, in line with typical assumptions used in satellite communication studies.

The propagation procedure yields continuous time series of azimuth and elevation angles for each satellite pass over the ground station. The temporal evolution of these angles is shown in *Figure 2.8*, where the first passage of the satellite seen from the ground station is represented. The temporal evolution exhibits the characteristic behaviour of LEO satellite visibility, with the elevation angle increasing from the horizon to a maximum value at closest approach and then decreasing symmetrically as the satellite sets. The azimuth angle varies smoothly during the pass, reflecting the ground track of the satellite relative to the station location. Together, these two parameters provide a complete geometric description of the satellite pass and of the orientation of the Earth–space link over time.

By collecting all visible satellite positions over the simulated period, empirical probability density functions (PDFs) of the azimuth and elevation angles are obtained and reported in *Figure 2.9*. The elevation-angle PDF is strongly skewed toward low values, with the highest probability occurring just above the minimum visibility threshold (5°). This behaviour is a direct consequence of the orbital geometry and of uniform time sampling. For a nearly circular LEO orbit at approximately constant altitude (about 550 km), the satellite spends a significant fraction of each visible pass at moderate and low elevation angles, while it traverses the region of maximum elevation only for a short time near closest approach. As a result, high elevation angles are intrinsically less frequent in time-based statistics.

The azimuth-angle PDF is clearly non-uniform and exhibits two dominant peaks (at roughly 70° and 290°). This bimodal structure reflects the fact that visible passes occur along preferred azimuth directions associated with the ascending and descending portions of the orbit, leading to two clusters of azimuth values corresponding to satellite acquisition and loss of signal. The exact location and the sharpness of these peaks depend on the orientation of the orbital plane and on the ground-station latitude. Such non-uniform azimuth distributions are typical for single-satellite analyses. Overall, the obtained angular distributions confirm that LEO links spend a large fraction of their visibility time at low elevation angles and along recurrent azimuth directions, aspects that have direct implications for atmospheric attenuation statistics and fade mitigation analyses.

The orbital-propagation module is a useful complementary tool and together with core rain-attenuation simulator, the overall framework preserves modularity and extensibility, allowing future integration of synthetic constellations or hybrid datasets without altering the existing simulation architecture.

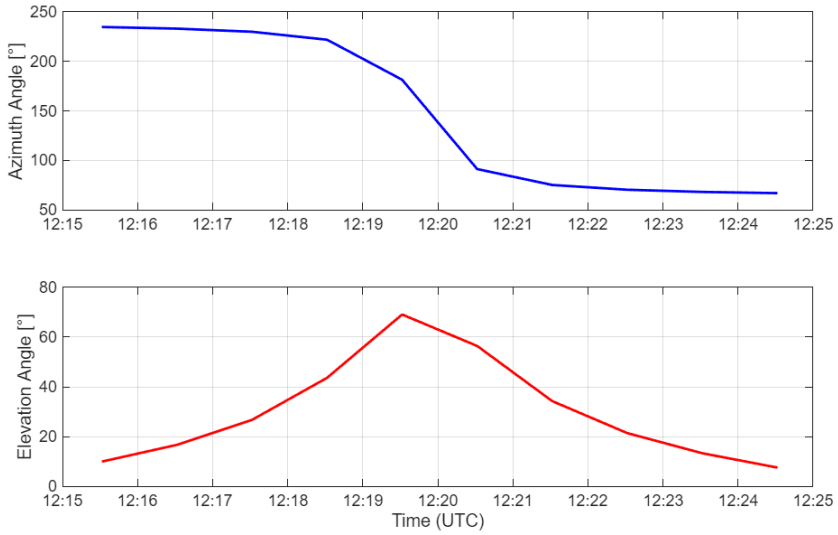

Figure 2.8: Temporal evolution of the azimuth and elevation angles for the satellite first passage above the ground station.

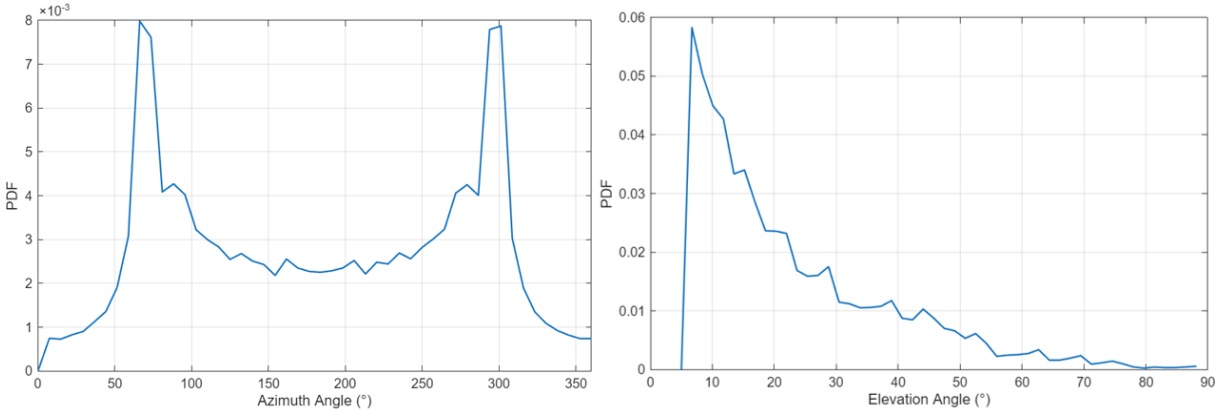

(a) (b)

Figure 2.9: PDFs of the azimuth angle (a) and elevation angle (b).

2.4. Time-series generation and data organization

The simulator described in the previous sections produces a set of time series describing the temporal evolution of rain attenuation and link geometry for multiple Earth–space links. These time series constitute the fundamental data structure used in the post-processing phase where minimum-attenuation selection, diversity combining strategies and CCDF estimation are applied to quantify the performance gains achievable through orbital, site and joint diversity schemes.

For a given simulation scenario the simulator generates a collection of timetables, one for each ground station included in the configuration. For instance, if k is the number of ground stations in the geometry, the output is stored in a kx1 cells, where each cell contains the timetable associated with the k-th ground station.

In the considered simulation, as indicated in *Figure 2.10*, each timetable has dimensions 524,140 × 2. The rows represent the uniformly sampled time epochs over the simulated period, while the columns store, respectively, the rain attenuation values affecting the NGSO Earth–space links visible from the considered ground station and the corresponding elevation angles of those links.

The rain attenuation values A_{NGSO} (in dB) result from the complete attenuation calculation procedure described in the previous sections, including rain-field intersection, specific-attenuation evaluation and path integration. The elevation angle θ (in degrees) is defined as the angle between the local horizontal plane at the ground station and the line of sight connecting the station to the satellite.

Both entries are stored as arrays of size $N \times 1$, where N is the number of NGSO satellites simultaneously visible from the ground stations at the considered time instant. So, for a considered time step, the number of visible satellites N is identical for all ground stations in the geometry. Moreover, N depends on the fact that only satellites with elevation angle greater than or equal to 5° are included.

To reduce data dimensionality and focus on the quantities strictly required for FMTs analysis, the timetables used represent a "slimmed" version of the full simulator output. Additional parameters that can be available include:

- ψ, the azimuth angle (in degrees), defined as the clockwise rotation applied to a North-oriented reference line to align it with the ground projection of the satellite link;
- $P_{RX,NGSO}$, the received power at the Earth station from the NGSO path, computed through the link-budget formulation;

- R, the local rain rate (in mm/h) at the pixel of the map corresponding to the ground station position;
- a binary clear-sky indicator, assuming value 1 during rain-free conditions and 0 otherwise, for a required pixel on the map.

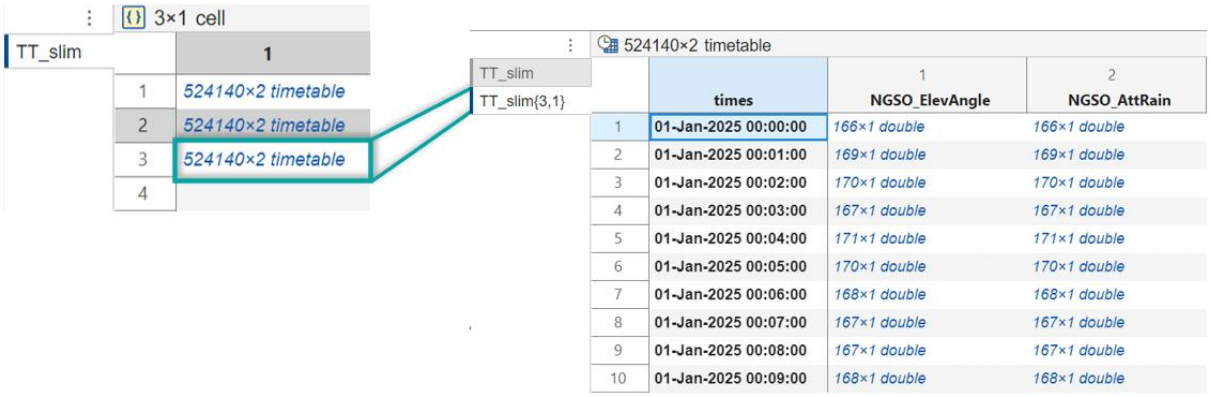

Figure 2.10: View of the simulator output structure (case with three ground stations).

3 Performance Analysis and Results

3.1. Scenarios and parameters

The simulator described in *Chapter 2* enables the analysis of different scenarios in which an NGSO satellite constellation communicates with one or multiple ground stations. For long enough simulated time periods, it is possible to collect a significant amount of data on the physical quantities of interest. In this work, the focus is on the long-term statistics of rain attenuation affecting extremely-high-frequency (EHF) NGSO Earth–space links and on quantifying the benefits achievable through diversity-based FMTs. For this reason, particular attention is given to key geometric and propagation parameters, such as the link elevation and azimuth angles, as well as the local rain-rate values extracted at specific positions within the rain map. The performance assessment is carried out by post-processing the attenuation and link-geometry time series generated by the simulator. The analysis mainly relies on attenuation Complementary Cumulative Distribution Functions (CCDFs) and on the diversity gain obtained through Site Diversity (SD), Orbital Diversity (OD) and their joint application.

This chapter presents the results obtained for a set of representative simulation scenarios and investigates how the combined use of different ground-station configurations and diversity techniques improves NGSO link performance. Moreover, along with the results, the chapter addresses a method to implement a statistical model for Orbital Diversity based on the long-term statistics of rain attenuation and on the three-dimensional angular separation between alternative NGSO Earth–space links.

3.1.1. Space segment

The NGSO constellation of interest is the SpaceX VLEO sub-constellation, whose orbital data were provided by SES S.A., as mentioned in *Section 2.2*. Specifically, the analysed scenario is a space-to-Earth communication downlink in which the NGSO satellites operate at 40 GHz. The NGSO constellation includes 7,518 satellites, almost uniformly distributed along the orbits at altitude 345.6 km, 340.8 km and 335.9 km. For completeness, in addition to the constellation's parameters reported in *Table 2.1* and

Table 2.2, the SpaceX satellites are assumed to implement an Equivalent Isotropic Radiated Power (EIRP) density adjustment as a function of the steer angle, defined as the angle formed between the boresight and the user beam. This feature is introduced to maintain approximately constant Power Flux Density (PFD) over the ground surface covered by the satellite. The values for both the EIRP density and the PFD are indicated in *Table 3.1*. Finally, the signals coming from the NGSO system are assumed to be circularly polarised.

Table 3.1: Table describing EIRP and PFD values for VLEO sub-constellation. Source: Table A.7-2 [29].

	at slant	at nadir
EIRP density [dBW/Hz]	-39.79	-44.20
EIRP in 1MHz [dBW/MHz]	20.21	15.80
Distance to Earth [km]	558.42	335.90
Spreading loss [dB]	-125.93	-121.52
PFD in 1MHz [dB(W/m^2/1MHz]	-105.72	-105.72

3.1.2. Ground Stations

Ground-station deployment is defined according to the specific FMT under study. For Orbital Diversity analysis the computation of CCDFs exploits the use of a single ground station positioned at the centre of one of the four quadrants of the 200 km x 200 km rain map. The arrangement of the ground station was made by moving the reference ground station located at the centre of the map along the two diagonals at a distance of 70 km from the centre of the squared map. The reference ground station was characterized by the following coordinates:

- *latitude*: 45.4°
- *longitude*: 9.5°
- *altitude*: 0.084 km

Each configuration is considered separately and obtained by dedicated simulation. The setting outlined in *Figure 3.1*. shows the chosen positions on the map, representing together the four points only for simplicity. The considered ground receive antenna is manufactured by ©*CPI Vertex Antennentechnik GmbH*; *Table 3.2* enlists its specifications. The main parameter of interest for the present study is the maximum receive gain, equal to G_{RX} = 59.6 dBi for the considered frequency of 40 GHz of the simulated

scenario. The receiver bandwidth is set to 1 MHz, consistently with Resolution 770 [32] for a receiving gateway.

For Site Diversity studies, the three ground-station geometries (diagonal, triangle and square) are used, as described in *Section 2.3.1* and illustrated in *Figure 2.6*. The MATLAB routine implementing the geometry placement allows to exploit each region of the rain map, specifying as input parameter the pixel coordinates of the geometry reference centre. This approach enables systematic comparisons across simulation scenarios and supports the generalization of the obtained results.

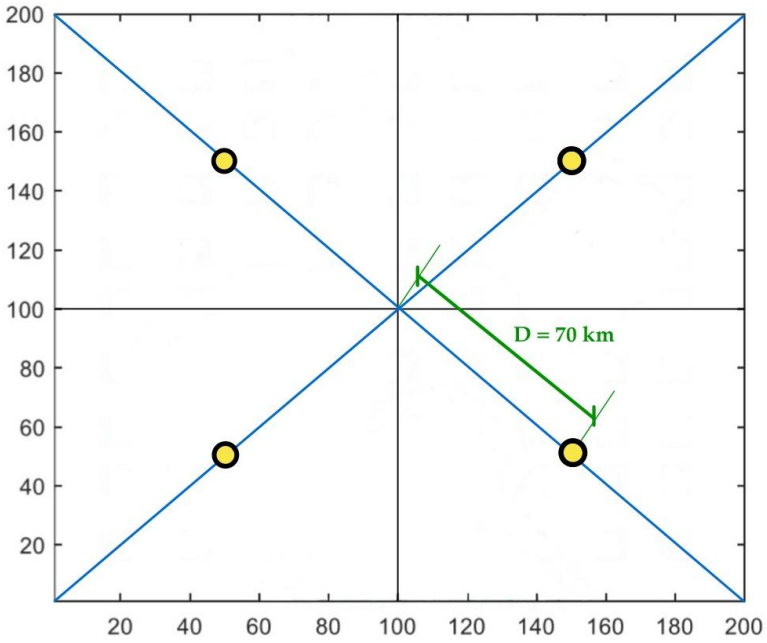

Figure 3.1: Ground-station chosen positions for OD analysis.

Table 3.2: Specifications of ©*CPI Vertex Antennentechnik GmbH.*

Freq. Pol.	Tx	47,85 – 48,15 GHz
	Rx	37,85 – 38,15 GHz
	Beacon	39,4 GHz, 45deg
Sidelobes	ITU 732, ITU-R S580	
Feed	2 port feed linear polarised	
G/T	@38GHz, elev. 20°, LNA 230 K	33,8 dB/K
Gain	@48/38GHz	61,18 dBi/ 59,08 dBi
Pattern BW	-3dB @38GHz -3dB @48GHz	0,17° 0,14°
Power	< 50W operation, 250W (max)	

For all SD configurations, the involved ground stations are treated as equivalent nodes, and a master–slave architecture is not assumed. The SD decision rule follows a selection-combining approach, selecting at each epoch the site associated with the lowest attenuation. Examples of ground-station layouts used for SD analysis are shown in *Figure 3.2* with a view of the chosen geometry on the map and the specifications for each ground sites.

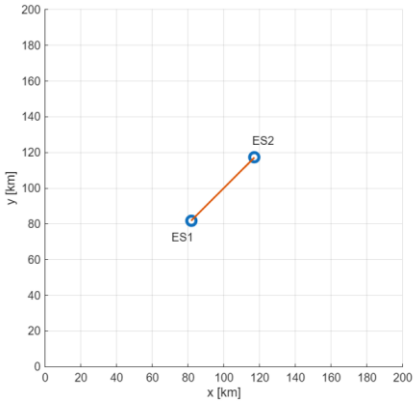

	Geodetic Coordinates (latitude, longitude, altitude)	Pixel Coordinates (x, y)
ES1	(45.241°, 9.275°, 0.133 km)	(81.822, 81.822)
ES2	(45.559°, 9.726°, 0.133 km)	(117.178, 117.178)

(a) Diagonal geometry, site separation S = 50 km

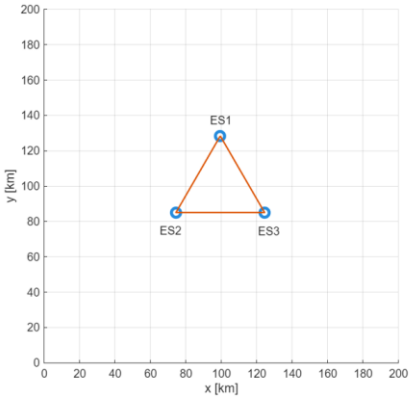

	Geodetic Coordinates (latitude, longitude, altitude)	Pixel Coordinates (x, y)
ES1	(45.659°, 9.5°, 0.149 km)	(99.5, 128.368)
ES2	(45.269°, 9.181°, 0.149 km)	(74.5, 85.066)
ES3	(45.269°, 9.819°, 0.149 km)	(124.5, 85.066)

(b) Triangular geometry, site separation S = 50 km

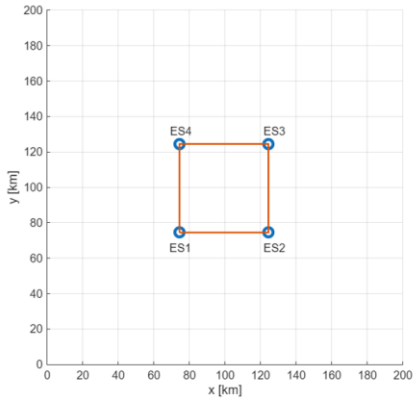

	Geodetic Coordinates (latitude, longitude, altitude)	Pixel Coordinates (x, y)
ES1	(45.175°, 9.182° ,0.182 km)	(74.5, 74.5)
ES2	(45.175°, 9.818° ,0.182 km)	(124.5, 74.5)
ES3	(45.625°, 9.821°, 0.149 km)	(124.5, 124.5)
ES4	(45.625°, 9.179°, 0.149 km)	(74.5, 124.5)

(c) Square geometry, site separation S = 50 km

Figure 3.2: Examples of ground-station configurations for SD analysis.

3.2. Orbital Diversity performance analysis

The key principle behind OD is to leverage on path diversity in multi-visibility NGSO constellations by selecting, at each time instant, the least impaired link between those in view from a single receiving site. OD has been discussed as an attractive countermeasure when deploying multiple geographically separated gateways is impractical due to Earth-segment costs and operational complexity, and when diversity can instead be achieved by allocating a "common resource on demand" across multiple spacecraft and/or transponders. It should be noted, however, that in GSO scenarios the benefit is frequently modest because the angular separation between feasible alternative paths is usually small, leading to high fade correlation. In NGSO systems, instead, multi-visibility conditions and rapidly varying geometries can provide substantially larger angular diversity and, consequently, higher potential gains.

At a given location, each visible satellite defines a distinct Earth–space propagation path with its own line-of-sight geometry (elevation and azimuth) and, consequently, a different interaction with the local precipitation field. Because rain is spatially inhomogeneous and organized in cells with limited horizontal extent, rain attenuation affecting different slant paths is only partially correlated. Even though all OD branches originate from the same ground station, the slant paths diverge as altitude increases: their ground-projected trajectories progressively separate, so different links may intersect different rain cells or cross the same storm with different effective path lengths and intensity profiles. Therefore, it becomes increasingly likely that, among multiple available links, at least one exhibits a significantly lower attenuation than the others. For OD analysis, the simulator generates, for each gateway placement, a time series sampled every $\Delta t = 60$ s. At each epoch t_n, the output contains the set of simultaneously visible satellite links, represented as a vector of rain attenuation values $\{A_i(t_n)\}$ and the corresponding vector of elevation angles $\{\theta_i(t_n)\}$. Since each attenuation value is computed along the actual Earth–space path defined by the instantaneous satellite geometry, the time variability and statistical distribution of the elevation angle are inherently embedded in the simulated dataset.

OD is modelled through selection combining performed independently at each epoch. The gateway is assumed to remain continuously active and to route traffic through the least impaired satellite path among the available candidates. This represents an idealised upper-bound condition, since it neglects any switching latency, signalling overhead, or operational constraints associated with handover between satellites. Accordingly, the OD-effective attenuation series is defined as

$$A_{\mathrm{OD}}(t_n) = \min_{i \in \mathcal{S}(t_n)} A_i(t_n), \tag{3.1}$$

$$\theta_{\mathrm{OD}}(t_n) = \theta_{i^\star}(t_n), \tag{3.2}$$

where $\mathcal{S}(t_n)$ is the set of satellites visible at epoch t_n and $i^\star$ is the index achieving the minimum attenuation. This step converts the original vector-per-epoch output into a scalar time series, where each epoch contributes a single attenuation value corresponding to the link selected by OD.

To quantify how OD performance scales with the number of available alternatives, the selection is repeated for different candidate-set sizes N_{vis}. At each epoch, a uniform subsampling of the visible-satellite set is applied to retain exactly N_{vis} candidate links, and the minimum attenuation is selected within that subset. For small N_{vis}, the gateway has limited freedom: it may be forced to use a link that happens to intersect a strongly attenuating rain cell. As N_{vis} increases, the gateway can choose among more distinct link geometries. Because rain attenuation along these links is only partially correlated, the probability that all candidate links are simultaneously severely faded decreases, and the OD-selected attenuation $A_{\mathrm{OD}}(t)$ is more frequently close to clear-sky conditions.

Long-term attenuation statistics are then obtained by computing empirical CCDFs from the resulting scalar time series. For a given threshold a, the empirical CCDF for the j-th gateway placement is estimated as the fraction of time samples for which the OD-selected attenuation exceeds a:

$$\widehat{P}_j(A_{\mathrm{OD}} > a) = \frac{1}{T} \sum_{n=1}^{T} \mathbf{1}\{ A_{OD}^{j}(t_n) > a\}, \quad j \in \{1,2,3,4\} \tag{3.3}$$

where T is the number of epochs and $\mathbf{1}\{\cdot\}$ denotes the indicator function, equal to 1 if the condition inside the braces is satisfied and 0 otherwise.

To reduce sensitivity to the specific positioning of the ground station within the finite 200 km × 200 km rain map, OD results are computed for four separate simulations, corresponding to four gateway placements located at the centres of the four map quadrants (see *Figure 3.1*). Each placement is treated as equally likely. The final OD CCDF is obtained by averaging the exceedance probabilities pointwise:

$$\bar{P}(A_{OD} > a) = \frac{1}{4} \sum_{j=1}^{4} \widehat{P}_j(A_{OD} > a). \tag{3.4}$$

This equal-weight averaging is justified because all four realizations are generated over the same simulated time span and with the same sampling period; therefore, they contain the same number of time epochs and, after OD selection, the same number of

OD-effective samples. Hence, the resulting mean CCDF can be interpreted as the average performance over equiprobable map placements. This strategy provides a more robust characterization of OD performance under the same climatic statistics and constellation dynamics, while mitigating potential artefacts related to map boundaries or local features of a single rain-field realization.

Figure 3.3 reports the empirical CCDFs of the OD-selected rain attenuation A_{OD} at 40 GHz for different candidate-set sizes N_{vis}. Each curve represents the exceedance probability $\bar{P}(A_{\mathrm{OD}} > a)$ obtained by applying OD selection at each epoch and then averaging across the four gateway placements. Differences among curves are attributable to the OD selection order N_{vis} only. A clear and monotonic trend is observed: increasing N_{vis} systematically reduces the exceedance probability for any fixed attenuation threshold a. This is the behaviour expected from selection combining: when the candidate set is enlarged, the corresponding minimum attenuation value cannot increase and can only remain unchanged or decrease. Consequently, for any threshold a, the event $\{A_{\mathrm{OD}} > a\}$ becomes less frequent as N_{vis} grows, leading to lower time percentages of exceedance across the entire attenuation range. $N_{\mathrm{vis}} = 1$ is the single-link case (no benefit from diversity), while the case "Full set of visible satellites" provides the maximum OD order available at each epoch. In the considered scenario, this corresponds on average to about 170 simultaneously visible satellites per epoch, and it yields the lowest curve, thus representing the most favourable OD condition under the imposed visibility constraints.

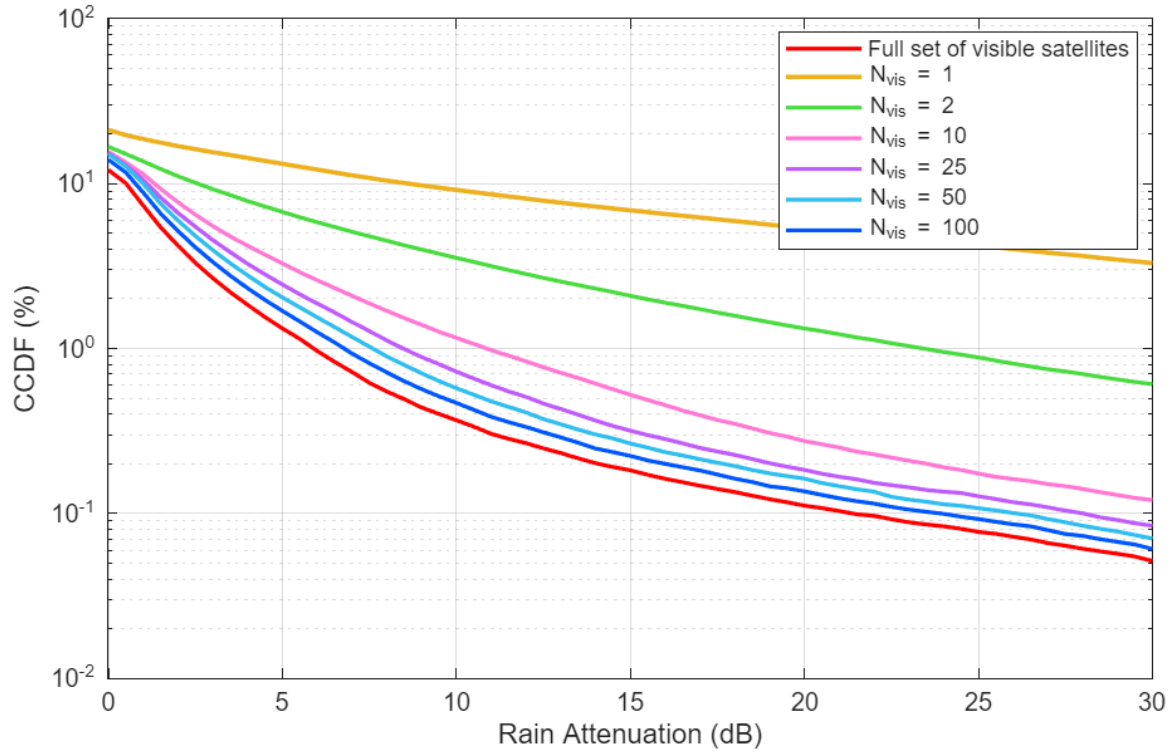

Figure 3.3: Orbital Diversity CCDFs for different candidate-set sizes N_{vis}.

The performance advantage provided by OD is quantitatively highlighted by comparing attenuation levels exceeded for a given fraction of time. Defining $A(p)$ as the attenuation exceeded for p% of the time (inverse CCDF), the single-link case yields $A_{N=1}(10\%) \approx 8.61$ dB, whereas OD over the full visible set yields $A_{\text{Full set}}(10\%) \approx 0.79$ dB. This corresponds to an OD diversity gain of:

$$G_{\text{OD}}(p) = A_{N=1}(p) - A_{\text{Full set}}(p), \tag{3.5}$$

equal to $G_{\text{OD}}(10\%) \approx 7.8$ dB. From an operational standpoint, OD also translates into a significant reduction in outage probability: for an outage threshold of $A_{OD} = 30$ dB, the exceedance probability decreases from $\bar{P}(A_{OD} > 30\,\text{dB}) \approx 3.29\%$ in the single-link case to $\bar{P}(A_{OD} > 30\,\text{dB}) \approx 0.052\%$ when selecting over the full visible set, i.e., an outage reduction by a factor of about 64x. The gain becomes even more pronounced at lower time percentages, which are dominated by intense and spatially localised precipitation events and the separation between curves is generally more evident in the high-attenuation tail. In these conditions, partial decorrelation across different pointing directions becomes more beneficial.

At the same time, the marginal benefit of increasing N_{vis} decreases as N_{vis} becomes large. This "diminishing returns" behaviour is evident from the progressively smaller separation between curves when moving from moderate to high values of N_{vis}. In practical terms, once the gateway already has access to many simultaneously visible satellites, adding further candidates yields a smaller incremental probability of avoiding the most attenuating rain regions, because the most favourable link is already likely to be available within the existing set. This saturation effect highlights that OD performance is ultimately bounded by the instantaneous geometric diversity offered by the constellation (distribution of satellites in elevation/azimuth) and by the spatial scales of the rain field.

3.3. Site Diversity Performance analysis

SD also exploits the spatial inhomogeneity of rainfall. In SD, multiple geographically separated gateways serve the same traffic and are connected through terrestrial backhaul so that, at each time instant, the system can route the signal through the site experiencing the most favourable propagation conditions. Compared with OD, SD provides diversity through inter-site separation rather than the angular separation between links to different satellites as observed from the same site. While OD relies on the partial decorrelation associated with different satellite pointing directions, SD mitigates fades by exploiting the limited spatial extent of intense rain cells: if a

precipitation field is affecting the area above one gateway, most or all satellite links from that site may be simultaneously degraded, reducing the effectiveness of OD, whereas a sufficiently distant gateway is unlikely to be impacted at the same time. This stronger decorrelation mechanism can therefore lead to larger diversity gains, at the cost of higher Earth-segment deployment and infrastructure requirements.

For the SD analysis, the simulator is run in a multi-site mode using predefined ground-station geometries with prescribed inter-site separations. For a given geometry with K Earth stations, the simulator outputs K synchronized timetables, one per site. At each time epoch t_n, the timetable entries contain the set of simultaneous satellite links visible from that site, represented by the vector of rain attenuation samples and the corresponding elevation angles. A key requirement for a fair SD assessment is that all sites in the geometry have the same number of candidate links at each epoch. This is enforced through the visibility constraint adopted in the simulator, as explained in *Section 2.3.1*: at any time t_n, only the subset of satellites simultaneously visible from all sites is retained. As a result, each station is associated with the same number of links $N(t_n)$.

Let $A_{s,j}(t_n)$ denote the rain attenuation on the j-th satellite link observed from site $s \in \{1, \dots, K\}$ at epoch t_n, where $j \in \{1, \dots, N(t_n)\}$ indexes the common set of links across all sites. SD is implemented through selection-combining applied to corresponding links: for each epoch and for each link index j, the site providing the lowest attenuation for that specific satellite is selected. This produces an auxiliary "master-site" timetable representing the SD-effective attenuation for each link j:

$$A_{\mathrm{SD},j}(t_n) = \min_{s\in\{1,\dots,K\}} A_{s,j}(t_n). \tag{3.6}$$

This construction preserves the same temporal indexing and the same set of satellite links as the original single-site outputs, while embedding the diversity selection across geographically separated stations.

Long-term attenuation statistics are computed as empirical CCDFs. For each original site s, a single-site CCDF is estimated from its attenuation time series, yielding $P_s(A > a)$. In parallel, the SD-effective CCDF is obtained from the master-site series, yielding $P_{\mathrm{SD}}(A > a)$. To support the interpretation of the results, the empirical SD CCDF is compared against a theoretical reference derived from the single-site CCDFs under simplified assumptions. In the idealized case of statistically identical and independent diversity branches, selection combining would yield:

$$P_{\mathrm{SD}}^{(ideal)}(A > a) = \prod_{s=1}^{K} P_s\,(A > a), \tag{3.7}$$

which, for the case with $k = 2$ ground stations reduces to $P_{\mathrm{SD}}^{(\mathrm{ideal})}(A > a) = P_1(A > a)\, P_2(A > a)$. Deviations between the simulated SD curve and this independence-based reference quantify the impact of spatial correlation of rain attenuation between sites. *Figure 3.4* illustrates the impact of SD on the long-term attenuation statistics by comparing the single-site CCDFs (ES1 and ES2) with the SD selection-combining curve for a simulation scenario with two ground stations along the SW-NE diagonal at two different site separation distances S (S = 20 km panel (a), S = 80 km panel (b)).

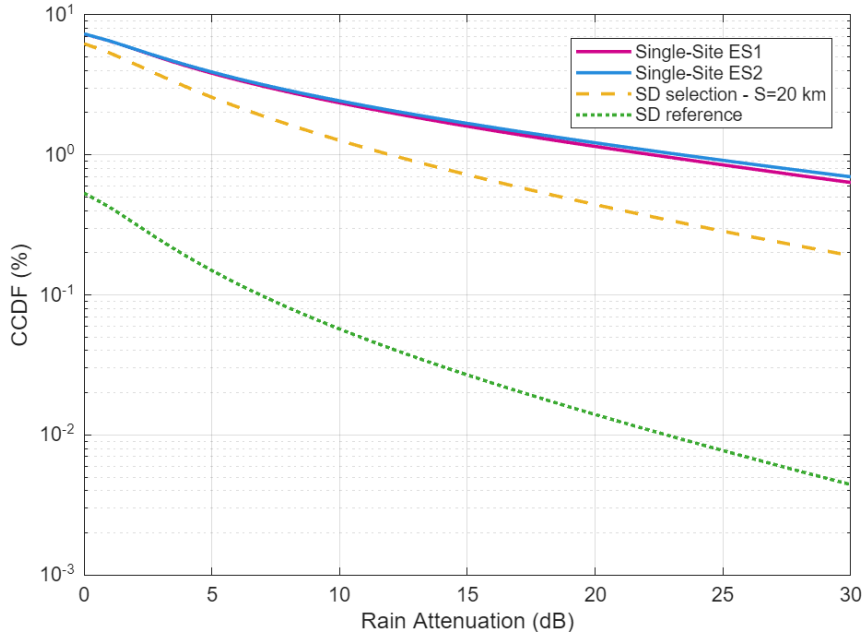

(a) Inter-site separation S = 20 km

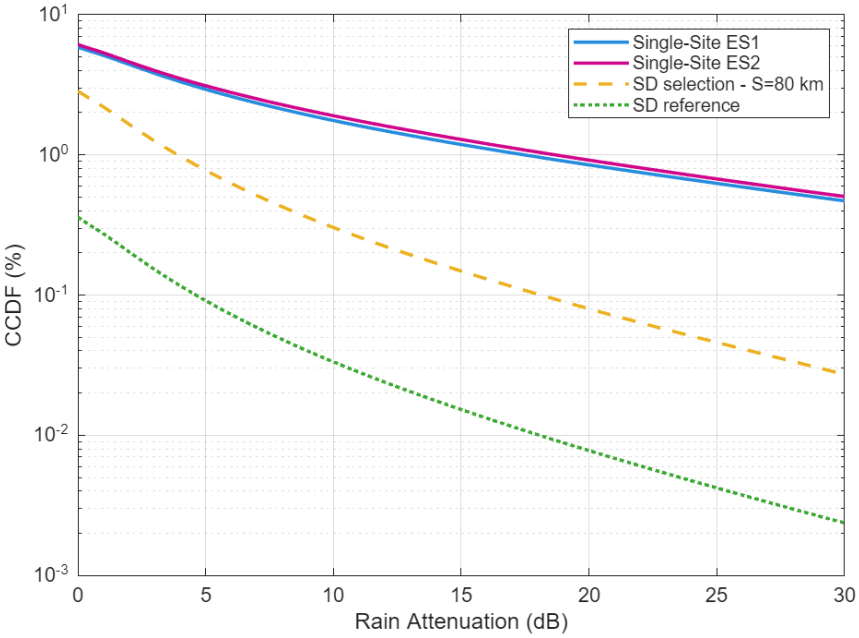

(b) Inter-site separation S = 80 km

Figure 3.4: Side Diversity CCDFs for dual-site diagonal geometry.

As expected, the two single-site curves almost overlap, confirming that the two gateways experience comparable marginal attenuation statistics and that differences in SD performance are mainly driven by the inter-site correlation. When the inter-site distance increases from 20 km to 80 km, the SD CCDF curve shifts further downward. This behaviour is consistent with the physical structure of rainfall. Importantly, the gap between the simulated SD curve and the independence reference decreases as the site separation increases, which is consistent with reduced correlation at larger distances. Hence, increasing the inter-site separation not only improves SD performance directly, but also moves the system closer to the ideal behaviour predicted under independence assumptions. The benefit becomes even more evident in the high-availability region, where deep fades dominate system margins. Using the inverse CCDF $A(p)$, the attenuation exceeded for 1% of the time decreases from $A_{20km}(1\%) \approx 12.0$ dB to $A_{80km}(1\%) \approx 3.9$ dB, corresponding to a reduction of about 8.1 dB. At 0.5% of the time the reduction increases to about 11.5 dB (18.7 dB vs 7.1 dB). For a fixed outage threshold of $A = 30$ dB the exceedance probability drops from $\hat{P}_{\text{single-site}}(A > 30\text{ dB}) \approx 0.635\%$ to $\hat{P}_{\text{SD, 20km}}(A > 30\text{ dB}) \approx 0.191\%$ and $\hat{P}_{\text{SD, 80km}}(A > 30\text{ dB}) \approx 0.0272\%$, corresponding to an outage reduction by factors of ~ 3.3 and ~ 23, respectively.

Figure 3.5 compares the long-term rain-attenuation CCDF for a single-site link with the SD selection-combining performance obtained for three multi-site geometries centered on the same map location: a dual-site diagonal configuration ($k = 2$), an equilateral triangle ($k = 3$), and a square ($k = 4$). In all cases, the inter-site spacing is fixed to $S = 50$ km, so that differences among the SD curves are primarily attributable to the diversity order (i.e., the number of available ground stations), rather than to different separations or to different placement within the rain field. All SD curves lie below the single-site CCDF over the entire attenuation range. The single-site reference is obtained by placing one Earth station at the mean position of the SD sites in the rain map, ensuring a consistent comparison with the diversity configurations. For a fixed site separation of 50 km, the SD performance improves monotonically with the number of sites employed: the diagonal configuration provides the smallest improvement, the triangular geometry yields a further downward shift, and the square configuration provides the most significant reduction of exceedance probability. Overall, *Figure 3.5* demonstrates that, once the inter-site separation is fixed, the dominant design parameter becomes the number of diversity sites. Increasing the diversity order from two to four gateways provides a substantial additional improvement in link availability, at the expense of increased Earth-segment deployment and backhaul requirements.

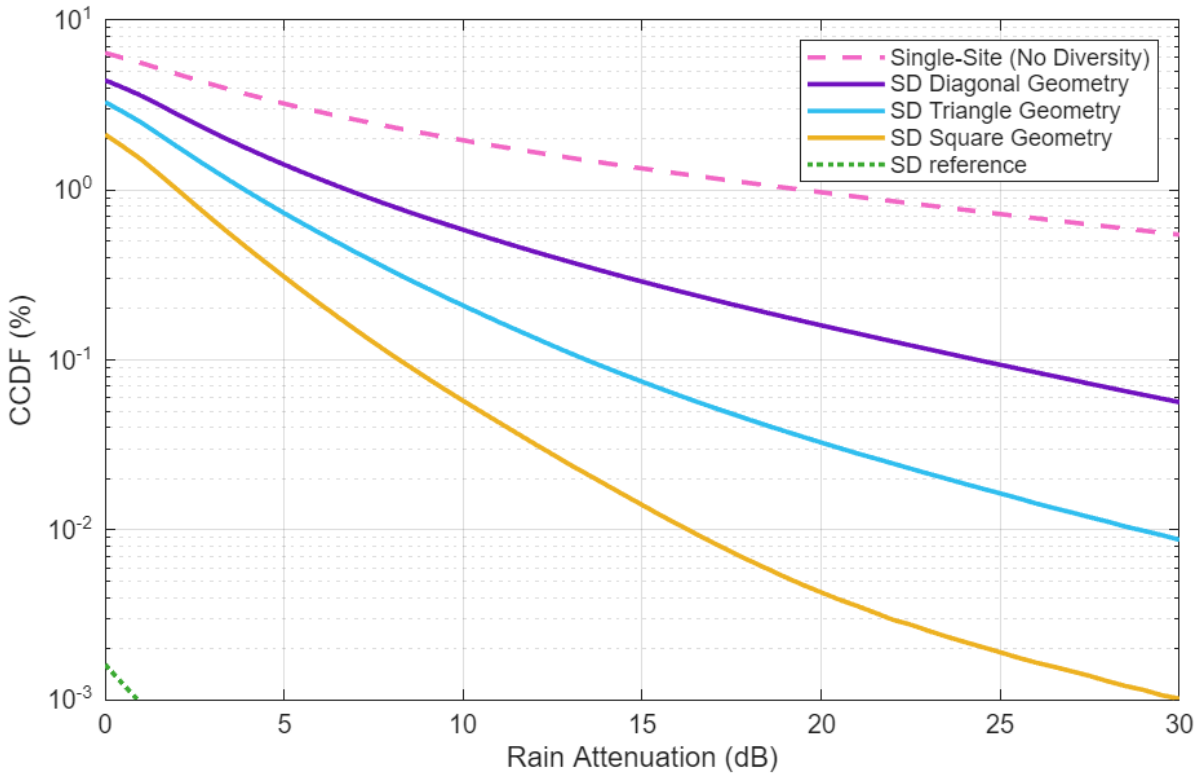

Figure 3.5: Site Diversity CCDFs for three geometry configurations with fixed site separation distance S = 50 km.

The incidence of the inter-site separation distance is shown in *Figure 3.6*. The results are obtained from a dual-site SD configuration in which two gateways are placed along the diagonal of the rain map and progressively separated by a distance *S*, starting from 10 km up to 60 km. The number of sites is kept fixed to two. The results highlight a clear and physically consistent trend: increasing *S* yields a systematic downward shift of the SD CCDF. A relevant observation is that, within the investigated range, the SD performance continues to improve noticeably, suggesting a broader effective separation range in this NGSO-driven simulation scenario. This behaviour can be contrasted with findings reported for GSO link studies based on weather-radar data [33], where the role of spatial correlation is often discussed in terms of a decorrelation distance on the order of some tens of kilometres. This statement captures the key point behind the saturation-like behaviour observed in GSO-oriented SD analyses: once attenuation processes are effectively uncorrelated, increasing the baseline further yields diminishing additional decorrelation. In the present results, instead, the improvement remains evident over a wider distance interval. This difference is consistent with the fact that the NGSO scenario involves time-varying link geometries and dynamic selection conditions, which can reduce the persistence of correlated fading compared to the essentially fixed pointing geometry typical of GSO paths.

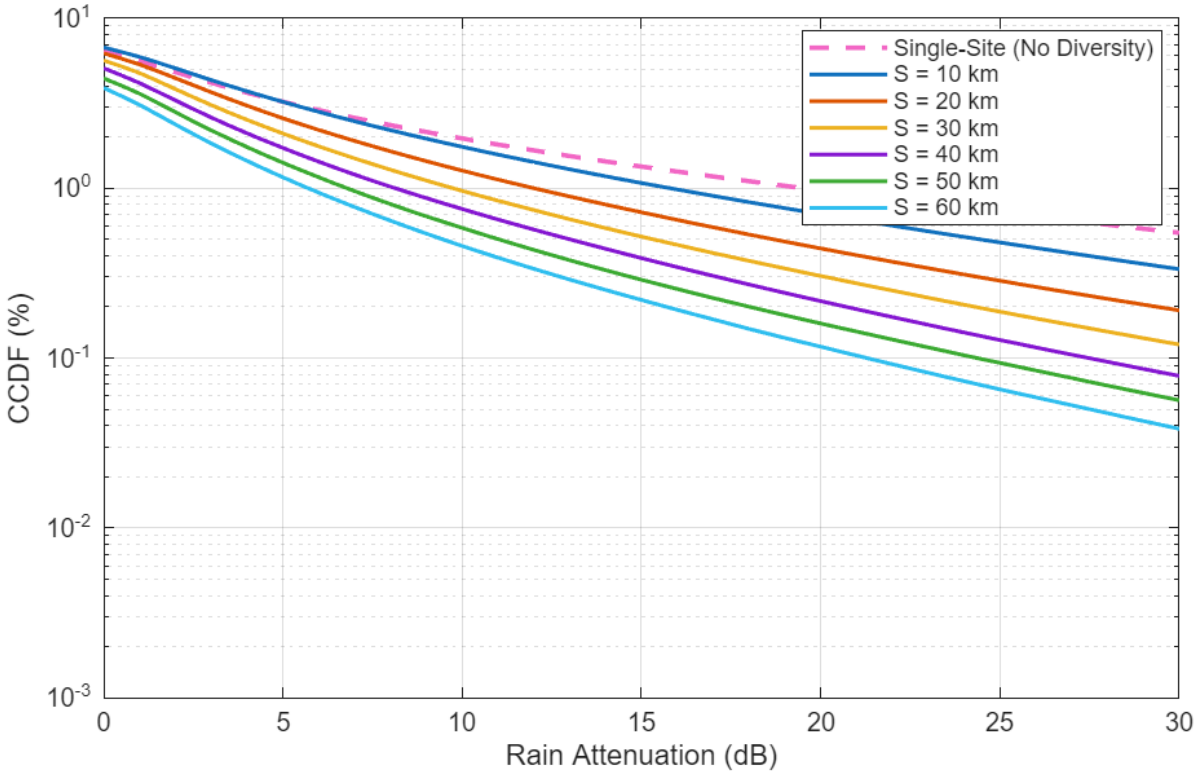

Figure 3.6: Site Diversity CCDFs for dual-site diagonal configuration at increasing inter-site distance S.

Other SD results will be shown in *Section 3.4* together with a direct comparison between scenarios in which the two FMTs previously discussed are jointly implemented to achieve additional performance gains.

3.4. Joint Site-and-Orbital Performance Analysis

After analysing OD and SD separately, this section investigates the performance achievable when the two FDTs are jointly applied. Joint SD–OD is particularly relevant for NGSO architectures where multiple gateways are deployed within the service area and, simultaneously, multiple satellites are visible from each gateway. From a propagation viewpoint, the two techniques provide diversity through complementary mechanisms, leveraging alternative paths in both the ground segment and the space segment. SD mitigates fades by exploiting the limited spatial extent of intense rain cell; OD, instead, exploits the angular separation among alternative satellite links from the same site. When combined, these mechanisms increase the overall diversity order and reduce the probability that all available alternatives are simultaneously severely faded.

For each simulated multi-site geometry, the simulator provides synchronized timetables for the involved Earth stations. The per-epoch output can be written as a vector of attenuation samples as

$$\{A_{s,j}(t_n)\}_{j=1}^{N(t_n)}, s \in \{1, \dots, K\}, \tag{3.8}$$

where s indexes the ground site and j indexes the common set of satellite links.

The joint SD–OD strategy adopted here corresponds to a two-stage selection combining procedure, consistent with the practical interpretation of "best available path" across all site–satellite alternatives.

First, SD is applied link-by-link across sites. For each epoch t_n and for each satellite link j, the attenuation minimum across the available sites is selected as reported in (3.6) and stored in the "master-site" timetable that contains, for every epoch, a vector of SD-selected attenuation values across the common satellite set. Second, OD is applied to the master-site timetable. At each epoch t_n, the system selects, among the $N(t_n)$ active satellite links, the one that yields the minimum attenuation:

$$A_{\text{joint}}(t_n) = \min_{j \in \{1,\dots,N(t_n)\}} A_{\text{SD},j}(t_n). \tag{3.9}$$

This step reduces the vector-per-epoch master-site output to a scalar time series $A_{\text{joint}}(t_n)$, representing the attenuation experienced by a system that can switch both across sites and across satellites, always choosing the least impaired path available at each time instant. Overall, this two-stage procedure is equivalent to selecting, at each epoch, the minimum attenuation across all site–satellite combinations:

$$A_{\text{joint}}(t_n) = \min_{s} \min_{j} A_{s,j}(t_n). \tag{3.10}$$

The staged implementation (SD first, then OD) is adopted for convenience and consistency with the SD and OD processing already introduced yielding the same per-epoch selected attenuation as the direct global minimum.

Long-term statistics of the joint scheme are finally obtained by computing the empirical CCDF of the selected attenuation series. For a threshold a, the exceedance probability (in time percentage) is estimated as:

$$\hat{P}(A_{\text{joint}} > a) = \frac{1}{T} \sum_{n=1}^{T} \mathbf{1}\{A_{\text{joint}}(t_n) > a\}, \tag{3.11}$$

where T is the number of epochs and $\mathbf{1}\{\cdot\}$ denotes the indicator function, equal to 1 if the condition inside the braces is satisfied and 0 otherwise.

The first analysis, shown in *Figure 3.7*, is made on the same dual-site geometry with the same set of separation distances *S*, considered in the previous section. So that the resulting curves can be directly compared with the SD-only results shown in *Figure 3.6*. A first qualitative outcome is that the joint SD–OD curves lie systematically below the SD-only curves for the same separation *S*, demonstrating that adding OD on top of SD yields a clear additional reduction of exceedance probability. This is expected because the joint scheme increases the effective diversity order. Compared to SD-only, the joint results exhibit a markedly stronger reduction in the high-attenuation tail, which is the region most relevant for high-availability design. This indicates that the additional OD stage is particularly effective at mitigating deep fades: even when both sites are affected by precipitation, the constellation typically offers multiple concurrent links with different elevation/azimuth geometries, and the selection of the least impaired path increases the probability of finding a link that avoids the most intense rain structures or traverses them with a shorter effective path.

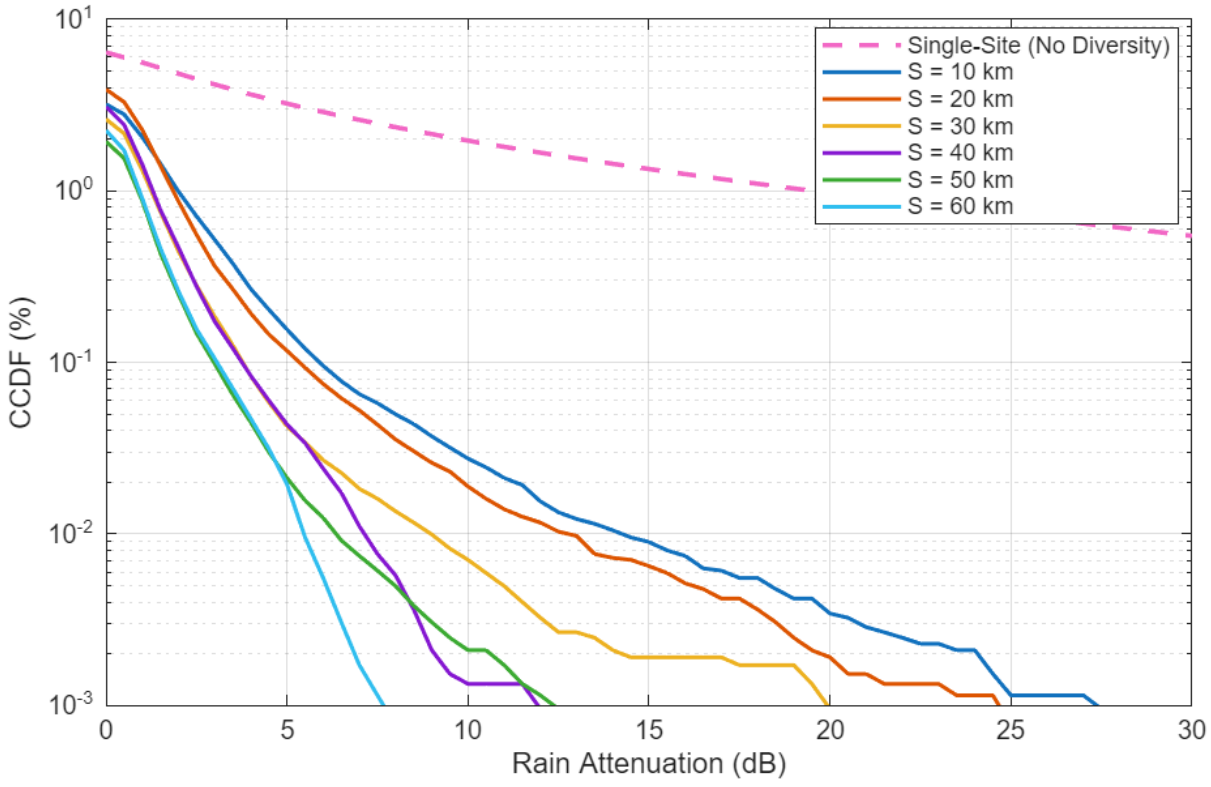

Figure 3.7: SD+OD CCDFs for dual-site diagonal configuration at increasing inter-site distance S.

In the final analysis, the objective is to highlight the substantial benefits achieved by exploiting both the diversity order (i.e., the number of ground stations) and the deployment geometry, (i.e., inter-site separation). The same simulation scenario is considered for SD-only and SD+OD analyses. The three ground-station configurations - diagonal ($k = 2$), triangle ($k = 3$) and square ($k = 4$) - are centered on the same rain-map region and two different inter-site separation distances are examined, $S = 30\ km$ and $S = 50\ km$. The attenuation CCDFs obtained with SD selection combining, *Figure 3.8* (a), can be easily compared with the CCDFs computed when SD and OD are together applied (*Figure 3.8* (b)). The previously discussed trends are confirmed. Quantitative examples illustrating this advantage are provided for the square geometry.

For SD-only, the exceedance probability at 2 dB is:

- $P(A > 2\ dB) \approx 2.19\%$ for S = 30 km,
- $P(A > 2\ dB) \approx 1.01\%$ for S = 50 km.

For joint SD+OD, it decreases to

- $P(A > 2\ dB) \approx 0.0651\%$ for S = 30 km,
- $P(A > 2\ dB) \approx 0.0015\%$ for S = 50 km.

Therefore SD+OD reduces the exceedance probability by a factor of about 34x with respect to SD-only at S = 30 km and by about 670x with respect to SD-only at S = 50 km. For higher attenuation thresholds, the joint SD+OD exceedance probability drops to the order of $10^{-4}\%$,rapidly approaching the statistical resolution limit of the dataset.

Compared with SD-only, the joint results also indicate that the dependence on inter-site separation becomes less dominant once OD is added. In *Figure 3.8* (a), the gap between the solid line (S = 30 km) and dashed line (S = 50 km) continues to increase when moving from the diagonal to the triangle and square geometry. In *Figure 3.8* (b), instead, this separation remains approximately constant across the different geometries. This behaviour is expected: OD already provides substantial diversity through the availability of multiple satellite paths at each epoch, so the incremental benefit of increasing S from 30 km to 50 km can become smaller, particularly for higher-order geometries (triangle/square) where the ground segment already offers strong spatial diversity.

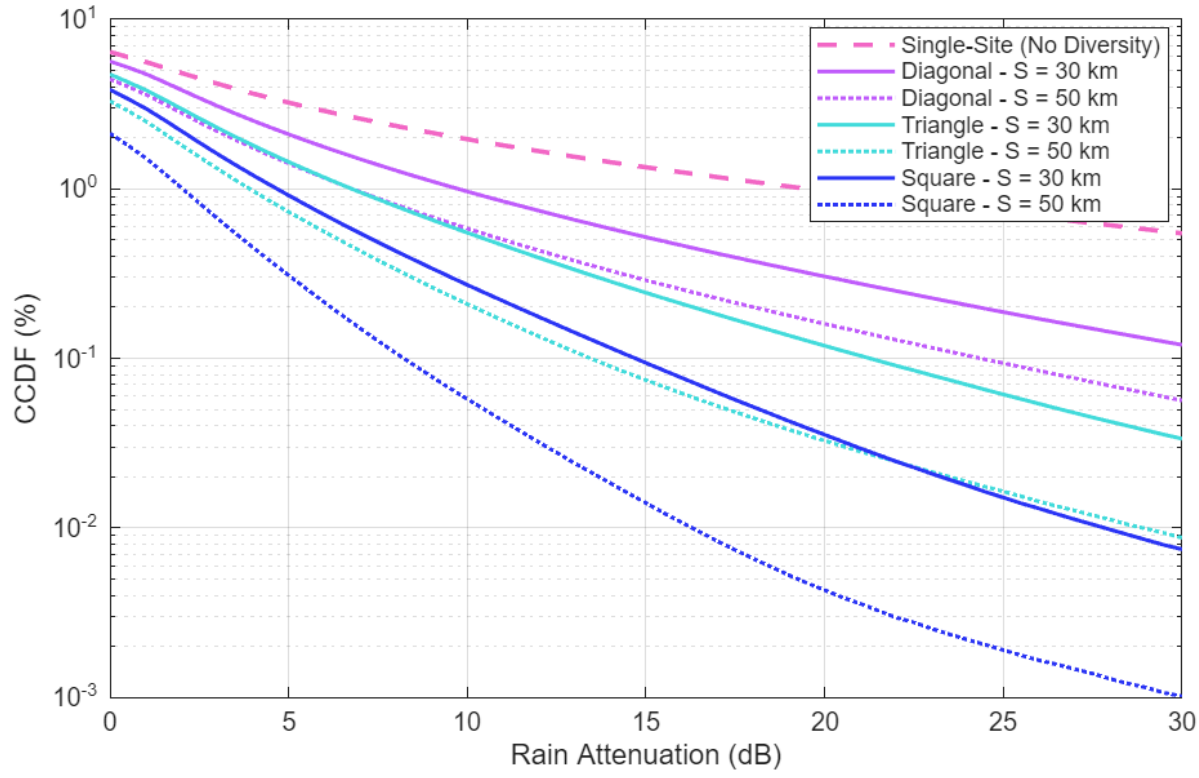

(a)

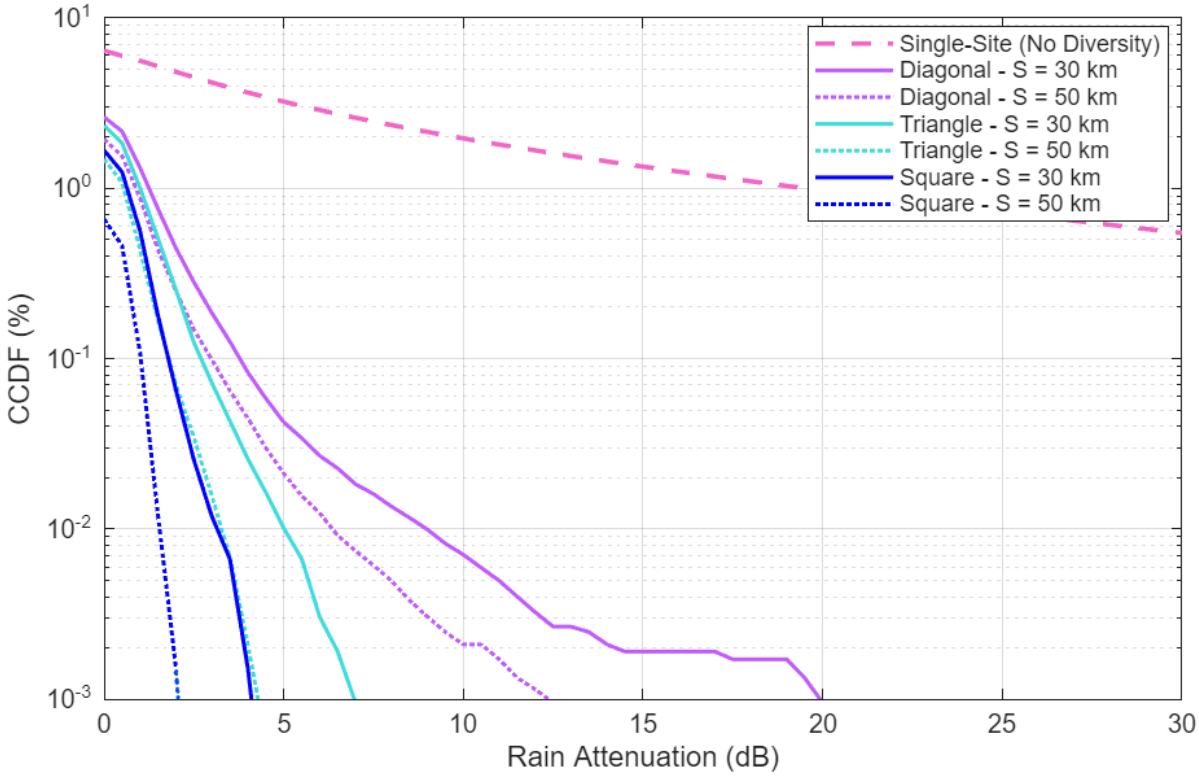

(b)

Figure 3.8: CCDFs for three geometry configurations with S = 30 km and S = 50 km. (a) SD-only scenario, (b) SD+OD scenario.

3.5. Statistical Model for Orbital Diversity

The objective of this section is to develop a statistical OD model that reproduces the long-term behaviour observed in the simulator, without requiring time-domain simulations once the model is calibrated. The modelling approach focuses on the absolute attenuation difference between pairs of simultaneously visible NGSO links and on its dependence on the angular separation between corresponding link directions. The analysis is performed on simulator outputs generated at three carrier frequencies (20, 30, and 40 GHz) to investigate possible frequency-dependent trends.

At each simulation epoch, the simulator provides a set of simultaneously visible links and their rain attenuation values. For each pair of visible links (i, j), the absolute attenuation difference is computed as

$$|\Delta A| = \left|A_i - A_j\right|, \tag{3.12}$$

and associated with the angular separation $\theta \in [0, 180°]$ between the two link directions. The resulting dataset is summarized through density plots: the colormap shows a column-wise normalized 2D density $H_{norm}(\theta, |\Delta A|)$, obtained by scaling each θ-bin column to its maximum value (maximum equal to 1), so that the relative distribution of $|\Delta A|$ can be compared across separation angles. To improve robustness and generality, the analysis was not carried out on a single rain-map placement of the gateway. Instead, five independent simulation runs were performed, each using the same scenario configuration, but a different ground-station location within the 200 km × 200 km rain map. Specifically, as visible in *Figure 3.9*, the gateway was placed at the map centre and along the two map diagonals at the centres of the four quadrants.

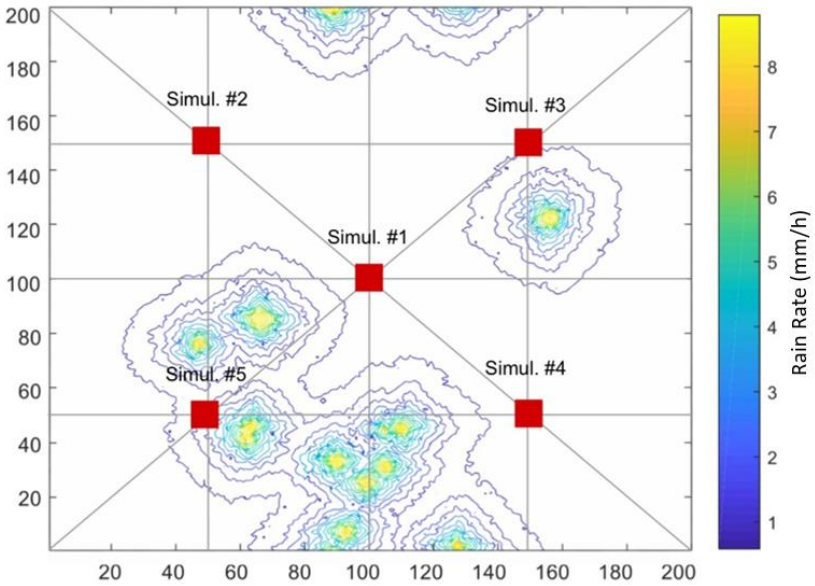

Figure 3.9: Sample of ST-MultiEXCELL rain map and chosen positions.

For each run $r \in \{1, \dots, 5\}$, $H_{r,norm}(\theta, |\Delta A|)$ was computed using the same $|\Delta A|$ binning and the same θ angular classes. The final density plot, reported in *Figure 3.10* (one for each simulation frequency) is obtained by pointwise averaging the five histograms. This averaging reduces sensitivity to the specific spatial realization of the rain field within a finite map and mitigates potential boundary artefacts. For parametric statistical characterization, the separation angle θ is discretized into 1° classes to obtain a locally stationary description.

For each class c, all the samples of $|\Delta A|$ whose separation angle falls in $[\theta_c, \theta_c + 1°)$ are pooled together and represented through an empirical histogram on a fixed $|\Delta A|$ grid (consistent with the density-map bins). Since the simulator output is already in binned form, parameter estimation is performed using frequency-weighted maximum likelihood. Several distributions were evaluated (e.g., Gamma, Burr, Weibull). The selection criterion was based also on the stability and interpretability of the fitted parameters as smooth functions of θ, and their consistency across the three frequencies. Among the tested candidates, the lognormal distribution provided the most coherent behaviour in this sense: it captures the skewed shape of $|\Delta A|$ across angles and produces parameter sequences suitable for subsequent functional modelling. Some examples are reported in *Figure 3.11*. This choice is also physically plausible, as rain attenuation depends on multiplicative propagation effects along the path (rain-rate variability, effective path length through cells, and spatial inhomogeneity), and when considering $|\Delta A|$ between two links, the resulting distribution remains strictly positive and typically right skewed.

Therefore, for each angular class c (centred at θ_c), the conditional distribution is modelled as

$$f_{|\Delta A|}(|\Delta A| \mid \theta = \theta_c) \sim \text{Lognormal}(\mu(\theta_c), \sigma(\theta_c)), \tag{3.13}$$

where $\mu(\theta)$ and $\sigma(\theta)$ are the mean and standard deviation of $\ln|\Delta A|$. Repeating the estimation for all classes yields discrete estimates $\{\mu(\theta_c)\}$ and $\{\sigma(\theta_c)\}$ for each frequency, as illustrated in *Figure 3.12*. The per-class parameter sequences are smooth but non-trivial with rapid behaviour at small angles, slow evolution at mid-angles and a tail near large separations. To enable analytic generation of the distribution at arbitrary θ, continuous parametric models are introduced.

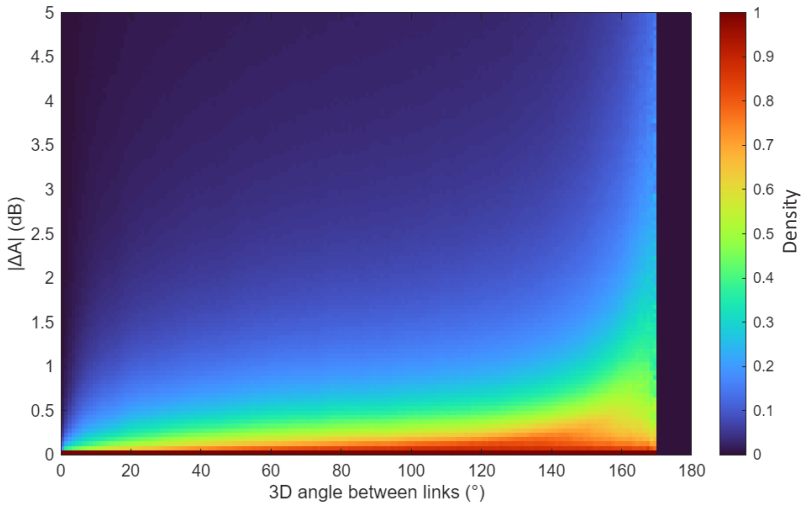

(a) $f = 20\ GHz$

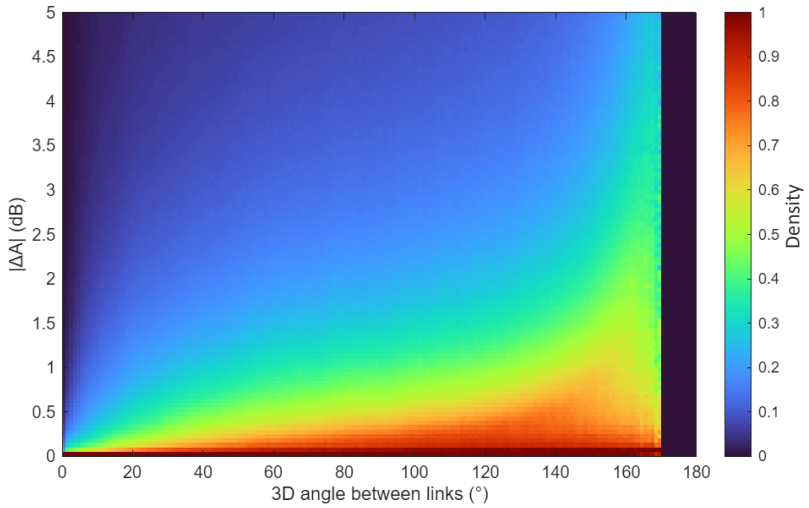

(b) $f = 30\ GHz$

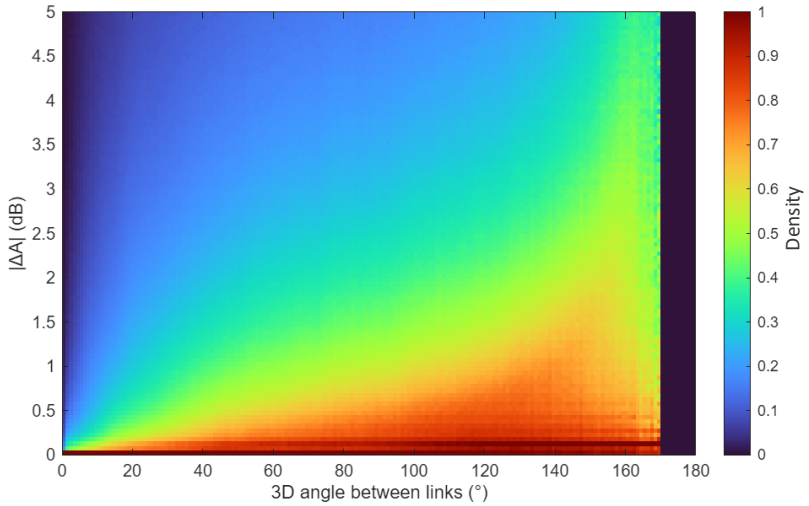

(c) $f = 40\ GHz$

Figure 3.10: Density plots $H_{norm}(\theta, |\Delta A|)$.

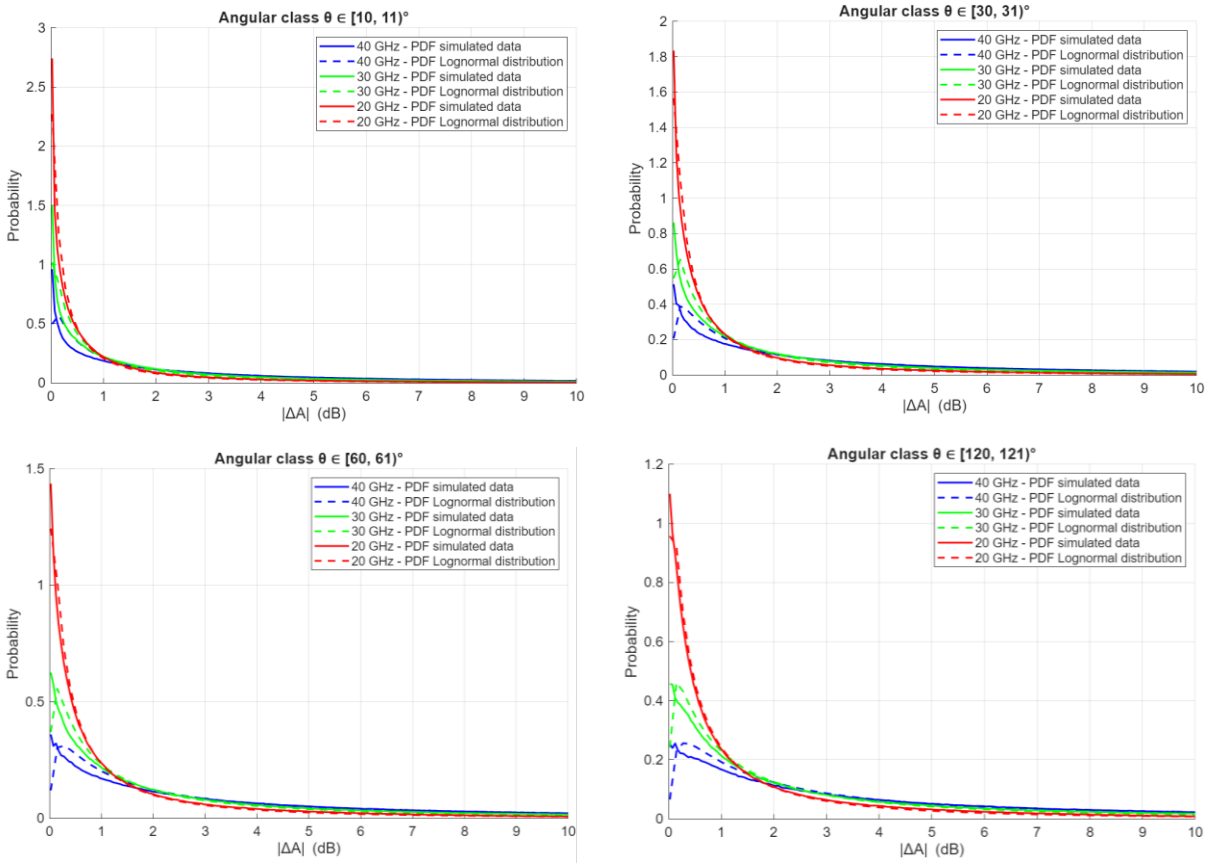

Figure 3.11: Empirical vs Lognormal PDFs for different angular classes

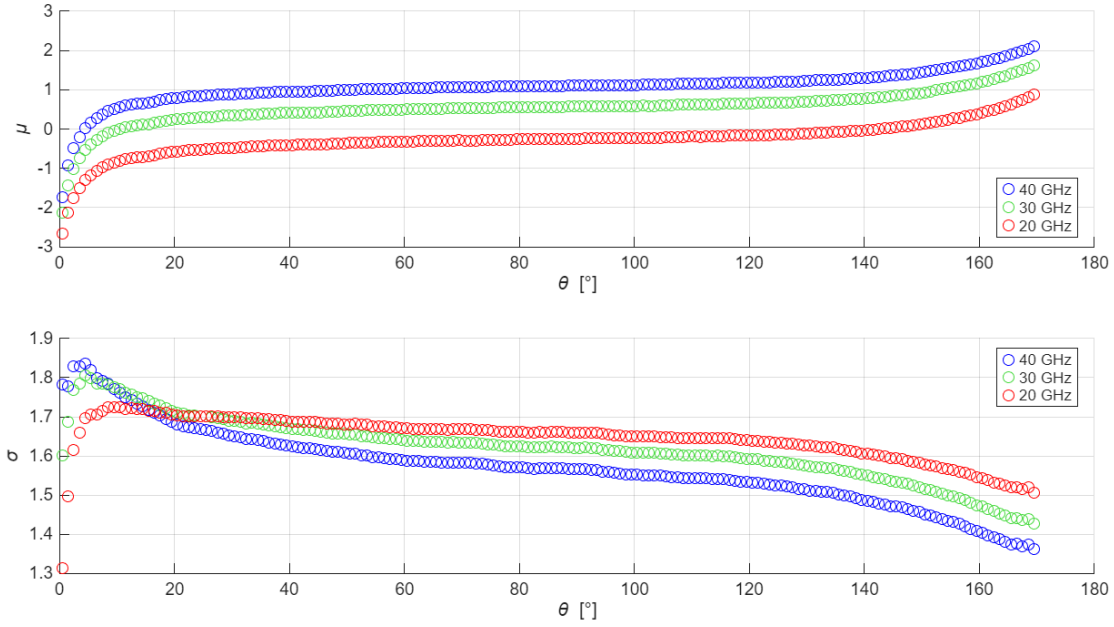

Figure 3.12: Estimates from data of Lognormal distribution parameters for 20, 30, and 40 GHz.

3.5.1. Model for $\mu(\theta)$: logarithmic + exponential tail

The selected model for $\mu(\theta)$ is:

$$\mu(\theta) = a_0 + a_1 \ln\left(\frac{\theta+\varepsilon}{180}\right) + a_2 \exp\left(\frac{\theta-180}{\tau}\right), \quad \varepsilon = 1° \tag{3.14}$$

This structure captures a slow growth driven by the ln (·) term (stable for $\theta \to 0$ thanks to ε), and a controlled "end-angle" behaviour through the exponential term centered at 180°. The fitted coefficients are reported in *Table 3.3* for $\mu(\theta)$ at the three considered frequencies.

Table 3.3: Coefficient values for $\mu(\theta)$ model.

Frequency	a_0	a_1	a_2	τ
20 GHz	0.05341	0.37	2.687	9.787
30 GHz	0.8849	0.3868	2.682	9.146
40 GHz	1.421	0.3868	2.623	8.788

A key empirical result is that the frequency dependence is mainly captured by a vertical shift, since a_1, a_2, τ are approximately invariant and the dominant change is in a_0. This is confirmed by the fact that the three curves in the first plot in *Figure 3.10* preserve the shape moving from one frequency to the other. Using 20 GHz as baseline, the other curves can be approximated by the function:

$$\mu_f(\theta) \approx s(f)\, \mu_{20}(\theta) + d(f), \tag{3.15}$$

where f is expressed in GHz and with $s(30\ GHz) \approx 1.01$ and $s(40\ GHz) \approx 0.99$, hence $s(f) \approx 1$ is assumed. The offset is then modelled as a logarithmic law with the constraint $d(20\ GHz) = 0$:

$$d(f) = \beta\ ln\left(\frac{f}{20}\right) \tag{3.16}$$

The final compact frequency-scalable model for μ, therefore is:

$$\mu(\theta, f) \approx\ \mu_{20}(\theta) + \beta\ ln\left(\frac{f}{20}\right), \quad \beta = 1.94337 \tag{3.17}$$

and the modelled functions are shown in *Figure 3.13*.

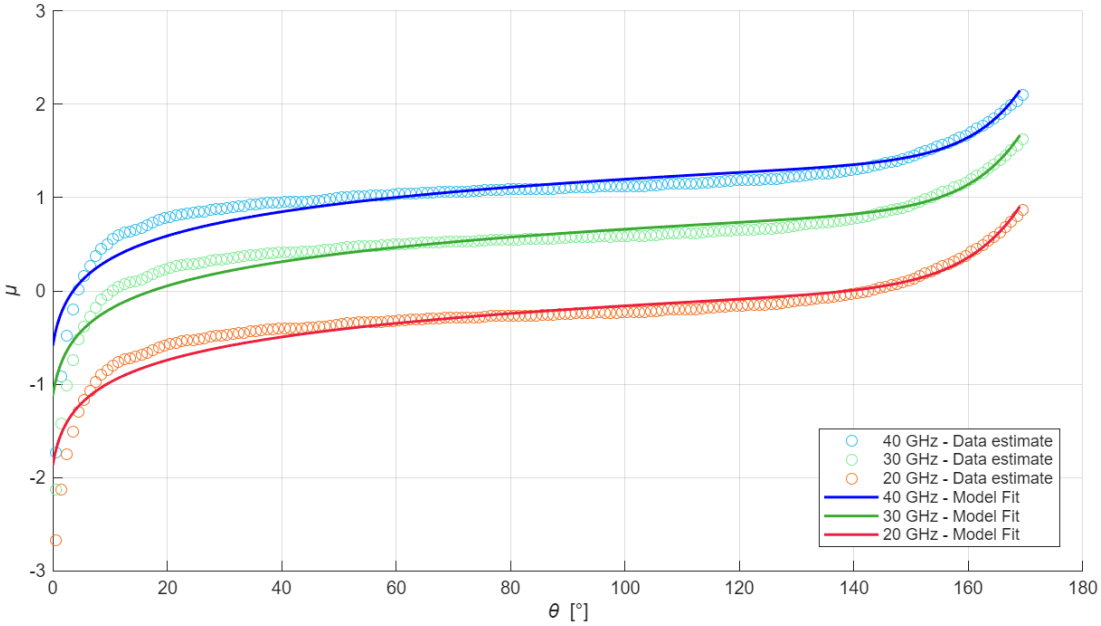

Figure 3.13: Fitted $\mu(\theta)$ model versus per class estimates from simulated data.

3.5.2. Model for $\sigma(\theta)$: two exponential end-corrections + low-angle bump

The modelling of $\sigma(\theta)$ is more complex. The behaviour from data estimate shows a sharp low-angle feature (rise and relaxation), a smoother mid-angle trend and a tail toward large separations. For counting all these contributions, a two-component model is used:

- A smooth baseline (two exponential end-corrections):

$$\sigma_{base}(\theta) = \sigma_0 + c_1 \exp\left(-\frac{\theta}{\tau_1}\right) + c_2 \exp\left(-\frac{(180-\theta)}{\tau_2}\right) \tag{3.18}$$

where σ_0 represents the average/background level, the term $c_1 e^{-\theta/\tau_1}$ mainly affects small angles and captures the initial relaxation/decay, while the term $c_2 e^{-(180-\theta)/\tau_2}$ becomes relevant at large separations and allows the final tail to be controlled.

- A low-angle bump modelled as a lognormal-shaped term in θ:

$$\sigma_{bump}(\theta) = A \exp\left(-\frac{(\ln(\theta+\varepsilon)-\mu_B)^2}{2s_B^2}\right) \tag{3.19}$$

where $\varepsilon = 1°$; the position of the maximum will be $\theta_{peak} \approx e^{\mu_B} - \varepsilon$.

In this way, the complete model results as the sum of the two components. The fitted coefficients are reported in *Table 3.4* for $\sigma(\theta)$ at the three considered frequencies.

Table 3.4: Coefficient values for $\sigma(\theta)$ model.

Frequency	$\boldsymbol{\sigma_0}$	$\boldsymbol{c_1}$	$\boldsymbol{\tau_1}$	$\boldsymbol{c_2}$	$\boldsymbol{\tau_2}$	$\boldsymbol{A}$	$\boldsymbol{\mu_B}$	$\boldsymbol{s_B}$
20 GHz	1.6685	-0.7107	7.98209	-0.23585	30.0623	0.4631	1.3065	0.9976
30 GHz	1.5805	-0.3195	25.9746	-0.27965	24.8418	0.4818	1.6145	1.3994
40 GHz	1.5653	0.2096	32.7017	-0.30595	29.8321	0.0805	1.7612	0.6282

These values yield $\theta_{peak} \approx 2.69°$ at $f = 20\,GHz$, $\theta_{peak} \approx 4.03°$ at $f = 30\,GHz$ and $\theta_{peak} \approx 4.89°$ at $f = 40\,GHz$. In *Figure 3.14* are illustrated the obtained modelled curves and *Figure 3.15* reports the application of the two-component model for $\sigma(\theta)$ at $f = 30\,GHz$.

At this step of study is not possible to find a relationship between those parameters and the working frequency, as the trend observing for $\sigma(\theta)$ does not show an approximately invariant shape across frequency over the whole angular range. This is most evident at low angular separations, where the relative ordering and curvature of the 20/30/40 GHz traces differ. This lack of shape invariance implies that a global frequency scaling based on a constant shift and/or scale factor cannot simultaneously fit the full θ-range.

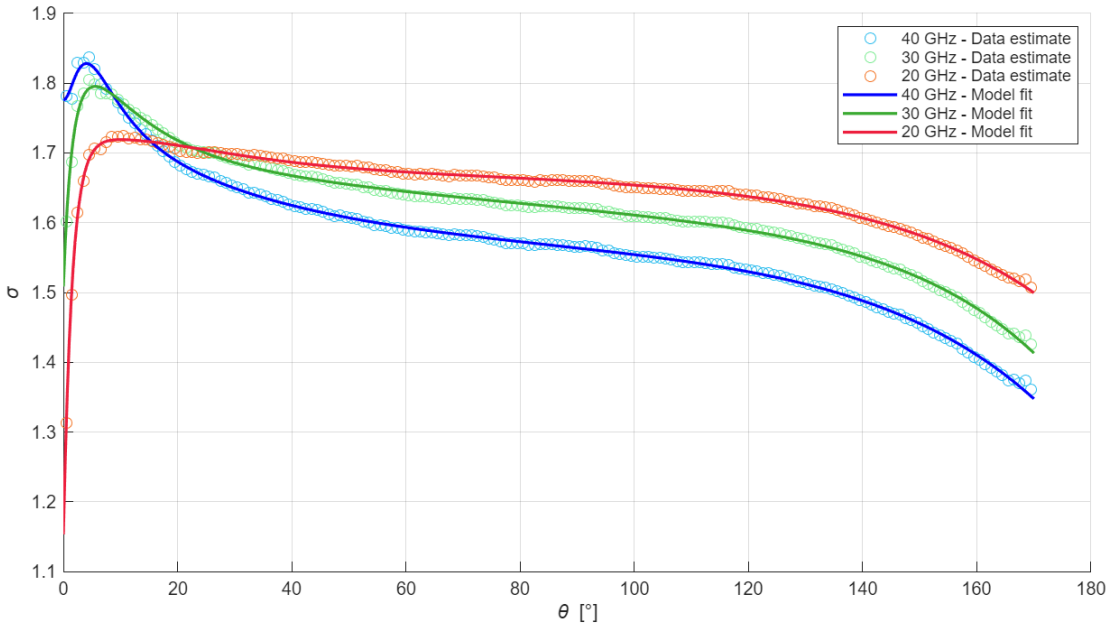

Figure 3.14: Fitted $\sigma(\theta)$ model versus per class estimates from simulated data.

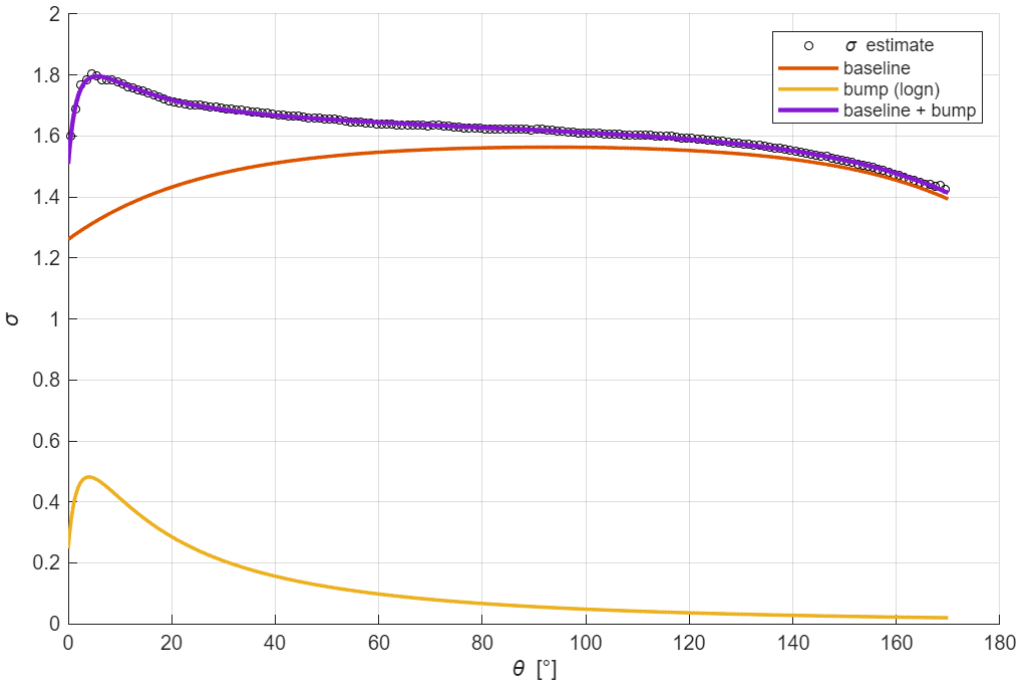

Figure 3.15: Application of the two-component model for $\sigma(\theta)$ at $f = 30\ GHz$.

3.5.3. Model-Based Reconstruction of $|\Delta A|$ Statistics

To validate the statistical model locally, representative angular classes are selected. For each class: the empirical PDF of $|\Delta A|$ is extracted from simulation samples and the model PDF is computed as:

$$f_{|\Delta A|}(x \mid \theta) = \text{LognormalPDF}(x; \mu(\theta), \sigma(\theta)), \tag{3.20}$$

with $\mu(\theta)$ and $\sigma(\theta)$ given by the fitted continuous models.
This check verifies that the model reproduces not only the mean behaviour, but also the shape of the distribution within each angular bin. For small and moderate angular separations, the model-based Lognormal PDFs closely match the empirical ones across the full range of $|\Delta A|$. For large separations, especially beyond $\theta \approx 140°$ a slight mismatch becomes visible, mainly in the very first attenuation bins, although the model still reproduces the overall decay and the tail behaviour. At high θ the number of available link pairs is typically smaller, making the empirical histogram noisier and the fit more sensitive. Some examples are shown in *Figure 3.16*.

A global validation is finally carried out by regenerating the density map $H_{norm}(\theta, |\Delta A|)$, through an analytic Monte Carlo procedure driven by the proposed parametric models. For each angular class c (centred at θ_c), the lognormal parameters are obtained directly from the fitted angle-dependent functions, i.e., $\mu_c = \mu(\theta_c),\ \ \sigma_c = \sigma(\theta_c)$.

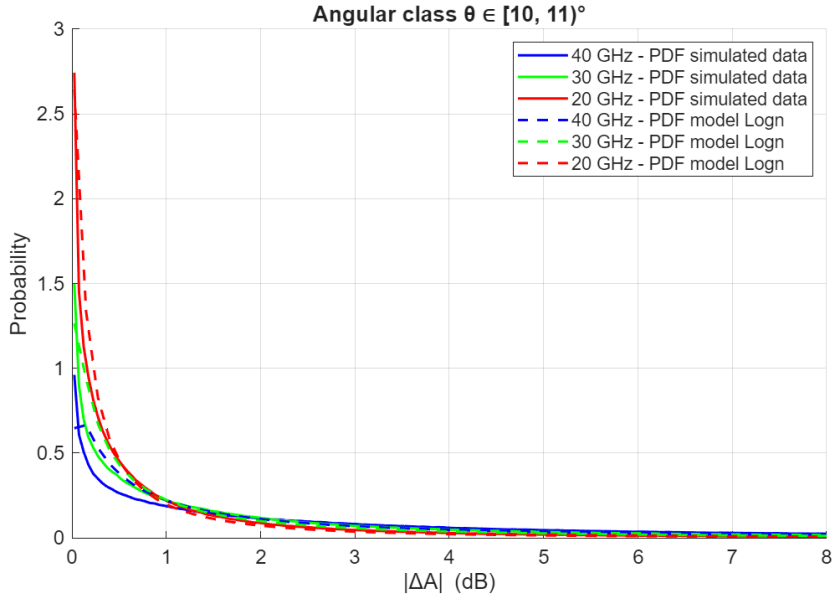
Angular class θ ∈ [10, 11)°
40 GHz - PDF simulated data
30 GHz - PDF simulated data
20 GHz - PDF simulated data
40 GHz - PDF model Logn
30 GHz - PDF model Logn
20 GHz - PDF model Logn
Probability
|ΔA| (dB)

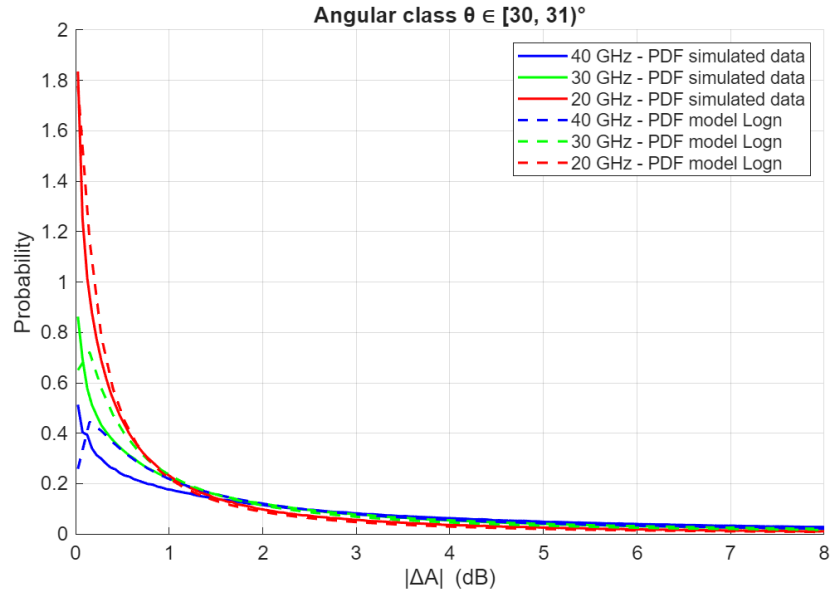
Angular class θ ∈ [30, 31)°
40 GHz - PDF simulated data
30 GHz - PDF simulated data
20 GHz - PDF simulated data
40 GHz - PDF model Logn
30 GHz - PDF model Logn
20 GHz - PDF model Logn
Probability
|ΔA| (dB)

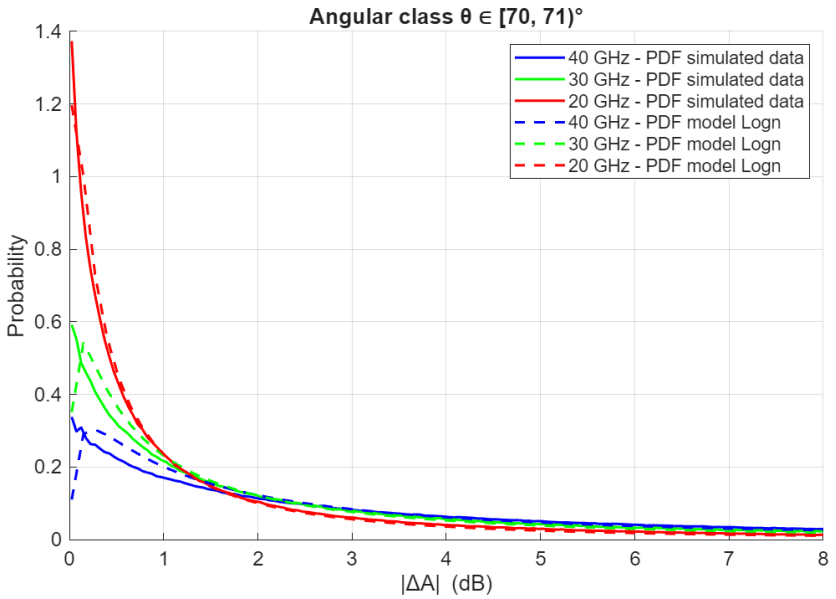
Angular class θ ∈ [70, 71)°
40 GHz - PDF simulated data
30 GHz - PDF simulated data
20 GHz - PDF simulated data
40 GHz - PDF model Logn
30 GHz - PDF model Logn
20 GHz - PDF model Logn
Probability
|ΔA| (dB)

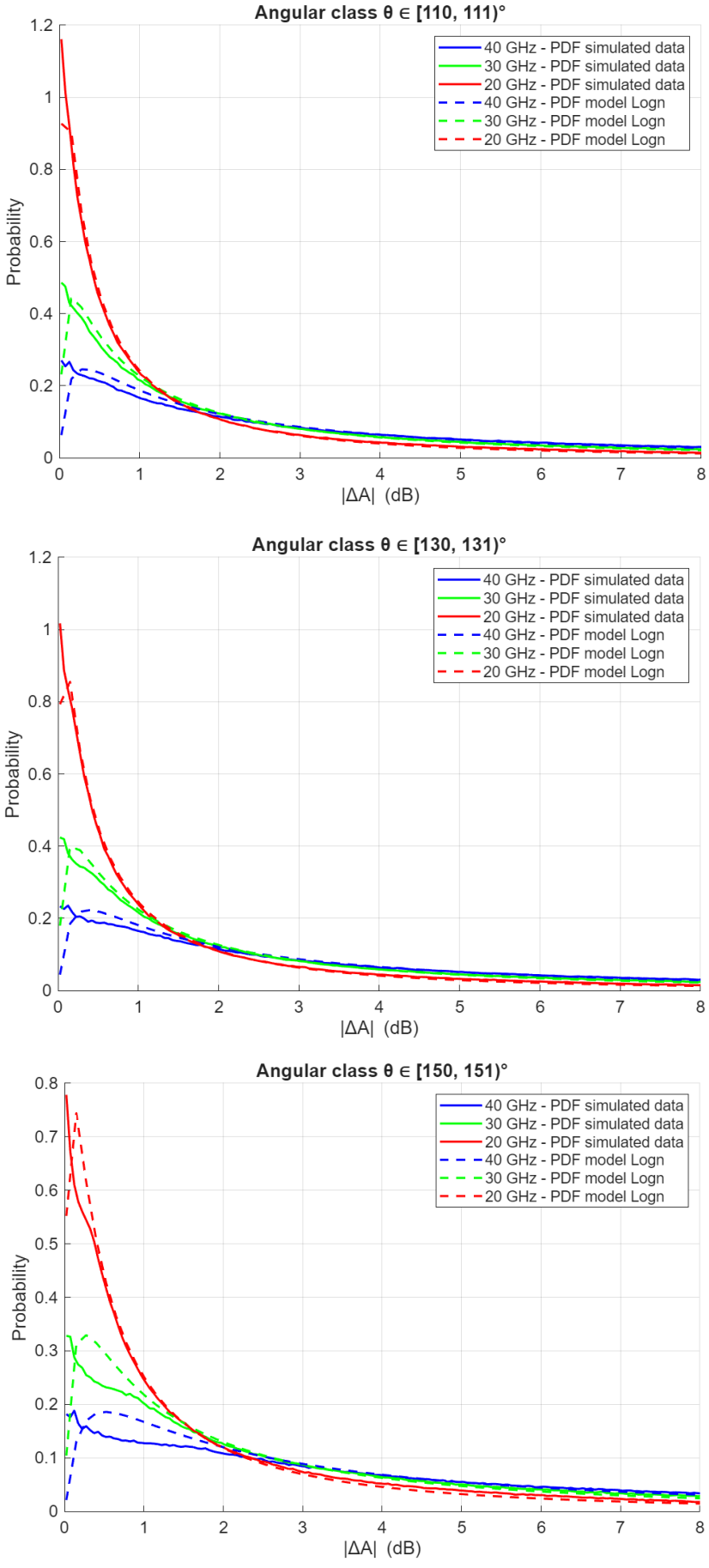

Figure 3.16: Empirical vs model-based PDFs for different angular classes.

Then, N independent samples are generated as

$$X_k(\theta_c) \sim \text{Lognormal}\big(\mu(\theta_c), \sigma(\theta_c)\big), \qquad k = 1, \dots, N. \tag{3.21}$$

The simulated samples are binned on the same $|\Delta A|$ grid used for the empirical density plots, producing a synthetic histogram for each angular class. Finally, the resulting 2D histogram is post-processed using the same column-wise normalization adopted for the simulator-based density maps, enabling a direct visual and quantitative comparison. The results are shown in *Figure 3.17*. A small margin of improvement can still be observed by visual inspection of the density maps. In particular, the region of highest concentration (darkest red) in the model-based maps appears slightly shifted towards $|\Delta A| \approx 0$ compared to the simulator-derived maps. This suggests that, while the lognormal assumption captures the overall skewness and tail behaviour well, it may not fully reproduce the fine structure of the empirical histograms around their mode. Capturing this subtle displacement would likely require exploring alternative distribution families or more flexible formulations (e.g., mixture models) capable of better matching the peak location across all angular classes. Nevertheless, among the candidate families investigated in this work, the lognormal distribution provides the closest overall agreement and the most consistent modelling framework across angles and frequencies.

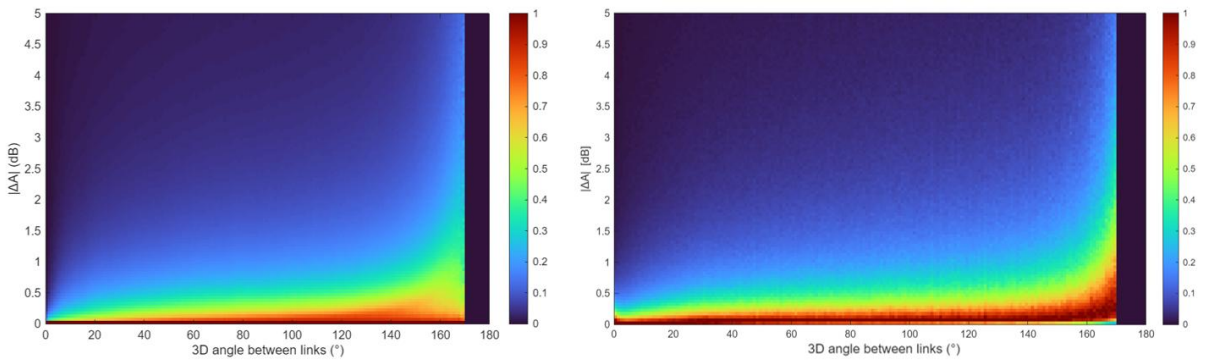

(a) $f = 20\ GHz$

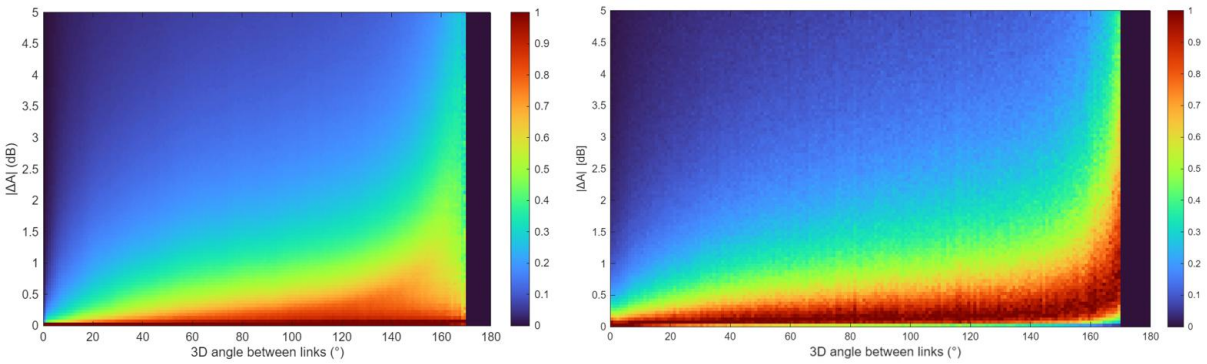

(b) $f = 30\ GHz$

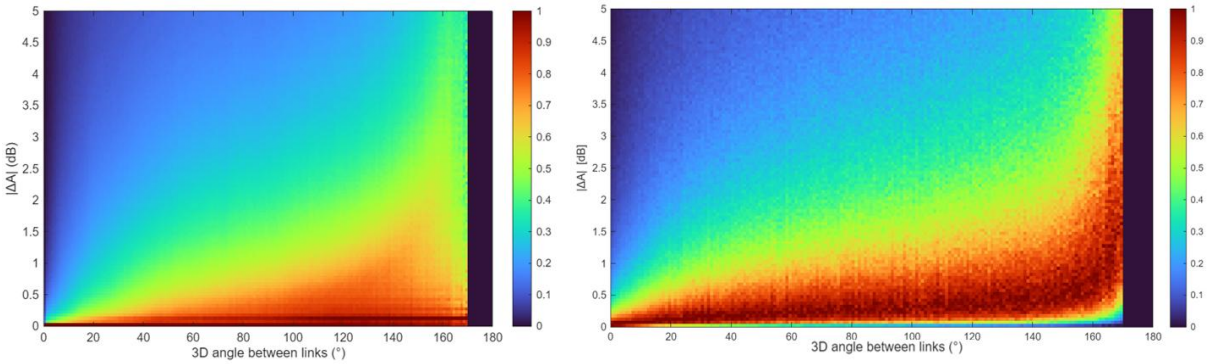

(c) $f = 40\ GHz$

Figure 3.17: Empirical vs model-based density plots: (left) simulation results, (right) analytic Monte Carlo reconstruction using $\mu(\theta)$ and $\sigma(\theta)$ models.

4 Conclusions and Future Works

The progressive migration of satellite systems toward Ka, Q and V bands, together with the rapid deployment of large NGSO constellations, makes rain attenuation the dominant propagation impairment for high-availability Earth–space links. In this context, conventional single-link design approaches are often insufficient to guarantee stringent availability targets. This thesis has therefore developed a simulation-based framework to quantify the performance improvements achievable through spatial diversity techniques in realistic NGSO scenarios. A key contribution is the extension of a rain-attenuation simulator to support multi-site and multi-satellite configurations. The simulator combines realistic space–time rain fields over a 200 km × 200 km domain, detailed NGSO orbital geometry, and pixel-level integration of specific attenuation along dynamically varying slant paths. The framework further supports configurable ground-station geometries, variable inter-site separations and a controllable number of simultaneously visible satellites. In addition, equal satellite visibility constraints are enforced across sites to ensure fair comparisons between SD, OD, and joint diversity schemes. Performance has been assessed through long-term attenuation time series and Complementary Cumulative Distribution Functions (CCDFs), and the obtained results confirm several key trends. Orbital Diversity provides monotonic improvement with increasing diversity order (i.e., number of simultaneously visible satellites); however, because all links originate from the same ground station, the achievable gain is limited by the angular correlation of the rain field. Site Diversity strongly depends on inter-site distance and on the number of deployed gateways: as the spatial correlation decreases with separation, significant diversity gains can be achieved, especially at low exceedance probabilities relevant to high-availability design. Finally, joint Site and Orbital Diversity (SD+OD) provides the largest mitigation benefit. By combining large-scale spatial decorrelation between sites with angular decorrelation between satellites, the joint scheme yields the greatest reduction of the CCDF tail, confirming the potential of coordinated multi-gateway/multi-satellite strategies for high-frequency NGSO feeder-link architectures. Beyond time-domain simulations, the thesis also introduces a statistical model for Orbital Diversity. The model relates the absolute attenuation difference between simultaneously visible links to their three-dimensional angular separation. Conditional attenuation-difference statistics are approximated via a lognormal

distribution, with parameters expressed as continuous functions of separation angle and characterized across multiple frequencies. This enables the generation of OD-related attenuation-difference statistics without full time-domain simulation, representing a first step toward a semi-analytical framework for NGSO diversity analysis.

The presented model considers rain as the only atmospheric impairment. Future developments could extend the simulator to include attenuation due to clouds, gaseous absorption (oxygen and water vapour) and depolarization effects caused by hydrometeors. This would allow the evaluation of total tropospheric attenuation rather than rain-only fading, enabling a more complete link-budget assessment. Moreover, modelling depolarization would enable the investigation of cross-polar discrimination degradation and its impact on dual-polarized high-throughput architectures. The developed simulator also enables additional analyses of FMTs performance in NGSO systems. Beyond selection combining, more advanced switching or weighted-combining strategies could be implemented (e.g., hysteresis-based policies). The framework could also be extended to jointly evaluate spatial diversity and adaptive techniques such as Adaptive Modulation and Coding (AMC) and dynamic bandwidth/resource allocation. Finally, the proposed OD statistical model constitutes a first approximation and deserves further refinement. In particular, a single lognormal distribution may not fully capture variability under mixed stratiform–convective regimes. Future work could investigate mixture-based approaches (e.g., mixtures of lognormal components), and generalize parameter dependencies with respect to frequency, elevation angle, and climate, leading to a more robust and portable modelling framework.

Bibliography

[1] Smirnov, A., Shprits, Y., Prol, F. et al. *A novel neural network model of Earth's topside ionosphere. Scientific Reports 13, 1303 (2023).*

[2] ITU-R. *Propagation data and prediction methods required for the design of Earthspace telecommunication systems.* Recommendation P.618-14, 2023.

[3] Lutgens, Frederick K., and Edward J. Tarbuck. *The Atmosphere*. 10th ed. Upper Saddle River, N.J.: *Pearson Prentice Hall,* 2007.

[4] R. Polonio and C. Riva, *"ITALSAT propagation experiment at 18.7, 39.6 and 49.5 GHz at Spino D'Adda: three years of CPA statistics," in IEEE Transactions on Antennas and Propagation*, vol. 46, no. 5, pp. 631-635, May 1998.

[5] L. Luini, C. Riva, F. Capelletti, A. Comisso, A. Rocha, S. Mota, M. Brás, M. Biscarini, S. Barbieri, F. Consalvi, A. Martellucci, "*Ka-Band Tropospheric Attenuation Derived from a MEO Satellite Constellation*", EuCAP 2024, pp. 1-5, 17-22 March 2024, Glasgow, Scotland.

[6] Lorenzo Luini. *Modeling the Space-Time Evolution of Rain Fields. IEEE Antennas Propagation Magazine*, August 2021.

[7] Crane, R.K. (1996) *Electromagnetic Wave Propagation through Rain. Wiley Interscience, New York.*

[8] Marshall, J. S. and Palmer, W. M., *"The Distribution of Raindrops with Size."*, Journal of the Atmospheric Sciences, vol. 5, no. 4, AMS, pp. 165–166, 1948. doi:10.1175/1520-0469(1948)005<0165:TDORWS>2.0.CO;2.

[9] ITU-R. *Rain attenuation model for rain for use in prediction methods.* Recommendation P.838-3, 2005.

[10] ITU-R. *Rain height model for prediction methods*. Recommendation P.839-4, 2013.

[11] H. Al-Hraishawi, H. Chougrani, S. Kisseleff, E. Lagunas, and S. Chatzinotas, *"A survey on non-geostationary satellite systems: The communication perspective," IEEE Communications Surveys & Tutorials*, vol. 25, no. 1, pp. 101–132, 2022, doi: 10.1109/COMST.2022.3197695.

[12] I. del Portillo, B. G. Cameron, and E. F. Crawley, "A technical comparison of three low earth orbit satellite constellation systems to provide global broadband," *Acta Astronautica*, vol. 159, pp. 123–135, Jun. 2019, doi: 10.1016/j.actaastro.2019.03.040.

[13] T. Pratt and J. E. Allnutt, *Satellite Communications*, 3rd ed. Hoboken, NJ, USA: Wiley, 2020.

[14] E. Lagunas, S. Chatzinotas, B. Ottersten, "Low-Earth orbit satellite constellations for global communication network connectivity," *Nature Reviews Electrical Engineering*, vol. 1, pp. 656–665, Sep. 2024, doi: 10.1038/s44287-024-00088-9

[15] ITU-R, Recommendation ITU-R S.1503-4, *"Functional description to be used in developing software tools for determining conformity of non-geostationary-satellite orbit fixed-satellite service systems or networks with limits contained in Article 22 of the Radio Regulations,"* Sept. 2023.

[16] T. Butash, P. Garland, and B. G. Evans, "Non-geostationary satellite orbit communications satellite constellations history," *International Journal of Satellite Communications and Networking*, vol. 39, no. 1, pp. 1–5, 2021, doi: 10.1002/sat.1375.

[17] D. A. Vallado, *Fundamentals of Astrodynamics and Applications*, 4th ed. Hawthorne, CA, USA: Microcosm Press, 2013

[18] ETSI, 2024. *Digital Video Broadcasting (DVB); Second generation framing structure, channel coding and modulation systems for Broadcasting, Interactive Services, News Gathering and other broadband satellite applications; Part 2: DVB-S2 Extensions (DVB-S2X).* European Standard (EN) 302 307-2 V1.4.1.

[19] L.Luini, C. Capsoni, "*A Rain Cell Model for the Simulation and Performance Evaluation of Site Diversity Schemes", IEEE Antennas and Wireless Propagation Letters*, vol. 12, No. 1, Page(s): 1327-1330, doi: 10.1109/LAWP.2013.2285400,2013.

[20] E. Matricciani, *"Orbital diversity in resource-shared satellite communication systems above 10 GHz,"* IEEE J. Select. Areas Commun., vol. 5, pp. 714–723, May 1987.

[21] Panagopoulos, Arapoglou and Cottis, "*Site versus orbital diversity: performance comparison based on propagation characteristics at the Ku band and above,"* in *IEEE Antennas and Wireless Propagation Letters*, vol. 3, pp. 26-29, 2004, doi: 10.1109/LAWP.2004.827898.

[22] https://hdl.handle.net/10589/190608

[23] Razavian, Mojtaba & Oestges, Claude & Vanhoenacker-Janvier, Danielle. (2022). *Synthetic Rain Models and Optical Flow Algorithms for Improving the Resolution of Rain Attenuation Time Series Simulated From Numerical Weather Prediction.* Radio Science. 58. 10.1029/2022RS007553.

[24] Capsoni, F. Fedi, C. Magistroni, A. Paraboni, A. Pawlina, "*Data and theory for a new model of the horizontal structure of rain cells for propagation applications," Radio Science*, Volume 22, Number 3, Pages: 395-404, May-June, 1987.

[25] L. Luini, C. Capsoni, "*MultiEXCELL: a new rain field model for propagation applications," IEEE Transactions on Antennas and Propagation*, vol. 59, no. 11, Page(s): 4286 – 4300, November, 2011.

[26] Tomaz, Luciano & Capsoni, C. & Luini, L.. (2023). *Model to Scale Rain Attenuation Time Series With Link Elevation Angle for LEO Satellite Based Systems*. Radio Science. 58. 10.1029/2022RS007551.

[27] L. Luini, C. Capsoni, "*MultiEXCELL: A new rain field model for propagation applications*", IEEE Transactions on Antennas and Propagation, vol. 59, no. 11, Page(s): 4286 – 4300, November 2011

[28] Louis J. Ippolito Jr. Satellite Communications Systems Engineering: *Atmospheric Effects, Satellite Link Design and System Performance.* Wiley, 2008.

[29] FCC. SpaceX V-Band Non-Geostationary Satellite System: Attachment A, Technical Information to Supplement Schedule S. Report SAT-LOA-20170301-00027, 2016.

[30] Luini, L. & Wioland, Bastien & Riva, Carlo Giuseppe. (2022). *Orbital and Spatial Diversity for Next Generation Large NGSO Satellite Constellations.* 1-6. 10.1109/MMS55062.2022.9825604.

[31] CelesTrak. Two-Line Element Set Format. https://celestrak.org/columns/v04n03/. [Online, accessed 01-Genuary-2026].

[32] ITU-R. Application of Article 22 of the Radio Regulations to the protection of geostationary fixed-satellite service and broadcasting-satellite service networks from nongeostationary fixed-satellite service systems in the frequency bands 37.5-39.5 GHz, 39.5-42.5 GHz, 47.2-50.2 GHz and 50.4-51.4 GHz. Resolution 770, 2019.

[33] Luini, L. & Jeannin, Nicolas. (2008). *Use of Weather Radar Data for Site Diversity Predictions and Impact of Rain Field Advection.* 122 - 127. 10.1109/ASMS.2008.29.

List of Figures

List of Tables

List of symbols

Variable	Description	SI unit
$\boldsymbol{\theta}$	elevation angle	degree
$\boldsymbol{\psi}$	azimuth	degree
$\boldsymbol{A_{NGSO}}$	rain attenuation on NGSO path	dB
$\boldsymbol{R}$	Rain rate	mm/h